

MAGNETICALLY ACTUATED MICROFLUIDIC MIXING AND PARTICLE CAPTURE

A Dissertation
Presented to
The Academic Faculty

by

Matthew Scott Ballard

In Partial Fulfillment
of the Requirements for the Degree
Doctor of Philosophy in the
George W. Woodruff School of Mechanical Engineering

Georgia Institute of Technology
August 2017

COPYRIGHT © 2017 BY MATTHEW SCOTT BALLARD

MAGNETICALLY ACTUATED MICROFLUIDIC MIXING AND PARTICLE CAPTURE

Approved by:

Dr. Alexander Alexeev, Advisor
George W. Woodruff School of
Mechanical Engineering
Georgia Institute of Technology

Dr. Hang Lu
School of Chemical and
Biomolecular Engineering
Georgia Institute of Technology

Dr. Peter Hesketh
George W. Woodruff School of
Mechanical Engineering
Georgia Institute of Technology

Dr. Damir Khismatullin
Department of Biomedical Engineering
Tulane University

Dr. Todd Sulchek
George W. Woodruff School of
Mechanical Engineering
Georgia Institute of Technology

Date Approved: May 3, 2017

To my amazing wife, Katie. Without your loving patience, sacrifice and support, none of
this would be possible.

ACKNOWLEDGEMENTS

I would like to begin by thanking my thesis advisor, Dr. Alexander Alexeev, for his mentoring and guidance over the years. He has kept me funded throughout my studies, taught me how to be a successful researcher and mentor, and has given me valuable career guidance and support. He has shown me that he truly cares about my success.

I would like to thank my dissertation reading committee, Drs. Todd Sulchek, Hang Lu, Damir Khismatullin and especially Peter Hesketh for their time and stimulating conversations and input that have contributed to my work.

I thank Dr. Marc Smith for mentoring me as a teacher. I thank the community at Georgia Tech Lorraine for the great experience that I had teaching there, as well as Marco Arienti at Sandia National Laboratories for the opportunity to expand my horizons.

I thank Drew Owen and Srinivas Hanasoge, as well as my many additional collaborators. They have helped me immensely in my work. I am thankful for my lab mates, class mates, undergraduate research assistants and other friends for their help in more than just research.

I am especially grateful for my family. I thank my parents, who taught me through example the value of hard work and always encouraged me to pursue my ambitions. I thank my children for keeping life fun and reminding me that there are more important things in life than work. Most importantly, I thank my sweet wife and best friend, Katie, for her love and support through the highs and lows, and for always being there for me. I would not be where I am today without her. Finally, I want to thank my Heavenly Father for blessing me with the confidence, clarity, strength and endurance needed to complete this work.

TABLE OF CONTENTS

ACKNOWLEDGEMENTS	iv
LIST OF FIGURES	vii
SUMMARY	xiii
CHAPTER 1. INTRODUCTION	1
1.1 Overview	1
1.2 Background and Literature Review	3
1.2.1 Microfluidic Mixing	3
1.2.2 Particle Capture	4
1.3 Research Objectives and Scope	6
CHAPTER 2. COMPUTATIONAL METHODOLOGY	8
2.1 Lattice Boltzmann Method (LBM)	8
2.2 Scalar Transport LBM	13
2.3 Lattice Spring Method (LSM)	14
2.4 Brownian Dynamics Model	18
2.5 Boundary Conditions and FSI Coupling	19
2.6 Summary	21
CHAPTER 3. MODELS OF MICROFLUIDIC SYSTEMS	22
3.1 Orbiting Magnetic Microbeads	22
3.1.1 Magnetic Bead Models	22
3.1.2 Mixing Model	26
3.1.3 Particle Capture Model	28
3.2 Synthetic Cilia Models	31
3.2.1 Filament Cilia	31
3.2.2 Ribbon Cilia	33
3.2.3 Mixing Model	36
3.2.4 Nano-Particle Deposition Model	37
3.3 Model Validation	38
3.3.1 Filament Cilia Deflection	38
3.3.2 Ribbon Cilia Deflection	40
3.3.3 Validation of Mass Transport Models	42
3.4 Summary	46
CHAPTER 4. MICROFLUIDIC MIXING AND PARTICLE CAPTURE USING ORBITING MAGNETIC MICROBEADS	47
4.1 Beads Dynamics and Resulting Flow	47
4.2 Microfluidic Mixing	51
4.2.1 Mixing by Orbiting Beads	51
4.2.2 Mixing Mechanisms	58
4.2.3 Mixing Distance	65

4.3	Micro-Particle Capture	69
4.3.1	Comparison to Experiments	69
4.3.2	Distance to Particle Contact	74
4.3.3	Capture of Non-Spherical Particles	77
4.4	Summary	79
 CHAPTER 5. MICROFLUIDIC MIXING AND PARTICLE CAPTURE USING MAGNETICALLY ACTUATED SYNTHETIC CILIA		81
5.1	Filament Cilia	82
5.1.1	Cilia Dynamics and Flow Generation	82
5.1.2	Asymmetric Cilia Actuation	86
5.1.3	Nano-Particle Capture	88
5.1.4	Microfluidic Mixing	94
5.2	Ribbon Cilia	96
5.2.1	Cilia Dynamics	96
5.2.2	Characterizing Cilia Stroke Patterns	101
5.2.3	Microfluidic Pumping	105
5.2.4	Generating Large-Scale Circulatory Flow	112
5.3	Summary	117
 CHAPTER 6. CONCLUDING REMARKS AND OUTLOOK		119
VITA	130	

LIST OF FIGURES

Figure 2.1 Schematic of the velocity distributions in a D3Q19 LBM model. The arrows represent the directions, c_i . Note that 0 represents the stationary distribution	9
Figure 2.2 a) 2-D triangular lattice with node i at the center, surrounded by six equally-spaced neighboring nodes. The solid lines represent springs connecting the nodes, and the dashed line is a unit cell associated with node i . b) 3-D cubic lattice with node i at the center, surrounded by 18 neighbors which are connected to it by springs	15
Figure 3.1 a) Experimental setup, with a permanent magnet rotating over the microfluidic chip, as designated by the red arrow. b) Diagram showing an instantaneous snapshot of magnetic microbeads (blue) located at the two magnetic poles generated on a NiFe disc (white) by a uniform horizontal external magnetic field, denoted by \mathbf{B} . Horizontal rotation of the uniform external magnetic field causes the magnetic poles to rotate about the NiFe disc so as to follow the external magnetic field, which results in the microbeads orbiting about the NiFe disc. c) Schematic of a periodic section of the microfluidic device, which consists of a microchannel with magnetic microbeads orbiting around NiFe discs patterned on the microchannel floor	23
Figure 3.2 Schematic of the device configured as a mixer. In the BD model, diffusive particles of two species are initially flowed in separate sides of the microfluidic channel, representing two fluid species	27
Figure 3.3 Schematic of the device configured for particle capture. In addition to orbiting magnetic beads, particles are suspended in the fluid and their dynamics calculated, so as to determine how far they move down the microfluidic channel before coming into contact with a microbead	29
Figure 3.4 Cumulative distribution function of the total number of captured particles plotted against the number of rows of beads that particles have travelled down the microfluidic channel	31
Figure 3.5 a) Periodic simulation domain, consisting of single elastic cilium actuated by a periodic force applied horizontally either distributed across its length or concentrated at its tip. b) Schematic of a fluid-filled microchannel with periodic arrays of cilia on the top and bottom walls. c) Schematic of a fluid-filled microchannel with a periodic array of cilia on only the bottom wall	32
Figure 3.6 a) Model of ribbon-shaped cilium. b) Periodic simulation domain for pumping and dynamics simulations. The top and bottom sides of the domain are solid walls, while the remaining sides are periodic, representing a large array of cilia pumping in the x -direction. c) Simulation domain for study of generation of circulatory flow in a channel of finite width. Here, the domain is periodic in the z - (axial-) direction, while there are solid walls on the edges in the x - (transverse) and y - (vertical) directions	34

Figure 3.7 Schematic of a microfluidic channel with a ciliated floor and bare ceiling filled with a viscous fluid. The fluid contains a solvent with initial concentrations of $C_i(0) = 0$ and $C_i(0) = 1$ at nodes on the bottom and top halves of the channel, respectively.....	37
Figure 3.8 Deflection (δ) of a beam cantilevered in the vertical- (y -) direction and subjected a force concentrated at the beam tip. This shows that LSM captures cilium deflections of over 50% with less than 5% relative error	40
Figure 3.9 Deflection (δ) of a beam cantilevered in the vertical- (y -) direction and subjected a force distributed evenly along its length. This shows that LSM captures cilium deflections of over 50% with less than 3% relative error in the ribbon cilium model.....	41
Figure 3.10 a) Schematic of the initial concentration profile used in the test case to validate the mass transport models used in this work. b) Concentration profiles showing the time-evolution of a solute in the microchannel, as calculated using the analytical solution, BD model and scalar transport LBM model. Each curve represents a separate point in time	43
Figure 3.11 Diffusive deposition of nano-particles in a microchannel without cilia. Here the analytical solution is compared to results obtained using the BD model at various values of Sc	44
Figure 3.12 Time evolution of the locations of mass-less non-diffusive tracer particles subjected to a magnetic microbead orbiting clock-wise through them in the channel, then exactly retracing its complete path. a) Initial distribution of particles. b) Distribution of particles after 14 clock-wise orbits. c) Distribution of particles after the entire process..	45
Figure 4.1 Instantaneous velocity fields generated by beads orbiting counter-clockwise in a microchannel with flow giving $U_x/V_b = 1$. a) Top view of the velocity field. Four pairs of beads are seen rotating counter-clockwise in a section of a microchannel, and velocity vectors at the half-height of the beads are given. b) Schematic showing the orientation of planes in which velocity fields are shown. c) Velocity field at a planar cross-section looking down the channel shows vertical flow due to magnetic microbeads	49
Figure 4.2 Streamlines of the period averaged fluid velocity at the plane located at the center height of the magnetic microbeads orbiting in a microchannel at the following velocity ratios: a) $U_x/V_b = 0$, b) $U_x/V_b = 0.3$, c) $U_x/V_b = 0.6$, and d) $U_x/V_b = 1.4$	50
Figure 4.3 a) Rapid mixing in an experimental micromixer. Streams of fluid with (white) and without (black) fluorescent nano-particles are mixed as they pass through a 300 μm mixing region. b) Simulation of mixing, made up of a series of images of the time evolution of the vertically averaged concentration field, each placed at the location corresponding to the distance fluid has moved downstream in the simulation. c) Profiles of concentration variation across the channel width at the inlet and outlet, shown for both	

experimental and simulation data. d) Summary of the calculated percentage of mixing, P , at the inlet and outlet of the mixing region for experiments, simulations, and a simulated channel with no microbeads, such that mixing occurs purely due to molecular diffusion over the length of the mixing region 52

Figure 4.4 Plot of the degree of mixing over dimensionless time for the case of no microbeads (pure diffusion) and of mixing enhanced by orbiting magnetic microbeads. 70% mixing occurs at times t_D and t_E for the pure diffusion and enhanced cases, respectively 54

Figure 4.5 Plots of mixing enhancement over a range of velocity ratios for different configurations. a) Arrays with channel height $H_c = 2a$ and two alternating offset rows of discs ($\theta = 26.6^\circ$) with the following values of disc spacing: ■ $S = 2a$, ● $S = 2.5a$, ▲ $S = 3a$, and ◆ $S = 1.5a$ (one bead per disc). b) Arrays with channel height $H_c = 2a$, disc spacing $S = 2a$ and discs offset at the following angles: ■ $\theta = 26.6^\circ$ (two alternating offset rows of discs), ● $\theta = 18.4^\circ$ (three alternating offset rows of discs), ▲ $\theta = 14.0^\circ$ (four alternating offset rows of discs), and ◆ $\theta = 0^\circ$ (square array of discs). c) Plot of mixing enhancement over a range of channel heights using arrays with $S = 2a$ and $\theta = 26.6^\circ$ at the following velocity ratios: ■ $U_x/V_b = 0$, ● $U_x/V_b = 0.3$, ▲ $U_x/V_b = 1.4$ 56

Figure 4.6 Vertically averaged concentration fields in microchannels after mixing a set amount of time $t = 25T$, where T is a fixed bead orbit period. a) Mixing due purely to diffusion (no beads). b – e) Mixing aided by orbiting microbeads at various velocity ratios: b) $U_x/V_b = 0$, c) $U_x/V_b = 0.3$, d) $U_x/V_b = 0.6$, and e) $U_x/V_b = 1.4$ 60

Figure 4.7 Horizontal view of the distribution of non-diffusive tracer particles from the entire height of the microchannel. a) Initial locations of tracer particles. b – e) Locations of tracer particles after 75 orbits of the magnetic microbeads in the channel at the following velocity ratios: b) $U_x/V_b = 0$, c) $U_x/V_b = 0.3$, d) $U_x/V_b = 0.6$, and e) $U_x/V_b = 1.4$ 61

Figure 4.8 Schematic of the effect of geometry and velocities on mixing performance. a) Schematic of the geometry of two NiFe discs (grey circles) with $S = 2a$ and $\theta = 26.6^\circ$, with their associated beads (blue circles). Beads travel approximately a distance of $3a$ during a half orbit around a NiFe disc. Fluid travels a distance of $3a$ to get from one row of beads to the next. b) Schematic showing the critical distances for escape of fluid from a bead orbit (fluid must travel at least $1.5a$ during one half orbit to get past the center of the bead as it returns) and for optimal mixing (fluid travels $2a$ during one quarter orbit so as to be in front of bead on next row) 63

Figure 4.9 a) Effect of S on optimal velocity ratio for mixing enhancement. b) Effect of θ on optimal velocity ratio for mixing enhancement 65

Figure 4.10 a) Mixing degree versus distance downstream from the inlet to the mixing section for various velocity ratios for the case of simulation of 20 rows of discs in the device (markers) and of simulation of a periodic domain that is two disc rows long, using time to estimate distance downstream (lines). b) Normalized distance downstream until the fluid reaches a level of 70% mixing under various conditions plotted against the velocity ratio. Inset shows a power-law increase in mixing distance (trend line in black) for low velocity ratios 66

Figure 4.11 Simulation results for the fraction of micro-particles flowed over a range of velocity ratios through a capture section of microchannels of varied height which are captured by orbiting magnetic microbeads. Here, it is assumed that all particles that come into contact with beads are captured 70

Figure 4.12 Capture fraction of particles in channels of varying height subjected to flows at different velocity ratios. Here, particles are not assumed to be captured irreversibly on contact. Hollow markers denote capture fractions obtained in the experiments of Owen (69). Lines with solid markers represent predicted particle capture under the same conditions, assuming that particles have a 20% probability of irreversible capture on contact with beads 72

Figure 4.13 Distance required for capture of 95% of spherical particles in a microchannel of height $H_c = 2a$ with NiFe disc spacing $S = 14\mu m$, $10\mu m$, and $8\mu m$ over a range of velocity ratios 75

Figure 4.14 Distance to capture of 95%, 90%, 80% and 70% of spherical particles subjected to flow at $U_x/V_b = 0.5$ by beads in a capture region with $S = 10\mu m$. The channel height, H_c , is varied so as to determine the effect of channel height on capture distance 76

Figure 4.15 Distance required to capture 80% and 95% percent of spherical and rod-shaped particles in a microfluidic channel with $S = 10\mu m$ and $H_c = 2a$ over a range of velocity ratios 78

Figure 5.1 Period-averaged velocity in the $x - y$ (cilia motion) plane (see Figure 3.5a) with $A = 1$, $\delta x/L = 1$, and a) $Sp = 2$, b) $Sp = 3$, c) $Sp = 4$, d) $Sp = 5$. For clarity, velocity magnitudes for $Sp = 2$, 4, and 5 are scaled up by a factor of ten as compared to those for $Sp = 3$. $Sp = 3$ results in the most significant circulatory flow patterns 83

Figure 5.2 Cilium tip trajectory for $Sp = 3$ and $\delta x/L = 1$ a) in the $x - y$ plane, and b) in the $x - z$ plane. Cilia movement is two-dimensional when the driving force amplitude is $A = 6$, but becomes 3-D when the driving force amplitude is increased to $A = 8$. Panels c) and d) show centerlines of cilia with $A = 8$ at different instants of cilium beating in the $x - y$ and $x - z$ plane, respectively. e) 3-D motion is a result of cilia buckling, due to a compressive force applied to the cilium end when it is bent over horizontally 86

Figure 5.3 Trajectories of cilia modeled as flexible filaments driven by symmetric and asymmetric oscillatory distributed forces at $Sp = 3$ and $A = 45$. Red lines are the tip trajectories, black lines are snapshots of the cilium centerline during the effective stroke, and blue lines are snapshots of the cilium centerline during the recovery stroke. a) Trajectory of the cilium tip for the case of $R_F = 1$, b) Snapshots of the cilium for the case of $R_F = 1$, c) Trajectory of the cilium tip for the case of $R_F = 0.5$, d) Snapshots of the cilium for the case of $R_F = 0.5$	88
Figure 5.4 Deposition of nano-particles ($Sc = 4000$) on microchannel walls without cilia and with cilia beating at $Sp = 3$, $\delta x/L = 1$, and $A = 1$. The time required to achieve 90% deposition is shown for each case, and is denoted by t_D and t_C , respectively.....	89
Figure 5.5 Deposition enhancement E in ciliated microchannels with $\delta x/L = 1$ for nano-particles with $Sc = 4000$. a) Cilia beating with different Sp and $A = 1$. b) Cilia beating with different A and $Sp = 3$	91
Figure 5.6 Dependence of E at 90% deposition on cilia sperm number Sp . The force amplitude is $A = 1$ and cilia separation is $\delta x/L = 1$	92
Figure 5.7 Dependence of E at 50% deposition on cilia spacing $\delta x/L$. The simulation parameters are $Sp = 3$, $A = 1$, and $\delta x = \delta x/2$	93
Figure 5.8 Dependence of E at 90% deposition on oscillation amplitude E for various Sc , $Sp = 3$, and $\delta x/L$	94
Figure 5.9 a) Concentration field in a microfluidic channel containing an array of flexible filaments driven by an oscillating distributed force at $Sp = 3$, $A = 8$, and $Sc = 2000$. Before mixing, the microchannel contained a layer of fluid with $C = 0$ (blue) and an equally thick layer with $C = 1$ (red). b) Time evolution of the degree of mixing of fluid layers in the case of Figure 5.9a (with cilia) and in a microchannel without cilia	95
Figure 5.10 Mixing enhancement in a microfluidic channel containing an array of cilia driven by an oscillating distributed force at $Sp = 3$ and $Sc = 2000$ with varied A	96
Figure 5.11 a) Series of experimentally-captured images of cilia at various instances of time throughout an oscillation cycle driven by CCW rotation of a magnetic B-field. The trajectory of the tip is denoted by the black and white dashed lines, which indicate the forward and recovery portions of the stroke, respectively. b) Similar images of cilia positions obtained using our numerical model	98
Figure 5.12 Cilium positions a-h at select times throughout the oscillation cycle given by black lines. For each cilium position, the corresponding B-field direction is given by a red arrow. The cilium tip (blue dots) traces out the tip trajectory through the forward and recovery strokes, as given in the top plot by the blue solid and dashed lines, respectively. At bottom, the magnitude and direction of the applied magnetic moment along the cilium	

length is given in red as a distribution plotted normal to the local cilium axis for the corresponding cilium positions at the given times t/T . While plotting the distribution normal to a curved axis gives the illusion of a sharp changes in the distribution, the magnetic moment and its spatial derivative both vary continuously along the cilium length..... 100

Figure 5.13 Cilia tip trajectories for varied values of Mn obtained by varying the magnitude of \mathbf{B} in a) experiments, and b) numerical simulations. Each colored curve represents a tip trajectory for a given value of Mn 102

Figure 5.14 Characterization of the effect of Sp and Mn on cilia behavior. Blue and red curves represent characteristic non-dimensional values obtained from simulations with varied ω , EI and ν at two values of Mn over a wide range of Sp . a) Effect on the non-dimensional stroke irreversibility time, T_s . b) Effect on the normalized cilium displacement, δ_s 104

Figure 5.15 Measures of pumping per cycle by each cilium a periodic array of cilia oscillating at $Sp = 2$ for varied Mn in a channel with $H/L = 1.1$. The red and green curves give $A_{enclosed}$ and $A_{enclosed}/4$, respectively. The blue curve is the pumping effectiveness, ε 107

Figure 5.16 Approximation of pumping in a microchannel with cilia oscillating at varied Sp for two values of Mn . a) $A_{enclosed}$ as a function of Sp , giving an approximation of the amount of fluid pumped by each cilium oscillation. b) $Q_{approx.}$, which approximates the volumetric flow rate of fluid pumped by cilia 108

Figure 5.17 Calculated pumping effect of oscillating cilia. a) Effect of H/L on pumping effectiveness ε . b) Effect of H/L on channel-area normalized pumping effectiveness ε_{ch} 110

Figure 5.18 Profiles of the normalized velocity in the pumping (negative $x -$) direction for a) $H/L = 6$ and b) $H/L = 2$ 111

Figure 5.19 Normalized mean transverse velocity of flow generated by oscillating cilia oriented so as to push fluid across a microchannel. The four curves represent velocities for configurations using one, two, three or four cilia stretching across the channel with varied H/L 114

Figure 5.20 Plot of streamlines of a slice of the period-averaged velocity field at the centerline of cilia for the case of 4 cilia across a channel with a) $H/L = 1.1$, and b) $H/L = 1.5$. Cilia oscillate at the locations of the circulatory flow cells at the bottom of the channels, and arrows indicate the direction of flow..... 116

SUMMARY

In recent years, microfluidic technologies have provided for drastic improvements in cost, speed and capabilities in a variety of areas, including bio-technology. Lab-on-a-chip devices have allowed processes that once required expensive and bulky equipment and highly-trained personnel to now be done on miniaturized, inexpensive devices that can often be used with very little training. Microfluidic mixing of fluid samples is a vital component of many of these processes, and precisely-controllable microfluidic mixing of complex samples including components such as live cells would be of great benefit. Additionally, efficient specific capture and extraction of particles such as bacteria and rare cells from fluid samples would greatly enhance current bio-sensing capabilities, but has proved to be a difficult problem to solve.

The objective of this work is to model and investigate microfluidic mixing and particle capture using magnetically actuated structures. More specifically, this work is focused on the study of two different types of magnetically actuated structures with microfluidic applications. The first type utilizes magnetic microbeads which are magnetically driven in controlled orbits through a fluid in a microchannel, while the second type uses synthetic cilia actuated in simple patterns by an oscillating or rotating magnetic field.

We use a fully coupled lattice Boltzmann lattice spring model to perform three-dimensional computational simulations to model and understand the fluid and solid dynamics of these systems. We then investigate the use of these structures for microfluidic mixing and for capture of particles from a fluid sample. We investigate the physical mechanisms that lead to microfluidic mixing and particle capture in these model systems.

Further, we study the effect of geometrical configurations and system parameters on microfluidic mixing and particle capture, so as to provide insight into how to exploit these physical mechanisms for effective mixing and particle capture. The results of our research will provide understanding of physical mechanisms that can be harnessed for microfluidic mixing and particle capture in bio-sensing and other microfluidic applications.

CHAPTER 1. INTRODUCTION

1.1 Overview

Lab-on-a-chip devices that make use of microfluidic technologies to perform laboratory operations on a small scale have a variety of benefits, as these compact devices can allow many operations to be performed rapidly at field locations at low cost and using small fluid sample sizes (1, 2). However, microfluidic systems have their own challenges. Due to the small length scale of microfluidic systems, they operate at a low Reynolds number (Re), in which the fluid motion is dominated by fluid viscosity, whereas inertial effects can be safely neglected. In this situation, creative mechanisms must be used to generate microflows that promote important functions such as microfluidic mixing and particle capture. Time-irreversible active mechanical manipulation of the fluid (3) can be used to create such flow. In our proposed research, we study the fluid dynamics of two different devices that use simple magnetic field inputs to create time irreversible movement, and investigate their ability to perform microfluidic mixing and particle capture.

The first type of device that we study is a miniaturization of a common mixer with which we are all familiar – the blender. A blender uses rotation of its blades in a fluid reservoir to create a circulation pattern in the fluid, which quickly and effectively mixes the fluid. A simple and inexpensive method of creating a similar action on the microscale is through a system of orbiting magnetic microbeads (4). In such a system, readily available magnetic microbeads are driven in controlled orbits around soft magnetic discs which are patterned onto the floor of a microfluidic channel through simple rotation of an external magnetic field. While such bead manipulation has been experimentally and numerically

demonstrated (4), there is not currently an understanding of the generated flow field, or of its effectiveness in microfluidic mixing or particle capture.

The second type of device which we study is inspired by nature. A variety of biological organisms utilize beating cilia to create flows in the surrounding fluid which help them to transport, capture and absorb nutrients, as well as to expel foreign objects (5, 6). Biological cilia are tiny elastic filaments that are generally a few micrometers in length, such that they operate in a low Reynolds number environment. Their elasticity combined with an asymmetric stroke (7-9) play a critical role in generating the motion required for efficient mass transport in a highly viscous fluid environment. The ability of biological cilia to regulate microscale transport processes has motivated researchers to design different types of biomimetic synthetic cilia (10-15), which are typically driven in a complicated fashion. A simple method of actuating microscale synthetic cilia so as to take advantage of cilia elasticity and create a time-irreversible asymmetric stroke could prove beneficial in providing microscale transport that supports microfluidic mixing and particle capture. Additionally, understanding the dynamics and effects of cilia that beat in similar fashion to those occurring in nature can provide insights into the function of biological cilia.

In the research presented herein, we study the dynamics of both types of magnetically actuated microfluidic devices, namely orbiting magnetic microbeads and magnetically actuated synthetic cilia. We examine the fluid flow patterns created therein, and study the utility of each device for both the task of microfluidic mixing and of particle capture. We examine the physical principles leading to microfluidic mixing and particle capture in these devices, so as to provide an understanding of how these devices can be effectively utilized in lab-on-a-chip applications.

1.2 Background and Literature Review

1.2.1 *Microfluidic Mixing*

Lab-on-a-chip technologies often require rapid mixing to ensure reliable processing of fluid samples in microfluidic devices. At the microscale laminar flows characterized by a low Reynolds number, mixing can be difficult to achieve if it is left purely to molecular diffusion, which is rather slow for rapid processing of a fluid sample (16, 17). In order to overcome this problem, a variety of passive and active microfluidic mixers have been developed (18).

Passive mixers use geometric features to mix fluid streams as they flow through the device (19-21). Stroock et al (17) demonstrated a continuous-flow chaotic mixer in which fluid streams flowed through a microchannel patterned with staggered herringbone-shaped grooves were effectively mixed through folding of the fluids into thin laminae, reducing the distance required for molecules to diffuse for mixing to occur. However, this mixer mixes over a downstream distance on the order of a centimeter, does not allow for independent control of flow rate and mixing, and is limited to continuous-flow applications.

Active mixers use external acoustic, electrical, or magnetic inputs to induce mixing by actively agitating fluid (22-25). Among other approaches, the use of ferromagnetic and superparamagnetic micro-particles is attractive for microfluidic mixing due to the ability to precisely guide the motion of these solid particles by alternating magnetic fields. Rida and Gijs (26) used a tightly-packed porous moving structure of chains of ferromagnetic micro-particles formed in a microchannel by an oscillating magnetic field to induce rapid

fluid mixing. However, the tightly packed structures used in such a design can obstruct motion of micro-particles present in the fluid sample, such as cells or unfiltered particulates, and thus limit the types of fluid samples that can be used in such a device. Additionally, the ferromagnetic particles required by this technique continue to agglomerate even after removal of the magnetic field. The use of superparamagnetic microbeads that do not remain magnetized upon removal of a magnetic field would be preferable, to allow for removal of individual beads for further analysis after processing (27).

Mao et al (28) and Owen et al (4) proposed an active mixer composed of a microchannel containing an array of superparamagnetic beads driven in controlled orbits around soft magnetic discs by the magnetic poles induced on the discs by a rotating external magnetic field. They showed through computer simulations that these orbiting magnetic beads can be potentially used to induce efficient mixing of a fluid in a microchannel.

1.2.2 Particle Capture

Rapid and specific detection of a dilute concentration of biological particles from fluid samples has proven to be a difficult task. Specific detection of bacteria has traditionally required a culturing step, so as to raise the small population of bacteria in a fluid sample up to a detectable level (29). While this method is able to raise even very low concentration levels to a detectable level, it can also be extremely time consuming, requiring an incubation time of several hours or even days (30).

More recently, microfluidic devices that use functionalized magnetic beads, which have a large surface area to volume ratio and can be easily extracted from a fluid sample, have

become popular in efforts to increase the speed and sensitivity of detection of biological particles (27, 31). Oftentimes, functionalized microbeads are incubated in fluid samples containing suspended target particles, allowing particles to specifically bind to the magnetic beads, and are then magnetically separated from the fluid sample for further analysis (32-35). While these methods can be effective at detection without growing an entire colony, the required incubation step is time-prohibitive for use in point-of-care and field applications.

In order to avoid a lengthy incubation step, beads can be magnetically held on surfaces in a microfluidic channel and used to capture biological particles from a fluid sample which is flowed over the static beads (36-40). Here, a static bed of functionalized magnetic microbeads acts as a filter for target particles, capturing particles that come into contact with the beads as they flow through the capture bed. However, capture using stationary beads is relatively inefficient and requires a long capture distance and for magnetic beads to occlude the entire height of the microchannel to achieve even a moderate capture efficiency (36).

Alternatively, surfaces of the microfluidic channel or of structures within the channel can be directly functionalized and used for specific particle capture (41). Capture on such surfaces does not allow for extraction of magnetic beads with their attached captured particles for further analysis, although the presence of captured particles can be detected through methods such as impedance measurements (41). As with the use of static beads, this method suffers from inefficiency due to the fact that target particles must come into contact with static surfaces to become captured.

1.3 Research Objectives and Scope

The objective of this dissertation is to model and investigate the governing physics of two methods of providing microfluidic mixing and particle capture using magnetically actuated structures. The first method utilizes magnetic microbeads which are magnetically driven in controlled orbits through a fluid in a microchannel, while the second uses synthetic cilia actuated in a simple manner by an oscillating or rotating magnetic field. For each type of system, we desire to answer three basic questions: (1) What dynamic behaviors does the system exhibit which can be useful in microfluidic applications? (2) How can the system be utilized so as to provide for microfluidic pumping? (3) How can the system be used for capture of particles from a fluid sample?

In order to answer these questions, we use a fully coupled lattice Boltzmann lattice spring model to perform three-dimensional computational simulations. Using these simulations, we investigate the fluid and solid dynamics of the systems. We then investigate the use of these structures for microfluidic mixing and for capture of particles from a fluid sample. We investigate the physical mechanisms that lead to microfluidic mixing and particle capture in these model systems. Further, we study the effect of geometrical configurations and system parameters on microfluidic mixing and particle capture, so as to provide insight into how to exploit these physical mechanisms for effective mixing and particle capture. The results of our research will provide understanding of physical mechanisms that can be harnessed for microfluidic mixing and particle capture in bio-sensing and other microfluidic applications.

The remainder of the dissertation is organized as follows. In Chapter 2, we describe the FSI and mass transport models in detail. In Chapter 3, we give details on how we use these basic computational methods to model the specific systems that we study and show validation of the models used in this work. In Chapter 4, we discuss the fluid and solid dynamics of magnetic microbeads orbiting in a fluid-filled microfluidic channel, and explore the use of orbiting microbeads in microfluidic mixing and micro-particle capture applications. In Chapter 5, we discuss the dynamics of two different types of magnetically-actuated synthetic cilia: high-aspect-ratio flexible filaments, and ribbon-shaped cilia. We investigate how to control their dynamics and their effect on fluid transport for microfluidic mixing and nano-particle capture applications.

CHAPTER 2. COMPUTATIONAL METHODOLOGY

In order to simulate the fluid and solid mechanics of our microfluidic systems, we use a computational method for fluid-structure interactions (FSI) (42, 43) that makes use of the lattice Boltzmann method (LBM) fully coupled to a lattice spring method (LSM) through appropriate boundary conditions (42, 43). Velocities of lattice spring nodes at the solid-fluid interface are transmitted to the surrounding fluids through a modified bounce-back rule (44) that transfers momentum to the LBM distribution functions crossing the interface. LSM nodes on the boundary experience forces from the fluid pressure and viscous stresses calculated using the momentum exchange in the LBM fluid. A Brownian dynamics model is coupled to this model in order to model mass transport of nano-particles for microfluidic mixing and nano-particle deposition applications. In order to accelerate microfluidic mixing simulations, a lattice Boltzmann scalar transport model is used in place of the Brownian dynamics model.

2.1 Lattice Boltzmann Method (LBM)

We model fluid flow using LBM, an efficient solver of incompressible viscous flows (45, 46). LBM is particularly well suited for flows with complex moving geometries, making it a good candidate for our purposes. The algorithm for LBM follows two steps: a streaming step, in which fluid “particles” move along predefined directions to neighboring nodes on a space-fixed lattice, and a collision step, in which the fluid “particles” equilibrate through collisions at the nodes. These fluid “particles” represent mesoscopic amounts of fluid and are described by a set of velocity distribution functions $f_i(\mathbf{r}, t)$, which give the mass

density of fluid “particles” propagating in the direction i with velocity c_i at the lattice node \mathbf{r} and time t . The number of distribution functions corresponds to the number of fluid propagation directions in a given model. In our simulations, we use a three-dimensional model with 19 streaming directions (D3Q19) as illustrated in Figure 2.1, which uses 19 distribution functions at each node (46).

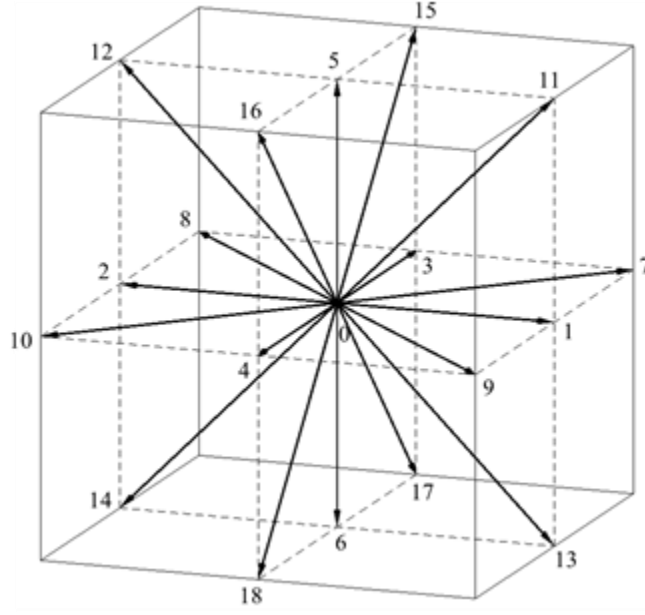


Figure 2.1 Schematic of the velocity distributions in a D3Q19 LBM model. The arrows represent the directions, c_i . Note that 0 represents the stationary distribution. The

discrete velocities of fluid in the streaming directions are as follows:

$$\mathbf{c}_i = \begin{cases} (0,0,0), & i = 0 \\ (\pm 1,0,0), (0,\pm 1,0), (0,0,\pm 1) & i = 1,2,\dots,6 \\ (\pm 1,\pm 1,0), (\pm 1,0,\pm 1), (0,\pm 1,\pm 1) & i = 7,8,\dots,18 \end{cases} \quad (2.1)$$

The hydrodynamic fields of the system are obtained by taking the moments of the distribution function, such that the mass density ρ , the momentum \mathbf{j} , and the momentum flux $\mathbf{\Pi}$ are given as the following, where \mathbf{u} is the local fluid velocity:

$$\rho = \sum_i f_i, \quad (2.2)$$

$$\mathbf{j} = \rho \mathbf{u} = \sum_i \mathbf{c}_i f_i, \quad (2.3)$$

$$\mathbf{\Pi} = \sum_i \mathbf{c}_i \mathbf{c}_i f_i. \quad (2.4)$$

The time evolution of the distribution function is governed by the discretized Boltzmann equation (45):

$$f_i(\mathbf{r} + \mathbf{c}_i \Delta t, t + \Delta t) = f_i(\mathbf{r}, t) + \Delta_i[f(\mathbf{r}, t)] \quad (2.5)$$

Here, the collision operator Δ_i acts on the distribution functions at every simulation time step Δt , and represents the effects of collisions of fluid “particles” at each node. We use Ladd’s double relaxation time collision operator (46), which is given by

$$f_i(\mathbf{r}, t) + \Delta_i[f(\mathbf{r}, t)] = a_i \left[\rho + \frac{\mathbf{j} \cdot \mathbf{c}_i}{c_s^2} + \frac{(\rho \mathbf{u} \mathbf{u} + \mathbf{\Pi}_{neq}^*) : (\mathbf{c}_i \mathbf{c}_i - c_s^2 \mathbf{I})}{2c_s^4} \right]. \quad (2.6)$$

Here, the weights a_i depend on the lattice speed in direction i , $|\mathbf{c}_i|$, and are given by

$$a_i = \begin{cases} 1/3, & |\mathbf{c}_i| = 0 \\ 1/18, & |\mathbf{c}_i| = 1 \\ 1/36, & |\mathbf{c}_i| = \sqrt{2} \end{cases} \quad (2.7)$$

The speed of sound is given by $c_s = \Delta x / \sqrt{3} \Delta t$, where Δx is the uniform spacing between lattice nodes. In our simulations, we set both Δx and Δt to always be equal to 1. Thus, the LBM length scale is defined by the lattice. Dimensional lengths for physical systems can be calculated using scaling arguments.

The non-equilibrium momentum flux $\mathbf{\Pi}_{neq}^*$ that appears in equation 2.6 is given as

$$\mathbf{\Pi}_{neq}^* = (1 + \lambda) \bar{\mathbf{\Pi}}_{neq} + \frac{1}{3} (1 + \lambda_v) (\mathbf{\Pi}_{neq} : \mathbf{I}) \mathbf{I}, \quad (2.8)$$

where $\mathbf{\Pi}_{neq} = \mathbf{\Pi} - \mathbf{\Pi}_{eq}$ and $\bar{\mathbf{\Pi}}_{neq}$ is the traceless part of $\mathbf{\Pi}_{neq}$. The equilibrium momentum flux is given by $\mathbf{\Pi}_{eq} = \rho c_s^2 \mathbf{I} + \rho \mathbf{u} \mathbf{u}$. The two relaxation parameters in this LBM model are λ and λ_v , which are related to the shear and bulk viscosities, respectively, through the following relationships:

$$\mu = -\rho c_s^2 \Delta t \left(\frac{1}{\lambda} + \frac{1}{2} \right), \quad (2.9)$$

$$\kappa = -\rho c_s^2 \Delta t \left(\frac{2}{3\lambda_v} + \frac{1}{3} \right). \quad (2.10)$$

In our simulations, we at times vary λ so as to control the system viscosity. We set $\lambda_v = -1$, giving a finite bulk viscosity, and thus a weakly compressible fluid. In order to model incompressible fluid flow and minimize potential compressibility effects, we keep the Mach number $Ma = u / c_s$ sufficiently small, typically below 0.15.

As mentioned previously, the LBM algorithm is made up of two main steps, namely collision and streaming, as described below:

1. Compute the post-collision distribution function at each lattice node:

$$f_i^* = f_i^*(\mathbf{r}, t) = f_i(\mathbf{r}, t) + \Delta_i[f(\mathbf{r}, t)]. \quad (2.11)$$

2. Propagate the distribution function to the neighboring lattice node in its velocity direction, \mathbf{c}_i :

$$f_i(\mathbf{r} + \mathbf{c}_i \Delta t, t + \Delta t) = f_i^*. \quad (2.12)$$

These two steps are repeated at each simulation time step. It is important to note that the collision portion of the algorithm requires most of the overall computation time, as the propagation step is very simple. However, since the collision step is performed locally at each node without requiring information from its neighbors, computations can be greatly accelerated by using parallel processing to simultaneously calculate the collision step at several nodes at once.

2.2 Scalar Transport LBM

In order to efficiently solve the convection-diffusion equation and thus enable simulation of microfluidic mixing in the large domain required for modeling oscillating cilia, we use a scalar transport LBM (47, 48). In this method, we model the concentration of a solute in the fluid using a second distribution function, $g_i(\mathbf{r}, t)$, which experiences one-way coupling to the velocity field. This allows for concentration calculations to be performed alongside fluid mechanics calculations, requiring minimal additional computational effort, as compared to a significant computational effort to calculate trajectories of thousands and even millions of diffusive particles using the BD model described in section 2.4. Analogous to calculating density in the LBM, the solute concentration can be obtained from the relation

$$C = \sum_i g_i. \quad (2.13)$$

The time evolution of this second distribution function is governed by the following equation:

$$g_i(\mathbf{r} + \mathbf{c}_i \Delta t, t + \Delta t) = (1 - \lambda_c) g_i(\mathbf{r}, t) + \lambda_c g_i^{eq}(\mathbf{r}, t). \quad (2.14)$$

Here, λ_c is the relaxation parameter governing the diffusion of the concentration of a solute, and is related to the diffusivity by

$$D_0 = \frac{\Delta x^2}{3\Delta t} \left(\frac{1}{\lambda_c} - \frac{1}{2} \right). \quad (2.15)$$

The equilibrium distribution function is given as

$$g_i^{eq} = Ca_i \left[1 + \frac{\mathbf{u} \cdot \mathbf{c}_i}{c_s^2} + \frac{(\mathbf{u} \cdot \mathbf{c}_i)^2}{2c_s^4} - \frac{\mathbf{u} \cdot \mathbf{u}}{2c_s^2} \right]. \quad (2.16)$$

2.3 Lattice Spring Method (LSM)

We simulate the dynamics of solids using the LSM (49, 50), which has advantages over the widely used finite element methods (FEM) in that it has a simpler implementation, is more robust at large deformations, and typically requires less computational power. LSM has been shown to be equivalent to a simple case of FEM in which the springs form element boundaries (49, 51). LSM models elastic solids as a system of distributed mass points (nodes) connected by harmonic springs (49) arranged on a regular lattice. The mapping of this model to macroscopic properties depends on the structure of the lattice network used. It has been proven that both square and triangular lattices behave like isotropic elastic solids (52). Depending on the system being modeled, we either use a two-dimensional (2-D) triangular lattice representation of a solid surface, or a three-dimensional (3-D) square lattice representation of the internal structure of the solid object. In all cases, we design our lattice such that we can form triangulated boundary surfaces, since this allows for simple coupling of LSM and LBM for FSI (42).

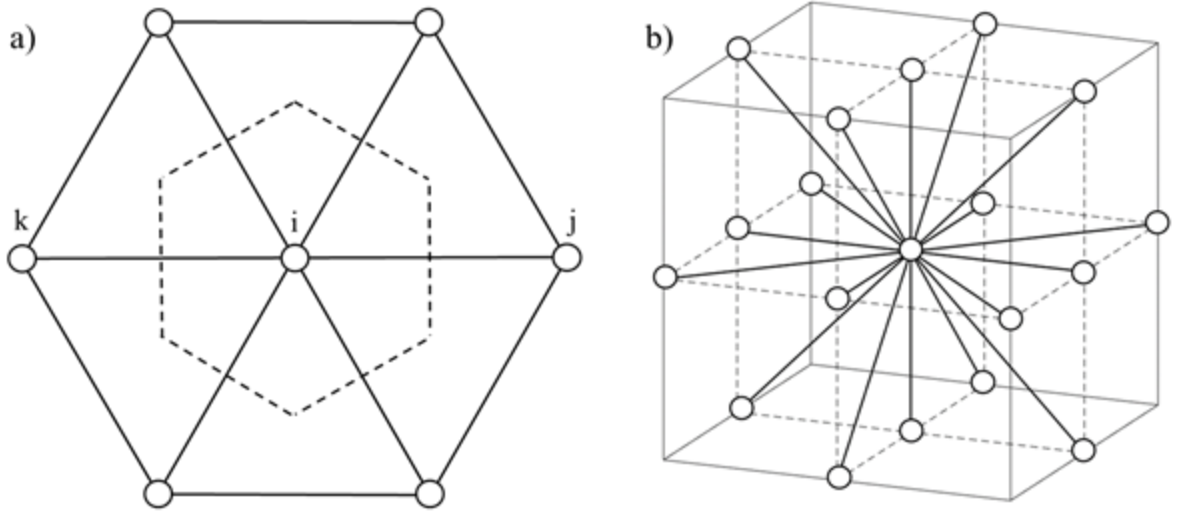


Figure 2.2 a) 2-D triangular lattice with node i at the center, surrounded by six equally-spaced neighboring nodes. The solid lines represent springs connecting the nodes, and the dashed line is a unit cell associated with node i . b) 3-D cubic lattice with node i at the center, surrounded by 18 neighbors which are connected to it by springs

For a 2-D triangular lattice, each node is connected to each of its six nearest neighbors by a harmonic spring with spring constant k_s , as shown in Figure 2.2a. Here, node i is located at the center, and is surrounded by six equally-spaced neighboring nodes. The stretching spring force between neighboring nodes i and j is given by

$$\mathbf{F}_{s,ij}^{str} = -k_s (r_{ij} - r_0) \hat{\mathbf{r}}_{ij}. \quad (2.17)$$

Here, r_{ij} is the distance between a pair of neighboring nodes, $\hat{\mathbf{r}}_{ij}$ is a unit vector from i to j , and r_0 is the equilibrium spacing between LSM nodes. For this model, the Young's modulus is given by $E_s = \frac{2}{\sqrt{3}} k$. For a simple isotropic 2-D triangular lattice, the Poisson ratio is $\nu = 1/3$.

In order to model resistance of 2-D lattice structures to out of plane bending, we add bending springs at node i . We define a bending unit as a collinear triplet jik , where nodes j and k are located opposite each other on either side of node i , as shown in Figure 2.2a. For each bending unit, a bending spring with stiffness k_b is placed at node i so as to resist out of plane bending. The forces supplied by the bending spring on each of the nodes of the bending unit are given by

$$\mathbf{F}_{s,j}^{bend} = -\frac{k_b}{r_{ij}r_{ik}} \left(\mathbf{r}_{ik} - \frac{\cos \theta_{jik}}{r_{ij}^2} \mathbf{r}_{ij} \right), \quad (2.18)$$

$$\mathbf{F}_{s,k}^{bend} = -\frac{k_b}{r_{ij}r_{ik}} \left(\mathbf{r}_{ij} - \frac{\cos \theta_{jik}}{r_{ik}^2} \mathbf{r}_{ik} \right), \quad (2.19)$$

$$\mathbf{F}_{s,i}^{bend} = -(\mathbf{F}_{s,j}^{bend} + \mathbf{F}_{s,k}^{bend}), \quad (2.20)$$

where \mathbf{r}_{ij} is a vector from node i to node j . Note that since each LSM node can be both a center point and an end point of a bending unit, it can feel multiple forces overall from all bending units with which it is associated. It has been proven that for a triangular lattice, this bending model yields a plate bending rigidity of $EI = 3\sqrt{3}k_b/4$ (53).

We also use a simple isotropic 3-D cubic lattice to model elastic solids as a network of springs connecting 18 nearest and next-nearest neighbors (Figure 2.2b). In this model, stretching spring forces are calculated as in the 2-D model, giving a Young's modulus of

$E_s = \frac{5k}{2l_0}$, where l_0 is the equilibrium lattice spacing. This 3-D lattice model handles

bending of static structures naturally without the addition of bending springs, and the resulting EI can be calculated from the Young's modulus and geometric dimensions.

The spring forces, along with forces arising from momentum exchange with the fluid and additional externally applied forces (such as magnetic forces, which will be discussed in greater detail in chapter 3) combine to give the total force at each node, \mathbf{F}_i . Motion of the solid nodes is determined through numerical integration of Newton's second law,

$$\mathbf{F}_i = m_i \frac{d^2 \mathbf{r}_i}{dt^2}. \quad (2.21)$$

We perform the numerical integration using the velocity Verlet algorithm (54, 55). This method is second order accurate in time, and has been used widely in molecular dynamics codes. The basic algorithm for calculation of the position, velocity and acceleration at the following time step $t + \Delta t$ is as follows:

1. Calculate the velocity at time $t + \Delta t/2$ using the known acceleration at time t :

$$\mathbf{a}_i(t) = \mathbf{F}_i(\mathbf{r}_i(t), t) / m_i, \quad (2.22)$$

$$\mathbf{v}_i(t + \Delta t/2) = \mathbf{v}_i(t) + \mathbf{a}_i(t) \Delta t/2. \quad (2.23)$$

2. Calculate the new position at time $t + \Delta t$ based on the velocity at time $t + \Delta t/2$:

$$\mathbf{r}_i(t + \Delta t) = \mathbf{r}_i(t) + \mathbf{v}_i(t + \Delta t/2) \Delta t. \quad (2.24)$$

3. Calculate the new acceleration and velocity at the new position and time:

$$\mathbf{a}_i(t + \Delta t) = \mathbf{F}_i(\mathbf{r}_i(t + \Delta t), t + \Delta t) / m_i, \quad (2.25)$$

$$\mathbf{v}_i(t + \Delta t) = \mathbf{v}_i(t + \Delta t/2) + \mathbf{a}_i(t + \Delta t) \Delta t/2. \quad (2.26)$$

2.4 Brownian Dynamics Model

We use a BD method (56, 57) to calculate mass transport of nano-particles for nano-particle deposition and microfluidic mixing. This method models diffusive mass-less particles whose trajectories are governed by the stochastic-differential equation:

$$d\mathbf{r}(t) = \mathbf{u}(\mathbf{r}, t)dt + \sqrt{2D_0}d\mathbf{W}(t), \quad (2.27)$$

where $\mathbf{r}(t)$ is the particle location. The first term on the right describes the advection of particles by the local fluid velocity $\mathbf{u}(\mathbf{r}, t)$, while the second term on the right represents the contribution of Brownian diffusion, where $D_0 = k_B T / 6\pi\mu r$ is the diffusion coefficient of the particle in the fluid and $d\mathbf{W}(t)$ is the differential of a Wiener process with unit variance. Here, k_B is Boltzmann's constant, T is the absolute temperature, μ is the dynamic viscosity of the fluid, and r is the diffusive particle radius. Equation 2.27 can be discretized as

$$\mathbf{r}(t + \Delta t) = \mathbf{r}(t) + \mathbf{u}[\mathbf{r}(t)]\Delta t + \sqrt{2D_0}\Delta\mathbf{W}(t), \quad (2.28)$$

where $\Delta\mathbf{W}$ is a random number sampled from a truncated Gaussian distribution with unit variance and is obtained using the Ziggurat method (58). We obtain the local fluid velocity

at the location of individual particles through linear interpolation of the fluid velocity at neighboring LBM nodes.

For microfluidic mixing simulations, we use two sets, or “species,” of diffusive particles to represent two initially separated miscible fluids. Once the locations of the diffusive particles are determined, we calculate the particle concentration at each fluid node by comparing the number of particles of species A in the $1 \times 1 \times 1$ bin surrounding the node to the total number of particles in that same bin,

$$C = \frac{N_A}{N_A + N_B}, \quad (2.29)$$

where N_A and N_B are the number of particles of species A and B, respectively, in each bin.

2.5 Boundary Conditions and FSI Coupling

FSI coupling is performed through a procedure in which momentum is transferred between fluid and solid nodes through appropriate boundary conditions (42, 43). In this method, the LSM mass nodes are used to define surfaces of the solid structures, which define the boundary between the fluid and solid. In the LBM model, we apply no-slip and no penetration boundary conditions using a linear interpolated boundary rule (44). In this boundary condition implementation, the velocity distribution functions that propagate from the fluid across boundary surfaces are reflected back in the opposite direction and modified with an exchange of momentum based on the position and velocity at the interpolated location of the intersection of the distribution function with the solid surface.

The momentum that is transferred to the fluid in this LBM bounce-back is then subtracted from the LSM nodes in the form of a hydrodynamic force applied in the integration of the LSM node position. This hydrodynamic force is distributed among the three LSM nodes that make up the boundary surface, while conserving forces on the interface. Details on this coupling procedure are found elsewhere (42).

In the scalar transport LBM, the solute concentration is coupled to the velocity field so as to model convection of a scalar quantity of solute. Note that no quantities related to the solute concentration appear in the equations governing the fluid flow, and thus it does not affect the flow. This is a valid approximation so long as the presence of the solute does not appreciably change the properties of the fluid.

A boundary condition of zero mass flux of solute is imposed at solid surfaces using an interpolated bounce-back rule (44, 59), analogous to the method used for boundary conditions on the fluid mechanics but with C and $g_i(\mathbf{r}, t)$ replacing ρ and $f_i(\mathbf{r}, t)$, respectively.

In order to couple the BD model to LBM, we use an interpolated fluid velocity in calculations of particle trajectories, as mentioned previously. We neglect the influence of diffusive particles on the fluid flow and any interactions between diffusive particles, including their agglomeration in the flow. We also neglect momentum exchange between the diffusive particles and the solid surfaces. These assumptions are valid for relatively dilute suspensions with particles much smaller than the solid structures.

As our boundary conditions for the BD model, we take all solid surfaces except those at which particles are deposited to be perfectly reflective of the particles, such that the

particles do not deposit on them. This condition is imposed by reflecting particles off of the solid surfaces by reversing the component of particle velocity that is normal to the surface. We also apply this reflective boundary treatment at the faces of the domain that represent non-adsorptive microchannel walls, and apply periodic boundary conditions for particles crossing the ends of the channel that are subject to periodic flow conditions. Particles that contact adsorptive surfaces are counted and removed from the simulation. This method and treatment of boundary conditions ensures conservation of the total number of diffusive particles suspended in the fluid or deposited on adsorptive surfaces.

2.6 Summary

Herein we have described the computational methodology which we use to simulate the solid and fluid mechanics of various microfluidic systems, as well as relevant mass transport phenomena. We use the LBM and LSM to model fluid and solid dynamics, respectively. In order to model mass transport, we use either a scalar transport LBM or a BD model. We use appropriate boundary conditions to couple the models. System-specific models which integrate these basic methodologies can be developed to capture the relevant physics of various microfluidic systems.

CHAPTER 3. MODELS OF MICROFLUIDIC SYSTEMS

We use the methodology described in chapter 2 to create computational models that approximate two specific types of magnetically actuated microfluidic systems. Our computational simulations enable a detailed study of the physical mechanisms involved in the function of these systems and provides an efficient means of their optimization for application in microfluidic mixing and particle capture. Specifically, we modelled a system that uses superparamagnetic microbeads moved in controlled orbits around soft magnetic features patterned on the floor of a microchannel in order to provide for microfluidic mixing and particle capture. We also modelled bio-mimetic cilia that are utilized to enhance transport processes in microfluidic devices, providing microfluidic mixing, pumping and nano-particle capture.

3.1 Orbiting Magnetic Microbeads

3.1.1 *Magnetic Bead Models*

Our first microfluidic device utilizes simple rotation of an externally applied magnetic field to drive superparamagnetic microbeads in controlled orbits around nickel-iron (NiFe) discs patterned on the bottom surface of a microfluidic channel (60, 61). A uniform horizontal external magnetic field, applied by a permanent magnet (Figure 3.1a), induces two magnetic poles located on opposite ends of the NiFe discs in alignment with the external magnetic field, as shown in Figure 3.1b. Superparamagnetic microbeads are drawn toward the poles, such that a magnetic microbead is located at each pole on the NiFe disc. Rotation of the permanent magnet results in rotation of the poles about the NiFe discs, and thus in

the movement of microbeads in controlled orbits on the patterned surface. Although multiple magnetic beads can follow each NiFe disc pole, at high rotation rates the fluid drag experienced by orbiting beads removes all beads but one, leaving a single bead to orbit at each pole. Since this configuration is stable and predictable and allows for flexibility of the rotation rate, we focus our investigation on the case where no more than one bead is located at each of the two NiFe poles.

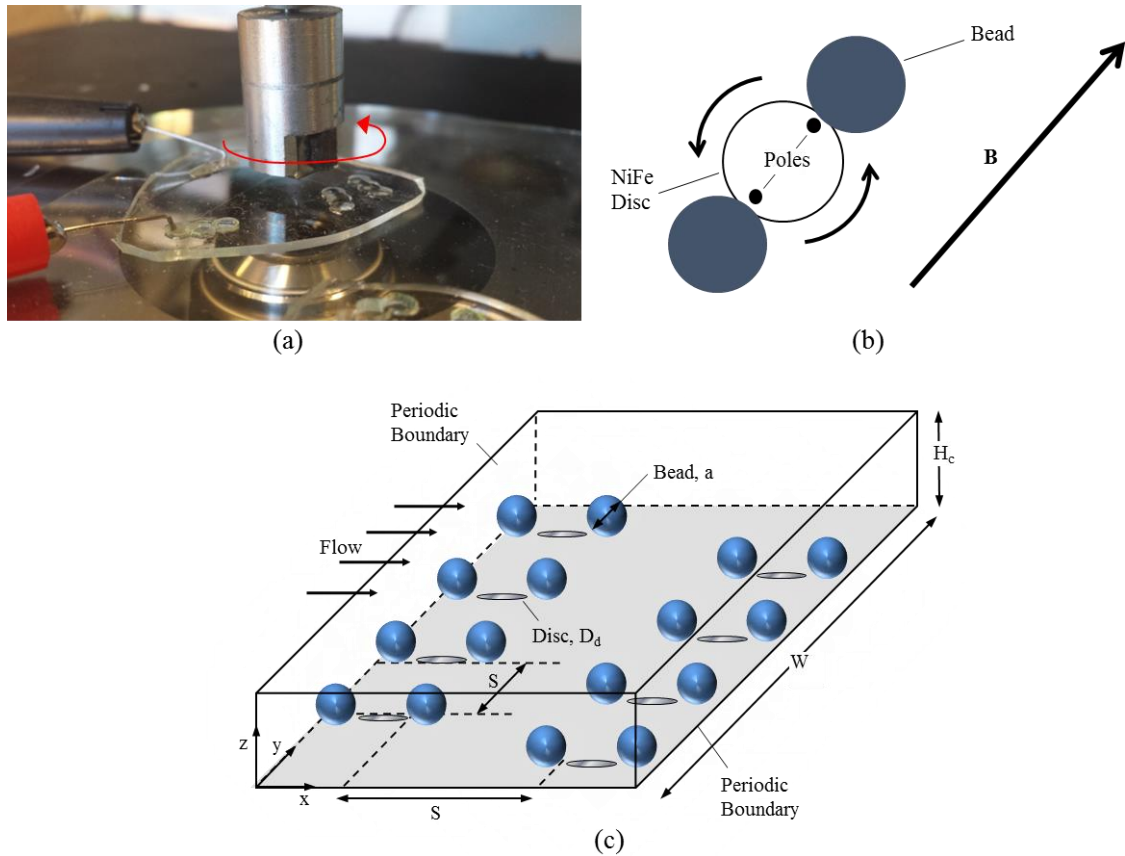


Figure 3.1 a) Experimental setup, with a permanent magnet rotating over the microfluidic chip, as designated by the red arrow. b) Diagram showing an instantaneous snapshot of magnetic microbeads (blue) located at the two magnetic poles generated on a NiFe disc (white) by a uniform horizontal external magnetic field, denoted by \mathbf{B} . Horizontal rotation of the uniform external magnetic field causes the magnetic poles to rotate about the NiFe disc so as to follow the external magnetic field, which results in the microbeads orbiting about the NiFe disc. c) Schematic of a periodic section of the microfluidic device, which

consists of a microchannel with magnetic microbeads orbiting around NiFe discs patterned on the microchannel floor

As shown in Figure 3.1c, we model the microfluidic device as a rectangular channel of width W and height H_c with solid walls in the y – (transverse) and z – (vertical) directions, and periodic boundaries in the x – (flow) direction, allowing for representation of a long channel. We model superparamagnetic microbeads of diameter a in orbit around NiFe discs of diameter D_d and height h , separated by spacing S .

We model two types of flow in a microchannel: EOF and pressure-driven flow. Owen et al. (61) and Ballard et al. (60) used EOF in experiments, since it allows for simple and precise control of flow through the channel even at low flow rates without the drawbacks of flow pulsations or bubbles introduced into the fluid via syringe pumps (62, 63) or the narrow range of flow rates available when using gravity driven flow. We perform simulations using EOF, so as to directly compare to experimental results. However, since EOF does not provide substantial pumping under certain ion concentrations likely to be seen in biological samples and is not a viable option with live cells (63-65), pressure driven flow is expected to be of most use in biological applications involving live cells and is thus used for the majority of simulations in this work. The plug-like EOF is simulated by assigning flow velocity through constant velocity boundary conditions at the channel walls (46). To simulate pressure-driven Poiseuille flow, we use a body force uniformly applied to the fluid in the microchannel (46).

We calculate magnetic forces on the superparamagnetic beads using the method employed by Owen et al. (4). In this model, the magnetic field of the NiFe discs is taken to be in alignment with the external magnetic field due to the high permeability and low

coercivity of NiFe, which allow it to be readily magnetized and demagnetized. The superparamagnetic beads, which tend to align along the applied field, saturate at a much lower value, and thus their effects on the magnetic field are negligible. The magnetic field of a single cylindrical soft magnet in a uniform external magnetic field can be theoretically evaluated (4, 66). Due to the linearity of the magnetic field, we use superposition of the contribution from each individual disc in the array to calculate the total magnetic field in the microchannel (67). The magnetic force acting on the magnetic beads is

$$\mathbf{F}_m = \mu_0^{-1} \Delta(\mathbf{M} \cdot \mathbf{B}), \quad (3.1)$$

where $\mu_0 = 4\pi \times 10^{-7}$ H/m is the permeability of free space, \mathbf{B} is the magnetic field vector, and

$$\mathbf{M} = V_p \chi \mathbf{B} \quad (3.2)$$

is the magnetic moment of a bead with volume V_p with the difference in magnetic susceptibility between the beads and the medium being χ . In the case of saturation of bead magnetization, the magnetic force simplifies to (68)

$$\mathbf{F}_m = V_p \chi \mu_0^{-1} (\mathbf{B} \cdot \Delta) \mathbf{B}. \quad (3.3)$$

We used the aforementioned method to calculate \mathbf{F}_m and applied it to solid surface nodes as a component of $\mathbf{F}(\mathbf{r}_i)$ in Newton's equation of motion (equation 2.21), so as to calculate bead trajectories, thereby enabling two-way coupling between the magnetic and

hydrodynamic forces. We found that for the range of velocities considered in our study, hydrodynamic forces are relatively small compared to magnetic forces and therefore do not affect magnetic control of microbeads. In this situation, the bead trajectories do not change appreciably with varied flow rates or bead velocities. Thus, we simplify simulations by first calculating trajectories of microbeads induced by a rotating magnetic field, and then removing the calculation of the magnetic forces and imposing the bead trajectories directly through prescribing their velocity. This allows simulations of mixing and particle capture to be significantly accelerated.

Since this microfluidic device operates at a low Reynolds number ($Re \ll 1$), the velocity of the net flow of the fluid down the channel and the linear velocity of the orbiting microbeads, V_b , can be varied without affecting system behavior so long as pertinent dimensionless parameters are maintained constant. Thus, the ratio of these velocities, U_x/V_b , rather than their absolute values, is important in the behavior of the system. Additionally, the bead Peclet number $Pe_b = V_b a / D_0$, which gives the relative importance of advective transport due to the orbiting beads to transport due to molecular diffusion, defines the system behavior for mixing applications.

3.1.2 *Mixing Model*

We model microfluidic mixing using a BD model, as described in Section 2.4. Here, we model two discrete sets of diffusive point particles, with each set tracked as a separate fluid ‘species.’ Two initially separated fluid streams of particles, as portrayed in Figure 3.2 as the different colored sections of the channel, were flowed in the x - direction down the microchannel.

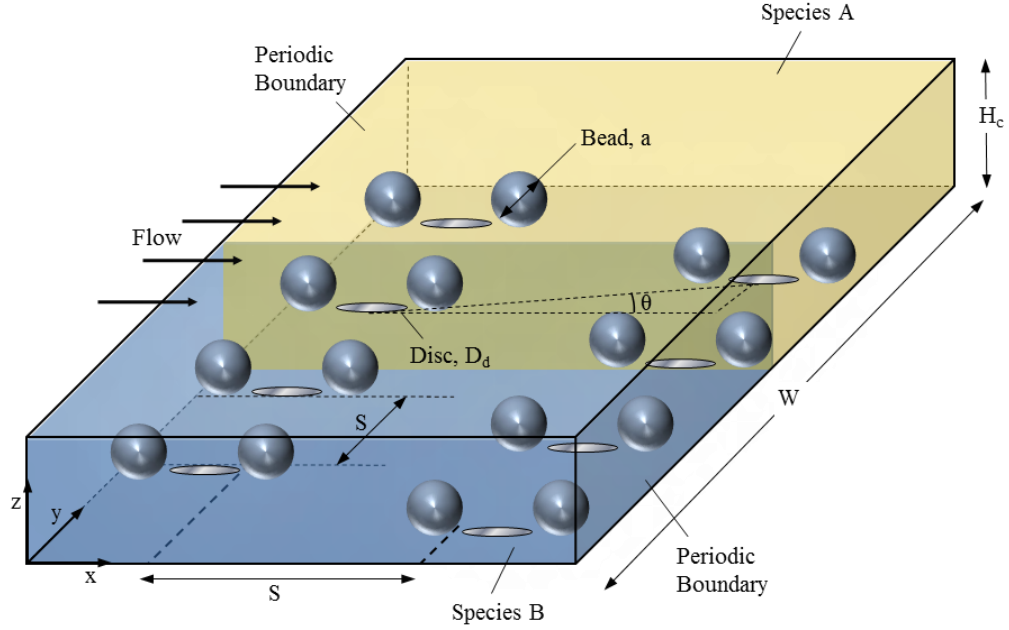


Figure 3.2 Schematic of the device configured as a mixer. In the BD model, diffusive particles of two species are initially flowed in separate sides of the microfluidic channel, representing two fluid species

In this study, we use $35N$ particles, where N is the number of fluid nodes in the simulation domain. This amounts to 1-20 million particles in each simulation, depending on the domain size. Once the locations of the diffusive particles are determined, we calculate the particle concentration at each fluid node by comparing the number of particles of species A in the $1 \times 1 \times 1$ bin surrounding the node to the total number of particles in that same bin,

$$C_i = \frac{N_{A,i}}{N_{A,i} + N_{B,i}}, \quad (3.4)$$

where $N_{A,i}$ and $N_{B,i}$ are the number of particles of species A and B, respectively, in bin i .

To quantify the level of mixing in a given region of the microfluidic channel, we use a dimensionless degree of mixing

$$\sigma = 2 \sqrt{\frac{1}{N} \sum_{i=1}^N (C_i - \bar{C})^2} \quad (3.5)$$

where \bar{C} is the average particle concentration (manifest in experiments as fluorescence intensity) in the channel and N is the number of pixels (from two-dimensional experimental images) or fluid nodes (from three-dimensional simulation data) in the region where mixing is measured. For the case of equal amounts of species A and B in the channel, $\sigma = 1$ indicates that the fluid species are fully separated, and when $\sigma = 0$ they are uniformly mixed. Alternatively, the mixing parameter can be expressed as a percentage of mixing

$$P = (1 - \sigma) \times 100. \quad (3.6)$$

3.1.3 Particle Capture Model

We model the dynamics of microscopic particles of similar size to that of the magnetic beads, which are suspended in the fluid, as shown in Figure 3.3. These particles are modelled using the LSM in identical fashion to the magnetic beads, except that they do not experience magnetic forces, allowing them to move freely with the fluid. As with other LSM structures, we use two-way coupling between the particles and the neighboring fluid. In order to reduce the effect of beads on each other and thus to model capture of a low

concentration of particles, we reduce the amount of particles per volume in the channel until further reduction does not appreciably affect simulation results.

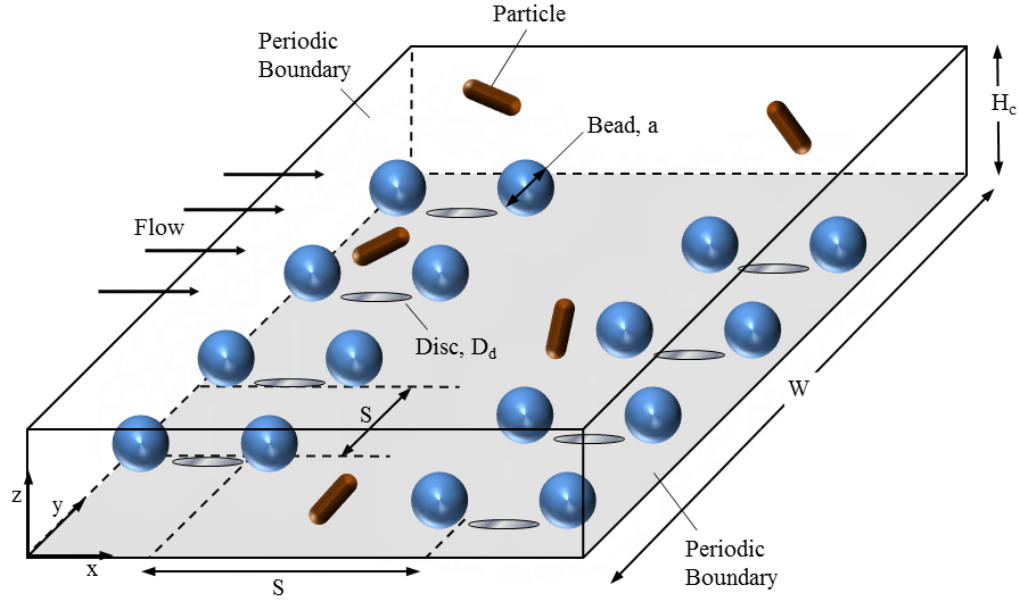


Figure 3.3 Schematic of the device configured for particle capture. In addition to orbiting magnetic beads, particles are suspended in the fluid and their dynamics calculated, so as to determine how far they move down the microfluidic channel before coming into contact with a microbead

Two types of micro-particles are used in the simulations. Rod-shaped particles with a length to diameter ratio of $L_r/D_r = 4$ were used to model salmonella bacteria. Spherical particles were also modeled, so as to compare to experiments and to assess the effect of particle shape on capture. These particles were scaled such that for magnetic microbeads of diameter $a = 2.8\mu m$, the rod-shaped particles have diameter $D_r = 0.5\mu m$ and the spherical particles have diameter $D_s = 1\mu m$, corresponding to the actual size of salmonella and of particles used by Owen (69) in experiments, respectively.

In order to model particle capture in an efficient manner, we make the following assumptions. We assume that the particles and beads must come into direct contact with each other for capture to occur, since their ligands and receptors are much smaller than the particles (tens of nanometers compared to a few microns). We assume that binding occurs more quickly than the bead orbit time scale, and that the binding force between particles and beads is much greater than the hydrodynamic forces pulling them apart. This leads us to assume that salmonella that come into contact with beads are irreversibly captured. While this assumption may not be completely valid for all potential experimental conditions, it allows us to determine the effectiveness of beads at coming into contact with particles, which is a necessary step in capture. This yields an upper limit on capture efficiency, so as to guide experiments and to assist in determining cases in which it would be beneficial to explore conditions leading to improved binding kinetics.

A Monte Carlo simulation is carried out to obtain statistical capture data on a large particle population. Particles are placed randomly in the simulation domain, and released into the system. When a particle is captured, the capture location is compared to its initial location to obtain a downstream distance to capture (Δx). The values of Δx for the particles in the population studied under specified conditions are used to estimate a cumulative distribution function as shown in Figure 3.4, which is used to determine the percentage of particles captured at various distances downstream.

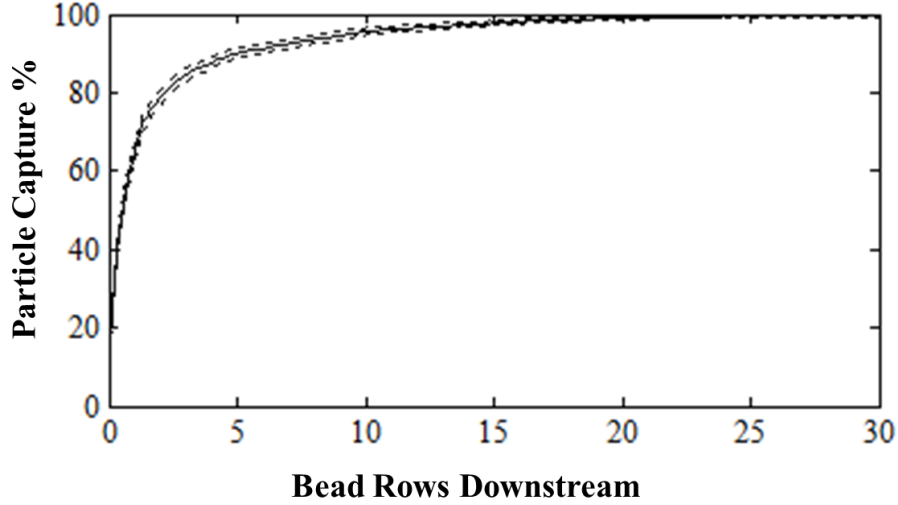


Figure 3.4 Cumulative distribution function of the total number of captured particles plotted against the number of rows of beads that particles have travelled down the microfluidic channel

3.2 Synthetic Cilia Models

We model two different types of magnetically actuated synthetic cilia. The first type is a high aspect ratio flexible filament as can be fabricated from polydimethylsiloxane (PDMS) impregnated with magnetic particles, and is chosen due to both its simplicity and its potential to mimic behavior of biological cilia. The second is a long ribbon-shaped cilium with finite width and negligible thickness, and is chosen because such structures can be manufactured through simple deposition of a thin film of metal, maintaining high flexibility to allow for cilia-like behavior.

3.2.1 Filament Cilia

In the flexible filament cilia model (57), cilia are modeled as a system of LSM nodes arranged on a 3-D square lattice (70, 71), such that they form filaments of square cross section and an aspect ratio of 10, as portrayed in Figure 3.5. The two lowest rows of nodes

are fixed in space in order to impose a clamped boundary condition at the point of elastic cilium attachment to the microchannel wall. The cilia are arranged on the floor of a fluid-filled microchannel in a rectangular pattern with horizontal spacing δx and δz in the x - and z - directions, respectively (Figure 3.5a). Periodic boundary conditions are used to simulate a large array of cilia in an efficient manner. At the top of the simulation domain, either symmetry or no slip boundary conditions are used, so as to represent microchannels with either cilia on the top and bottom channel walls (Figure 3.5b) or with cilia on the bottom wall only (Figure 3.5c). The cilia are driven by a sinusoidal horizontal force applied either at their tips or distributed along their entire length, causing them to periodically oscillate from their vertical equilibrium position.

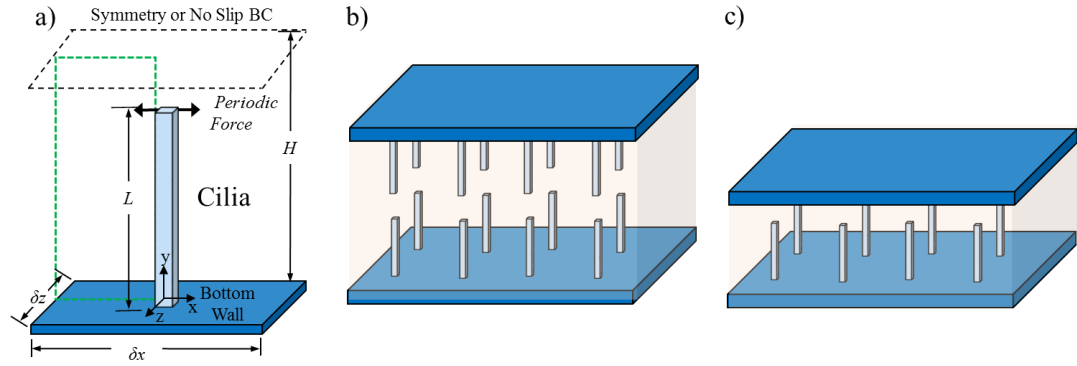


Figure 3.5 a) Periodic simulation domain, consisting of single elastic cilium actuated by a periodic force applied horizontally either distributed across its length or concentrated at its tip. b) Schematic of a fluid-filled microchannel with periodic arrays of cilia on the top and bottom walls. c) Schematic of a fluid-filled microchannel with a periodic array of cilia on only the bottom wall

The bending pattern and deflection of the cilia are defined by two dimensionless parameters. The sperm number, $Sp = L(\zeta\omega/EI)^{0.25}$, shows the ratio of viscous to elastic forces on the oscillating cilia, and defines the bending pattern of the cilia. Here, L is the

cilia length, ζ is the lateral drag coefficient of the cilia (defined here as $\zeta = 4\pi\rho\nu$), ν is the kinematic velocity of the fluid, ω is the driving force oscillation frequency, and EI is the bending rigidity of the cilia. The dimensionless force, $A = KFL^2/EI$, defines the deflection of the cilia, where F is the amplitude of the oscillatory force driving the cilia and K is a constant whose value depends on the location of the applied force ($K = 1/3$ when the force is applied to the cilium tip, and $K = 1/8$ when it is distributed across the cilium length).

3.2.2 Ribbon Cilia

The second type of ciliated system utilizes an array of long, thin ribbon-shaped cilia, which can be fabricated through deposition of a thin layer of soft ferromagnetic metal, such as NiFe. These cilia are fastened to the channel floor, and in the absence of external forcing have an upward curvature due to thermal stresses from the manufacturing process. In the presence of a uniform magnetic field, such as that provided by a permanent magnet, the cilia experience magnetic moments that serve to attempt to align them with the magnetic field. Thus, cilia can be manipulated through rotation of an external magnetic field.

We model each cilium as a 2-D triangular lattice array of mass points connected by harmonic springs, forming a continuous linearly elastic array of triangular thin surfaces as shown in Figure 3.6a. Our triangular lattice leads to isotropic behavior with Poisson ratio $\nu = 1/3$, stiffness k_s , bending stiffness k_b , and one-dimensional beam bending rigidity EI . The ribbon-shaped cilia under consideration have an width of $w = 0.1L$ and negligible thickness. They lay down horizontally, and curve upward under zero loading

conditions, as shown in Figure 3.6a. In order to model this curvature, we apply a constant internal bending moment on the LSM lattice using the method of Yeh and Alexeev (72). In this method, forces are applied to the nodes in each bending unit that is parallel to the cilium axis. For each such bending unit jik , centered on node i as in Figure 2.2a, forces are applied to nodes j and k in the direction normal to the local cilium surface, and a force equal and opposite to the forces at nodes j and k is applied at node i , resulting in zero net force on the cilium, but yielding a moment that acts to give the cilium local curvature, as seen in Figure 3.6a.

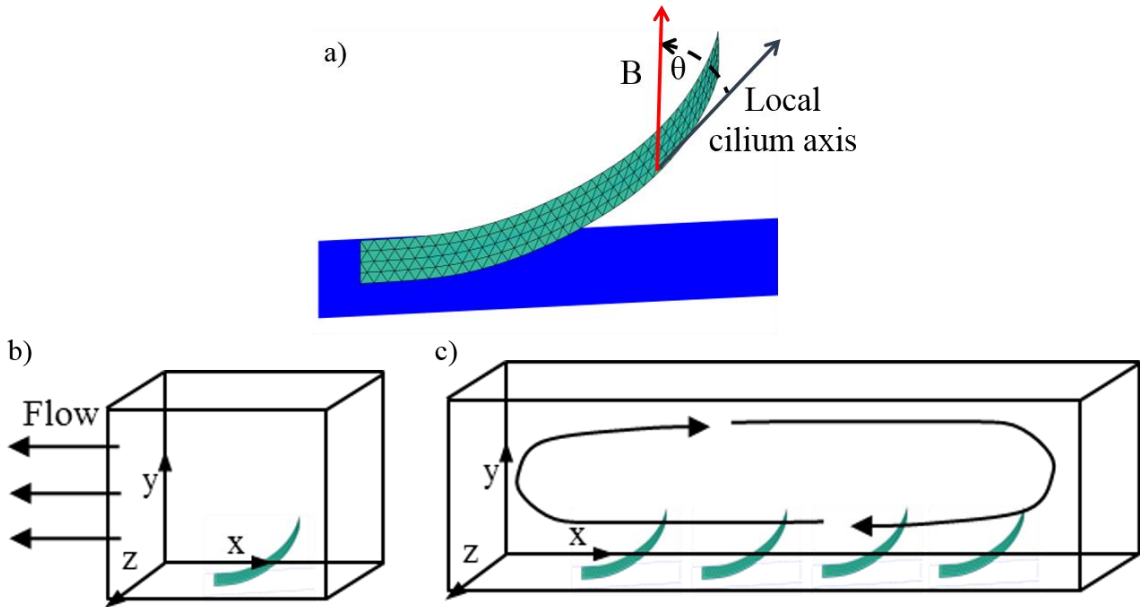


Figure 3.6 a) Model of ribbon-shaped cilium. b) Periodic simulation domain for pumping and dynamics simulations. The top and bottom sides of the domain are solid walls, while the remaining sides are periodic, representing a large array of cilia pumping in the x -direction. c) Simulation domain for study of generation of circulatory flow in a channel of finite width. Here, the domain is periodic in the z – (axial-) direction, while there are solid walls on the edges in the x – (transverse) and y – (vertical) directions

In order to model the magnetic actuation of cilia, we approximate our system to be subjected to a uniform magnetic field producing moments on the cilia. As will be seen in chapter 5, these approximations capture the major physical mechanisms in the system, although it is reasonable to expect some differences between experimental results and those obtained using our computational model. We model magnetic moments on the cilia as a series of dynamically changing moments applied locally in the same manner as explained in the previous paragraph. Here, the value of the moment is time-varying, proportional to $\sin(2\theta)$, where θ is the angle between magnetic field \mathbf{B} and the local axis of the cilium (13). More specifically, the applied magnetic moment is given by $M_c = A_m \sin(2\theta)$, where $A_m = Mn^2 EI / Lc_m$. Mn is the magneto-elastic number $Mn = L \left(|\mathbf{B}|^2 wT / EI \mu_0 \right)^{1/2}$, which gives the balance between magnetic and elastic forces on the cilia. Here, w and T are the width and thickness of the cilia, respectively, and μ_0 is the permeability of free space. Finally, c_m is an empirical constant obtained through experiments due to uncertainties in experimentally applied forcing.

Additionally, cilia behavior is characterized once again using the Sperm number, $Sp = L(\zeta\omega/EI)^{0.25}$, where in this case ω is the frequency of oscillation of the cilia. Due to the angle-moment relationship being proportional to $\sin(2\theta)$, the cilium will beat two times for every rotation of the magnetic field. Collectively, Mn and Sp characterize the balance between the magnetic, elastic, and viscous forces on the cilia, thus accounting for the governing forces for this system, in which inertial forces are negligible due in great part due to its small size.

We use this model in two basic configurations. In order to efficiently simulate cilia dynamics and microfluidic pumping, we use a periodic simulation domain (Figure 3.6b) where the top and bottom sides of the domain are solid walls, while the remaining sides are periodic, representing a large array of cilia patterned on the microchannel floor, pumping in the negative x-direction. Study of the generation of large-scale transverse circulatory flows requires a microfluidic channel with a finite width. Thus, we also perform simulations with a finite channel width with a varied number of cilia stretching across the floor of the channel (Figure 3.6c). Here, the domain is periodic in the z- (axial-) direction, while there are solid walls on the edges in the x- (transverse) and y- (vertical) directions. This allows the cilia to drive fluid across the channel, generating a transverse fluid flow.

3.2.3 *Mixing Model*

In order to investigate the use of filament cilia for mixing of vertically stratified fluid layers in a microfluidic channel with a ciliated bottom wall and a bare top wall, we use a scalar transport LBM to model transport of concentration of a solvent in the microfluidic channel. We use two initially stratified layers each with uniform concentration, $C_i(0)=0$ and $C_i(0)=1$ at each fluid node in the bottom and top halves of the microchannel, respectively, as depicted in Figure 3.7. Once we have calculated the concentration field in the system, we calculate the mixing level of the fluid in the system using equations 3.5 and 3.6.

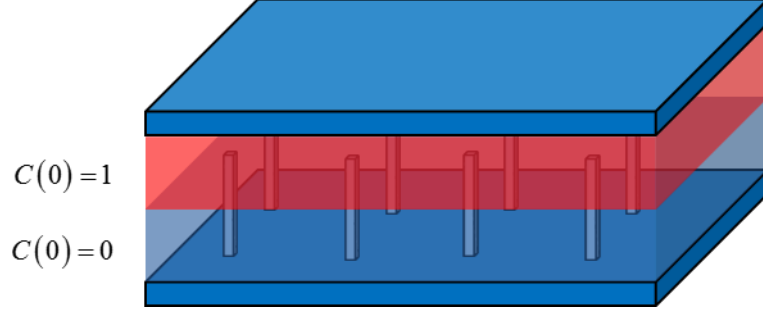


Figure 3.7 Schematic of a microfluidic channel with a ciliated floor and bare ceiling filled with a viscous fluid. The fluid contains a solvent with initial concentrations of $C_i(0)=0$ and $C_i(0)=1$ at nodes on the bottom and top halves of the channel, respectively

3.2.4 Nano-Particle Deposition Model

We model the effect of actuated synthetic filament cilia on deposition of nano-particles onto ciliated sensory surfaces (57) on the top and bottom walls of a microchannel (Figure 3.5b) using the BD model. In the simulations reported here, we use 10^4 particles. We assume that the cilia surface is perfectly reflective of the particles. In this case, the particles do not deposit on the cilia. To impose this condition, we reflect the particles off of the cilia by reversing the component of the particle velocity that is normal to the cilia surface. We apply a reflective boundary at the top of the domain, and periodic boundary conditions in the horizontal directions (Figure 3.5a). At the bottom of the domain representing the bottom microchannel wall, any particle that crosses the boundary is assumed to be deposited, thereby simulating perfectly adsorptive walls. This assumption is valid in the situations when the number of adsorption sites is much larger than the amount of deposited nano-particles and/or nano-particles can bind to each other forming continuous deposit layers. We track nanoparticle deposition and calculate the fraction of particles deposited on the microchannel walls in the course of the simulations to assess the

effect of beating cilia on this process. The behavior of this system for particle transport can be characterized using the Schmidt number, $Sc = \nu/D_0$, which gives the relative importance of momentum diffusion to particle diffusion in mass transport within the system.

3.3 Model Validation

The hybrid LBM and LSM model has been extensively validated and used as an FSI model for the study of a variety of physical phenomena (42, 54, 55, 72-80), but herein we provide validation cases to show that this model can accurately capture large deformations of the cilia in our models, as well as to validate our mass transport models. For validation of the hybrid LBM and LSM model for flow over spheres, see the work of Mao (53). In addition to the validation cases provided in this section, in chapters 4 and 5 we provide comparison to experimental results, where applicable.

3.3.1 *Filament Cilia Deflection*

In order to understand the ability of our LSM model to capture the physics of our model filament cilia when they are subjected to forces large enough such that they experience large deformations, we performed validation tests in which we applied constant horizontal force F to the tip of the vertical cilium, and calculated the resulting deflection. Although there is no closed-form analytical solution to the large-deflection cantilevered beam problem, it can readily be solved using an integral approach using the method of Chen (81). This method takes advantage of the fact that the curve length of the beam, s , is given by

$$\frac{ds}{dy} = \frac{1}{\sqrt{1 - \left(\frac{F}{EI}\right)^2 \left(ly - \frac{y^2}{2}\right)^2}}, \quad (3.7)$$

where l is the length of the curved beam in the y – (vertical-) direction. For a given value of l , this equation is readily integrated numerically, using a method such as the trapezoidal rule with sufficient spatial resolution. Thus, the arc length $s(l)$ can be found for each value of l . Since $s(l)$ is a monotonic function of l , we can easily scan the entire range of l by starting with a low value of l and then increasing l until we meet the condition $s(l) = L$, indicating that the arc length considered is the entire length of the beam. With the correct value of l for the entire curved beam, the entire bending curve can be calculated through numerical integration of the following equation at each point y :

$$\frac{dx}{dy} = \frac{\frac{F}{EI} \left(ly - \frac{y^2}{2}\right)}{\sqrt{1 - \left(\frac{F}{EI}\right)^2 \left(ly - \frac{y^2}{2}\right)^2}}. \quad (3.8)$$

As shown in Figure 3.8, our LSM model gives a reasonably good approximation of the deflection, δ , of a flexible beam, even up to a deflection of over 50%. For this high deflection, the tip deflection is underestimated by less than 5%. This difference can be attributed to a relatively small number of LSM nodes across the cilia. Indeed only 4 nodes were used in the simulations, so as to allow for efficient simulation of high-aspect-ratio cilia. Between this finding and the ability of our model to recreate cilia beating

phenomena (8, 70, 82) as will be shown in chapter 5, we determine that our filament cilia model is sufficient to model cilia mechanics with reasonable accuracy.

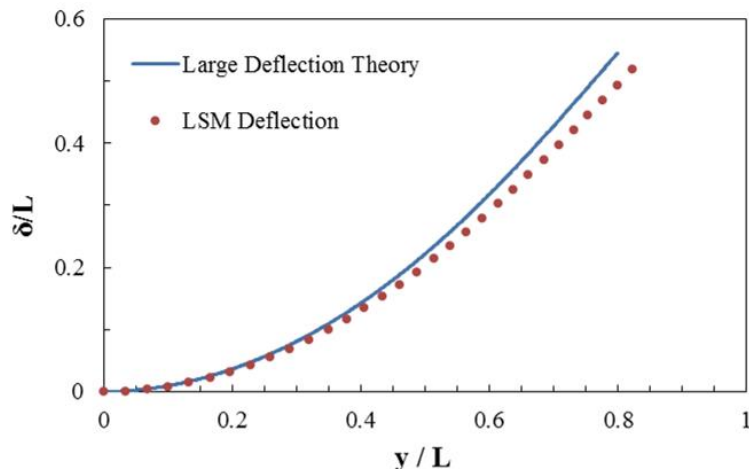


Figure 3.8 Deflection (δ) of a beam cantilevered in the vertical- (y -) direction and subjected to a force concentrated at the beam tip. This shows that LSM captures cilium deflections of over 50% with less than 5% relative error

3.3.2 Ribbon Cilia Deflection

Since the ribbon cilia are also subjected to forcing that results in large deformations, we perform similar validation on that model. As these cilia are not forced at the tip, but are instead actuated along their entire lengths, we performed validation tests of vertically cantilevered ribbon cilia subjected to constant and uniformly-applied force distribution F , but with no internally-applied moments. A large-deflection beam theory can be applied in similar fashion as was done in section 3.3.1. However, in this case equations 3.7 and 3.8 should be replaced by the following:

$$\frac{ds}{dy} = \frac{1}{\sqrt{1 - \left(\frac{F}{2EI}\right)^2 \left(\frac{y^3}{3l} - y^2 + ly\right)^2}}, \quad (3.9)$$

and

$$\frac{dx}{dy} = \frac{\frac{F}{2EI} \left(\frac{y^3}{3l} - y^2 + ly\right)}{\sqrt{1 - \left(\frac{F}{2EI}\right)^2 \left(\frac{y^3}{3l} - y^2 + ly\right)^2}}. \quad (3.10)$$

As given in Figure 3.9, our LSM ribbon cilia model provides an accurate solution of the large deformation of cilia. In this case, there was even less error in the deflection solution than was seen with the filament cilia, as the deflection was overestimated by less than 3%.

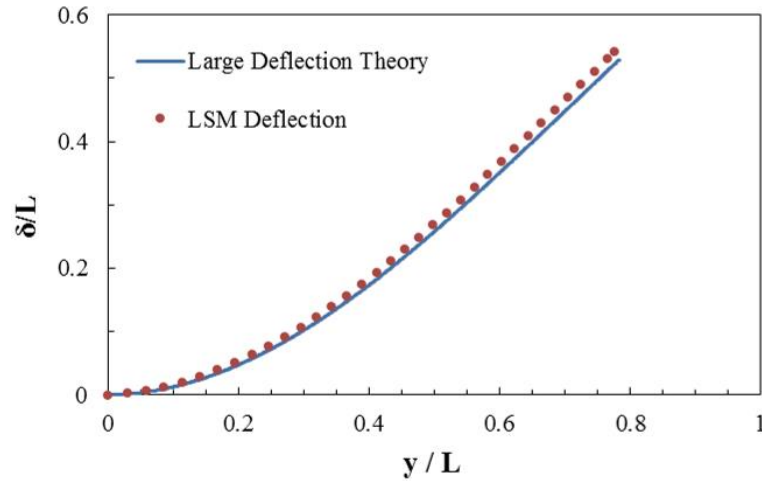


Figure 3.9 Deflection (δ) of a beam cantilevered in the vertical- (y -) direction and subjected a force distributed evenly along its length. This shows that LSM captures cilium deflections of over 50% with less than 3% relative error in the ribbon cilium model

3.3.3 Validation of Mass Transport Models

In order to validate both the BD model and the scalar transport LBM model, we performed a simulation test case using both models. In this test case, we simulated a channel of appreciable width W containing a viscous fluid with initial solute concentration of $C(y < W/2, t = 0) = 0$ on one side and $C(y > W/2, t = 0) = 1$ on the other, as seen in Figure 3.9a. Simulations were run in stagnant flow, and the resulting concentration profile evolution was compared to an analytical solution for cross-channel diffusion of particles in a dilute liquid solution at constant temperature and pressure with no reactions and zero fluid velocity. This analytical solution is derived from the diffusion equation with boundary conditions $C(y \rightarrow -\infty, t) = 0$ and $C(y \rightarrow \infty, t) = 1$ and is given as

$$C(y, t) = \frac{1}{2} \left[1 + \operatorname{erf} \left(\frac{y}{2\sqrt{D_0 t}} \right) \right]. \quad (3.11)$$

As seen in Figure 3.10b, both the BD model and the scalar transport LBM model were able to accurately calculate the concentration profiles in the channel at a variety of points in time. Thus, we conclude that both models accurately calculate mass transport by diffusion.

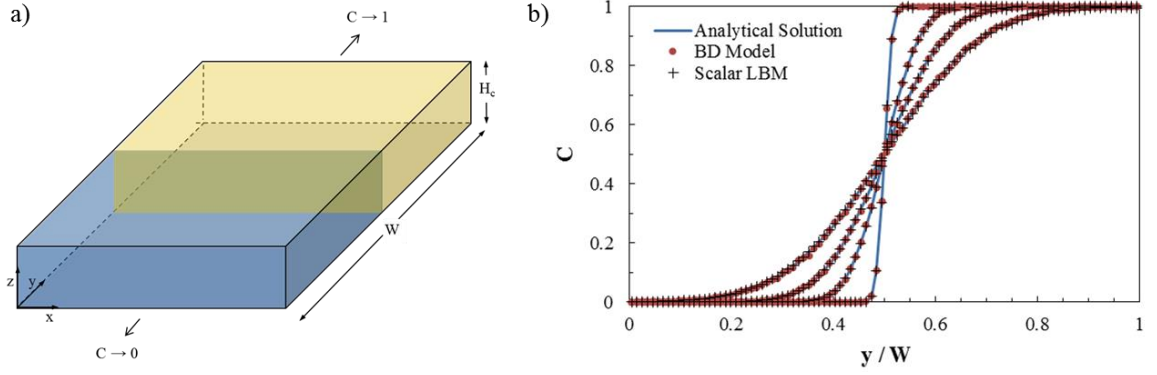


Figure 3.10 a) Schematic of the initial concentration profile used in the test case to validate the mass transport models used in this work. b) Concentration profiles showing the time-evolution of a solute in the microchannel, as calculated using the analytical solution, BD model and scalar transport LBM model. Each curve represents a separate point in time

In order to further validate the BD model for use in the study of synthetic cilia for enhancement of nano-particle deposition, we validated our model against an analytical solution of the deposition fraction of diffusive particles in a microfluidic channel by integrating a solution to the diffusion equation. The fraction of particles deposited on the channel walls, denoted by P , is given by

$$P = 1 - \frac{2}{\pi^2} \sum_{n=1}^{\infty} \frac{(1 - (-1)^n)^2}{n^2} e^{(-n^2 t / \tau)}, \quad (3.12)$$

where $\tau \equiv H^2 / D_0 \pi^2$ is the diffusion time scale. The equation is obtained subject to boundary conditions of zero concentration at the channel walls (perfectly adsorptive walls) and an initial condition of a uniform concentration throughout the channel at time $t = 0$.

Figure 3.11 shows that the amount of deposited particles steadily increases with time. This figure also compares the theoretical predictions with the results of our BD model for the case of a microchannel without cilia at various values of Sc . The results of simulations

match closely with the analytical solution, indicating that our computational model correctly predicts diffusive transport and particle deposition in a microchannel. This gives us a baseline for nano-particle deposition in a microchannel without cilia, and gives us confidence that our calculations of mass transport due to cilia will be accurate.

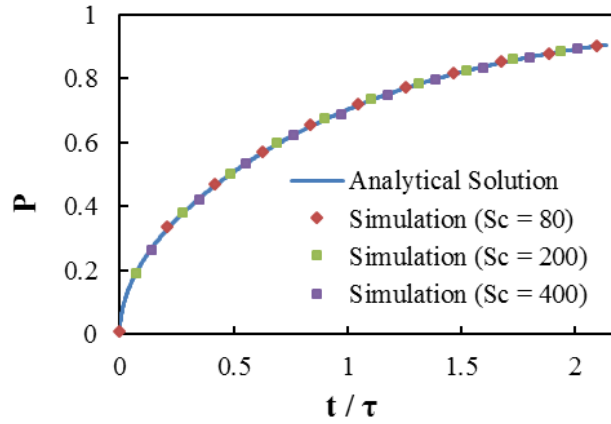


Figure 3.11 Diffusive deposition of nano-particles in a microchannel without cilia. Here the analytical solution is compared to results obtained using the BD model at various values of Sc

Finally, in order to verify that the BD model accurately tracks the movement of tracer particles without appreciable errors due to boundary conditions or velocity interpolation, we performed a test case designed to test the model's ability to reproduce behavior seen at low Re flows in which fluid has a 'memory,' and returns to its original location if subjected to time-reversible motion of a solid object in the fluid (3).

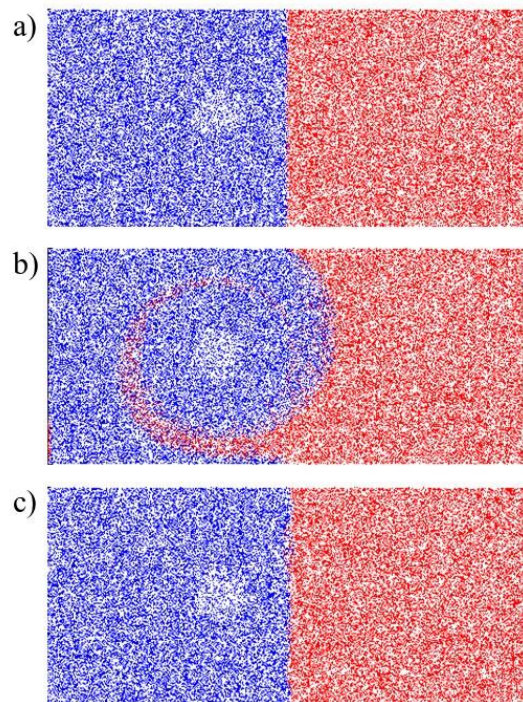


Figure 3.12 Time evolution of the locations of mass-less non-diffusive tracer particles subjected to a magnetic microbead orbiting clock-wise through them in the channel, then exactly retracing its complete path. a) Initial distribution of particles. b) Distribution of particles after 14 clock-wise orbits. c) Distribution of particles after the entire process

In the test case, a magnetic microbead was moved in an orbit crossing the interface between two regions that initially contained separated solutions of two different species of tracer particles (which did not experience diffusion), as shown in Figure 3.12a. The microbead was moved so as to complete 14 clock-wise orbits, and was observed to drag tracer particles in a circular pattern in its wake, as seen in Figure 3.12b. The bead trajectory was then exactly retraced, such that it moved in 14 counter-clockwise orbits. This resulted in the particles returning almost exactly to their original locations without any visibly noticeable changes, as seen in Figure 3.12c. At the end of this process, error in particle location was calculated to be only 0.06% as compared to the distance that the bead travelled before reversal. This indicates that our model accurately calculates the effect of flow

around moving solid structures on particle movement, and along with our validation of the model for calculating diffusion, gives us confidence that our model will accurately calculate diffusive mass transport in complicated flows around solid structures.

3.4 Summary

We developed computational models based on the methodologies in chapter 2 so as to approximate two specific types of magnetically actuated microfluidic systems. Specifically, we modelled orbiting magnetic microbeads for applications in microfluidic mixing and particle capture. We also modelled bio-mimetic cilia for use in microfluidic mixing, pumping and nano-particle capture. We validated our models using basic test cases, and are now ready for application of our models in a detailed study of the physical mechanisms involved in the function of these systems and of their optimization for application in microfluidic mixing and particle capture.

CHAPTER 4. MICROFLUIDIC MIXING AND PARTICLE CAPTURE USING ORBITING MAGNETIC MICROBEADS

Herein, we use 3-D numerical simulations to study the dynamic behavior of a multi-functional device that performs microfluidic mixing and microscale particle capture using magnetic microbeads which are moved in controlled orbits on the floor of a microfluidic channel. We study the physical mechanisms of mixing and capture, and determine the effect of system parameters on these processes.

4.1 Beads Dynamics and Resulting Flow

The magnetic microbeads under study are driven in controlled orbits around NiFe discs patterned onto a microfluidic channel floor, so as to sweep through the fluid in the channel. The beads are pulled magnetically to poles on the NiFe disc, such that they tend to equilibrium positions on either side of the disc. The locations of the magnetic poles on each NiFe disc rotate around the disc to maintain alignment with an applied external magnetic field, such that rotation of an external magnetic field results in rotation of the magnetic poles around each NiFe disc, and thus in controlled orbits of magnetic beads around each NiFe disc on the microchannel floor. Owen et al (4) previously demonstrated this method experimentally, and used a computational model to simulate microbead dynamics. They found that beads follow predictable trajectories in circular orbits around NiFe discs when the magnetic forces on the beads are greater than the hydrodynamic forces experienced by the orbiting beads.

Our further analysis of the bead orbit trajectories shows that in the range of velocities for which hydrodynamic forces are relatively small compared to magnetic forces, which is required for reliable magnetic control of microbeads, the bead trajectories do not change appreciably with varied bead velocities or magnetic field flux densities. Our simulations of beads orbiting at rotation rates ranging from 2,500 – 10,000 RPM and driven by an external magnetic field with flux densities ranging from 0.088 - 0.18 T reveal that the beads with diameter $a = 2.8\mu$ orbit discs of diameter $D_d = 3\mu m$ at a radius of approximately $1.86a$, which closely matches experimental findings. Thus, we can simplify simulations by first calculating trajectories of microbeads induced by a rotating magnetic field, and then imposing the bead trajectories directly through prescribing their velocity. This allows the simulations of mixing and particle capture to be significantly accelerated.

We examine the flow patterns generated by magnetic microbeads orbiting in a microfluidic channel to understand the physical origin of fluid mixing induced by rotating microbeads (60). Our simulations show that the orbiting magnetic beads create a time-varying three-dimensional flow pattern, a snapshot of which is shown in Figures 4.1a-c. Beads drag fluid in the horizontal plane in which they orbit, and the effect of the beads on the flow is greatest in the direct vicinity of the beads, although the beads also drag to a lesser extent the fluid located at a height of several times the bead size. When a net flow down the channel is added, the combined effect of this net flow with the orbiting beads causes the generation of dynamically changing lanes of fluid (Figure 4.1a), resulting in flow winding back and forth between oncoming beads on subsequent rows and allowing much of the fluid to come in close contact with beads, which has implications in the effectiveness of particle capture. The ratio of the average axial flow velocity U_x to the

bead orbit velocity V_b has a profound effect on the generated flow patterns, as well as the effectiveness of the beads in microfluidic mixing and particle capture, as will be seen hereafter.

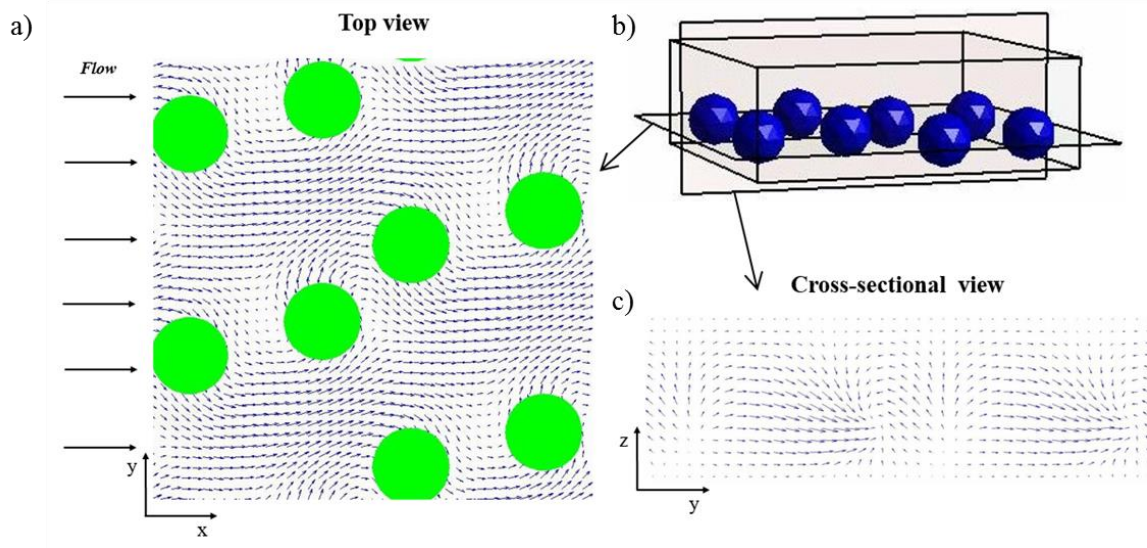


Figure 4.1 Instantaneous velocity fields generated by beads orbiting counter-clockwise in a microchannel with flow giving $U_x/V_b = 1$. a) Top view of the velocity field. Four pairs of beads are seen rotating counter-clockwise in a section of a microchannel, and velocity vectors at the half-height of the beads are given. b) Schematic showing the orientation of planes in which velocity fields are shown. c) Velocity field at a planar cross-section looking down the channel shows vertical flow due to magnetic microbeads

In addition to horizontal flow, the beads generate vertical flow (Figure 4.1c) due to the creation of regions of high and low pressure at the leading and trailing ends of the beads, respectively. This allows some of the fluid from the top of the channel to come down to the beads located at the bottom of the channel.

We find more insights into the generated flow pattern by examining the streamlines of the period-averaged velocity field of the flow created by orbiting microbeads. Beads orbiting in an otherwise stagnant fluid generate circulation patterns around NiFe discs, as

seen in Figure 4.2a. Additionally, the circulation pattern cells are linked by streamlines on which fluid is advected from cell to cell across the channel. Physically, this occurs due to the beads dragging fluid that is left in their wake and picked up by the wake of beads orbiting adjacent discs, bringing the fluid to the next circulation cell. As we discuss later, this is important to microfluidic mixing using orbiting magnetic microbeads.

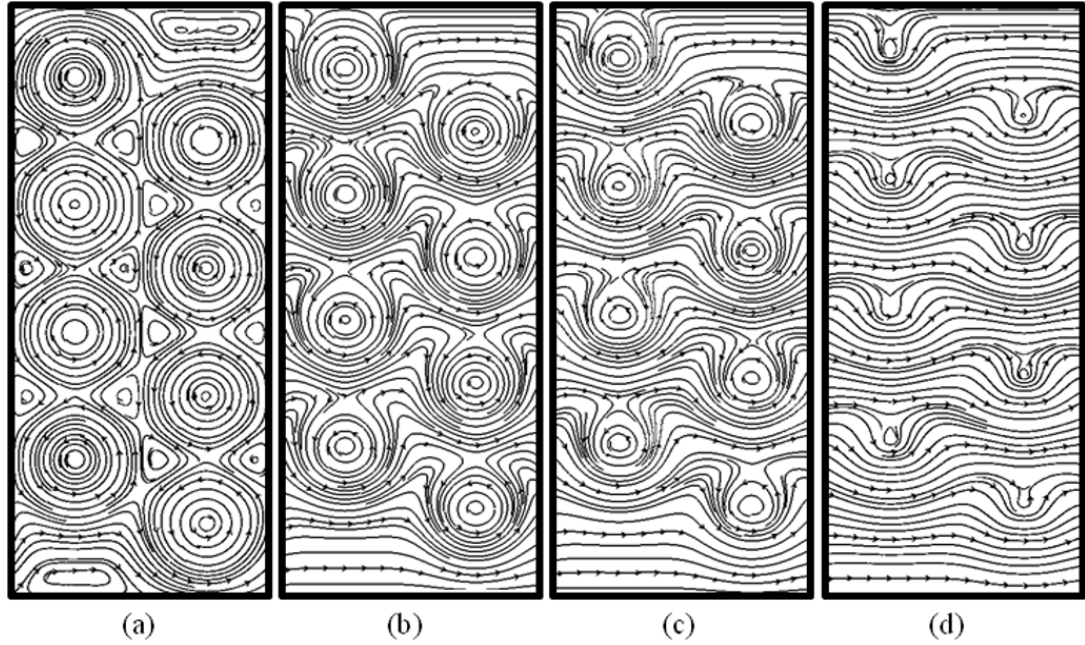


Figure 4.2 Streamlines of the period averaged fluid velocity at the plane located at the center height of the magnetic microbeads orbiting in a microchannel at the following velocity ratios: a) $U_x/V_b = 0$, b) $U_x/V_b = 0.3$, c) $U_x/V_b = 0.6$, and d) $U_x/V_b = 1.4$

As a net flow velocity is introduced and the velocity ratio increases, fluid left in the wake of orbiting beads is advected downstream out of the trajectory of the oncoming bead, which leads the circulatory cells to shrink and streamlines linking cells across the channel to disappear by $U_x/V_b = 0.3$ (Figure 4.2b). As the velocity ratio is further increased, the circulatory cells continue to shrink (Figure 4.2c), and are almost non-existent at high velocity ratios (Figure 4.2d), leaving primarily axial period-averaged flow down the

channel. With the lack of period-averaged transverse flow, bulk advection of fluid across the channel is suppressed at higher velocity ratios.

4.2 Microfluidic Mixing

4.2.1 *Mixing by Orbiting Beads*

In order to validate our numerical model, we compare our results with experimental data published by Ballard et al. (60). Those experiments were performed with fluid streams flowing via EOF at axial velocity $U_x \approx 50 \text{ } \mu\text{m/s}$ through a $300 \text{ } \mu\text{m}$ -long region of a microfluidic channel containing magnetic microbeads orbiting at 4500 RPM, such that the ratio of the flow velocity to the bead linear velocity V_b was $U_x/V_b \approx 0.03$. As seen in Figure 4.3a, separated streams of fluid with (white) and without (black) fluorescent nanoparticles were mixed rapidly over a compact mixing distance. Here, the streams had already blended somewhat due to molecular diffusion in the lengthy microchannel leading up to the mixing section, as is apparent from the gradual transition from white to black across the channel at the inlet. Mixing in this experimental device is visibly evident from the light and dark sections at the inlet merging in the mixing section, so that the fluid in the channel becomes grayer at the outlet. Additionally, experimental mixing resulted in circular rings of dark and light in the regions of bead orbit around discs (black spots in the image), leading across the channel. Numerical simulations (Figure 4.3b) of mixing under the same conditions as in the experiments of Figure 4.3a qualitatively match experimental results, with similar circular patterns across the channel and a mixing layer growing at a similar rate as was seen in the experiments. Non-uniformities in the experimental fluid led to a more jagged experimental mixing profile within the mixing section (Figure 4.3a) than was

seen in simulations (Figure 4.3b). In order to reduce the effect of these non-uniformities on further analysis, six separate experimental images taken under these conditions were analyzed and averaged for fluorescence intensity at each distance across the channel. As seen in Figure 4.3c, experiments and simulations yielded quantitatively similar concentration profiles (manifest as fluorescence intensity in experiments) across the channel at the outlet.

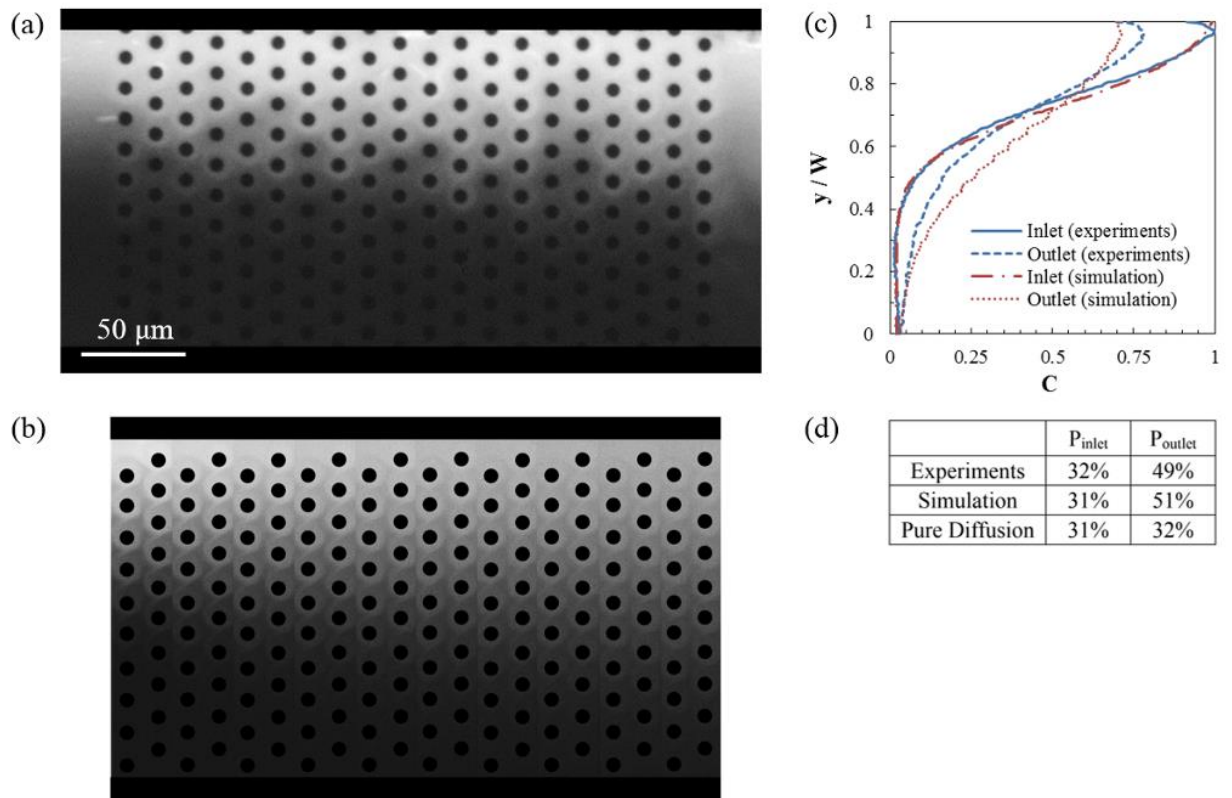


Figure 4.3 a) Rapid mixing in an experimental micromixer. Streams of fluid with (white) and without (black) fluorescent nano-particles are mixed as they pass through a 300 μm mixing region. b) Simulation of mixing, made up of a series of images of the time evolution of the vertically averaged concentration field, each placed at the location corresponding to the distance fluid has moved downstream in the simulation. c) Profiles of concentration variation across the channel width at the inlet and outlet, shown for both experimental and simulation data. d) Summary of the calculated percentage of mixing, P , at the inlet and outlet of the mixing region for experiments, simulations, and a simulated channel with no microbeads, such that mixing occurs purely due to molecular diffusion over the length of the mixing region

The levels of mixing calculated at the inlet and outlet in experiments and simulations, as well as for a channel without orbiting microbeads, are given in Figure 4.3d. In the experiments, the fluid streams entered the mixing section 32% mixed, and were 49% mixed at the outlet. Our simulations showed similar mixing levels, with the fluid streams 31% and 51% mixed at the inlet and outlet, respectively. In the absence of orbiting magnetic microbeads, very little mixing would occur over the short distance of the mixing region. Indeed, we calculated that without orbiting microbeads fluid streams entering the mixing region 31% mixed to still only be 32% mixed at the outlet.

Thus, we see that orbiting magnetic microbeads mix fluid streams at a rate that is greatly accelerated compared to molecular diffusion, and that our numerical model yields results that both qualitatively and quantitatively match the experimental results. We must note that the conditions and mixing section length used in these experiments are not optimized for the fastest mixing, but instead provide a means of validating our computational model. Even more rapid mixing can be achieved by tuning flow conditions or the length of the mixing region, as will be discussed below. A detailed experimental investigation of fluid mixing by orbiting magnetic microbeads at the limit of low velocity ratios was published by Owen et al (61).

In order to utilize orbiting magnetic microbeads to most efficiently mix fluid streams in a microfluidic channel, it is important to understand how various parameters affect mixing performance. In order to compare the effectiveness of orbiting microbeads to the mixing that occurs purely due to diffusion, we introduce a mixing enhancement parameter defined by

$$E_P = \frac{t_D}{t_E}, \quad (4.1)$$

where E_P is the acceleration of mixing of the fluid streams to P percent mixed by beads as opposed to mixing by diffusion alone, and t_D and t_E are the amounts of time required to reach P by diffusion alone and when mixing is enhanced by orbiting microbeads, respectively. The parameter definition is illustrated in Figure 4.4 for $P = 70\%$. In this case the mixing enhancement by magnetic beads leads to $E_{70\%} = 25.5$, meaning that the orbiting microbeads cause the fluids to reach 70% mixing 25.5 times faster than would happen due to molecular diffusion alone.

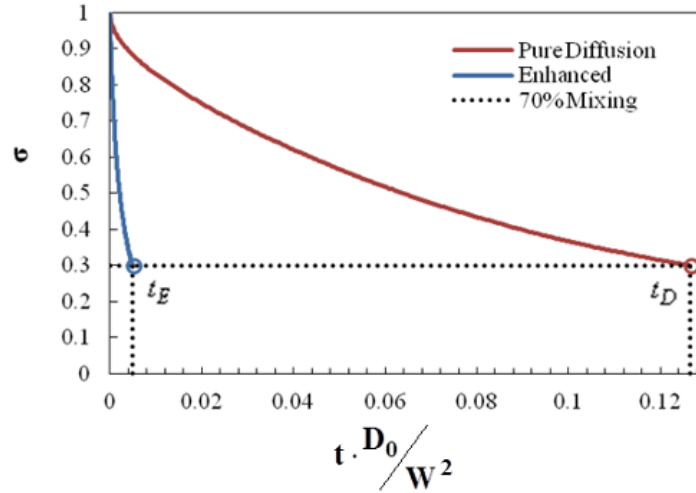


Figure 4.4 Plot of the degree of mixing over dimensionless time for the case of no microbeads (pure diffusion) and of mixing enhanced by orbiting magnetic microbeads. 70% mixing occurs at times t_D and t_E for the pure diffusion and enhanced cases, respectively

The configuration of NiFe discs and orbiting microbeads in the microfluidic channel, as shown in Figure 3.2, affects the mixing performance of the magnetic micromixer. In order

to explore the effect of NiFe disc placement, we performed numerical simulations with the channel height, channel width and NiFe disc diameter fixed at $H_c = 2a$, $W = 14a$ and $D_d = a$, respectively, with constant $Pe_b = 500$, and varied the edge to edge spacing S between NiFe discs and the offset angle θ between rows of beads over a wide range of velocity ratios. Simulations show that mixing enhancement increases monotonically with decreasing S , as evidenced by the curves in Figure 4.5a. We note that in our simulations we consider configurations in which a pair of beads orbits each disc. The minimum possible spacing between neighboring discs is limited by the fact that the orbiting beads must have enough clearance to not hit adjacent discs or beads. Experiments showed that for two beads to orbit a single NiFe disc at opposite poles, as shown in Figure 3.2, there must be enough space between adjacent discs, $S \geq 2a$, so that the beads will not collide with each other. For more tightly spaced NiFe disc arrays, only a single bead can orbit around each NiFe disc. Moreover, if the spacing is further decreased, then even single beads will not be able to orbit predictably around a NiFe disc due to the effect of adjacent discs.

As shown in Figure 4.5a, simulations performed over a wide range of velocity ratios show that decreasing the spacing to $S < 2a$, such that only one bead orbits each NiFe disc, significantly reduces mixing performance as compared to the case where two beads orbit each NiFe disc with an increased spacing of $S = 2a$. This improvement is most exaggerated at high velocity ratios, where interactions between successive rows of beads are important. In this case, a second bead orbiting the discs passes by the first bead of the adjacent row, and serves to transport some of the fluid further across the channel, rather than allowing it to return back to its original location with the bead. We will therefore focus on the configurations allowing a pair of magnetic beads to orbit each NiFe disc.

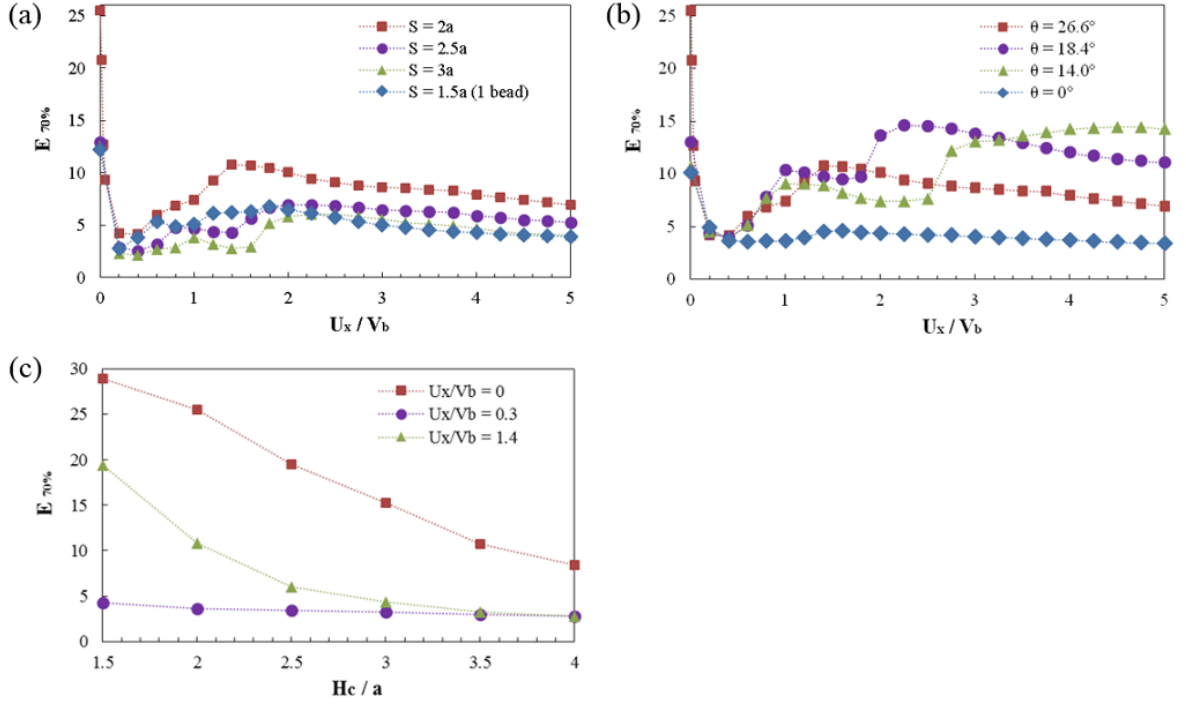


Figure 4.5 Plots of mixing enhancement over a range of velocity ratios for different configurations. a) Arrays with channel height $H_c = 2a$ and two alternating offset rows of discs ($\theta = 26.6^\circ$) with the following values of disc spacing: \blacksquare $S = 2a$, \bullet $S = 2.5a$, \blacktriangle $S = 3a$, and \blacklozenge $S = 1.5a$ (one bead per disc). b) Arrays with channel height $H_c = 2a$, disc spacing $S = 2a$ and discs offset at the following angles: \blacksquare $\theta = 26.6^\circ$ (two alternating offset rows of discs), \bullet $\theta = 18.4^\circ$ (three alternating offset rows of discs), \blacktriangle $\theta = 14.0^\circ$ (four alternating offset rows of discs), and \blacklozenge $\theta = 0^\circ$ (square array of discs). c) Plot of mixing enhancement over a range of channel heights using arrays with $S = 2a$ and $\theta = 26.6^\circ$ at the following velocity ratios: \blacksquare $U_x/V_b = 0$, \bullet $U_x/V_b = 0.3$, \blacktriangle $U_x/V_b = 1.4$

The angle between adjacent rows of beads has a significant effect on mixing performance. Figure 4.5b shows that there is an increase in mixing performance for the case of arrays with NiFe discs in angled patterns created by alternating different numbers of offset rows of discs orbited by two beads, as compared to similar arrays with square patterns of discs ($\theta = 0$ on Figure 3.2), and that this improvement is exaggerated at high velocity ratios. The difference between mixing performance for these configurations is due

to the fact that angled configurations aid the beads in advecting fluid across the channel as fluid moves down the channel from one row of beads to the next offset row, where beads are located further across the channel. The physical mechanism of the increase in mixing performance at high velocity ratios will be discussed in section 4.2.2.

As seen in Figure 4.5b, there is a significant increase in mixing enhancement at high velocity ratios as long as there is a significant offset angle between rows of discs. Notably, the velocity ratio at which the maximum mixing enhancement occurs varies with θ , as the optimal velocity ratio is governed by geometry, as discussed in section 4.2.2. In the rest of this study we focus on a simple array of two alternating rows of offset discs ($\theta = 26.6^\circ$) with spacing $S = 2a$ where each disc is orbited by two microbeads. However, the trends found for this specific array can be directly extended to configurations with other offset angles between rows of discs.

As shown by the curve of squares in Figure 4.5a, the mixing enhancement by the beads in the selected configuration is strongly dependent on the velocity ratio. In the absence of flow through the channel, mixing enhancement is the highest with $E_{70\%} = 25.5$. This result shows that this mixer can effectively be used as a chamber or stop-flow mixer. When we introduce flow through the channel but the bead velocity is still much greater than the flow velocity (low velocity ratio), the mixing enhancement remains large, although it decreases rapidly with increasing velocity ratio. The mixing enhancement is weakest when $U_x/V_b \approx 0.3$. For velocity ratios greater than $U_x/V_b \approx 0.3$, mixing enhancement increases with increasing velocity ratio up to a local maximum that is dependent on θ and S . This dependence is addressed in section 4.2.2. For the configuration used for the rest of our

work, the local maximum in mixing enhancement occurs at $U_x/V_b \approx 1.4$. For higher velocity ratios, enhancement gradually decreases with increasing velocity ratio.

Since the effect of bead motion on the fluid will diminish with increasing distance to the beads, we would expect mixing enhancement to also be dependent on channel height. In order to investigate this dependence, we performed simulations with the channel width, NiFe disc diameter, spacing, and offset angle fixed at $W = 14a$, $D_d = a$, $S = 2a$ and $\theta = 26.6^\circ$, respectively, with constant $Pe_b = 500$, and varied the ratio of the channel height to the bead diameter, H_c/a .

As seen in Figure 4.5c, the mixing enhancement with flows at various velocity ratios decreases with increasing channel height. At $U_x/V_b = 0$ and $U_x/V_b = 1.4$, which velocity ratios were previously found to be the local maxima for mixing enhancement for this geometrical configuration at $H_c/a = 2$, mixing enhancement was high for low H_c/a , but dropped dramatically with increasing channel height. However at $U_x/V_b = 0.3$, which was found to be a local minimum for mixing enhancement, the drop in mixing enhancement with increasing channel height is less pronounced, since at this velocity ratio beads did not mix the fluid nearly as effectively at low H_c/a as they did at other velocity ratios. Thus, we find that decreasing channel height with respect to the bead diameter increases mixing enhancement, but that the amount of increase is dependent on U_x/V_b .

4.2.2 *Mixing Mechanisms*

Examining the concentration fields in microchannels with fluid streams being mixed by beads orbiting at various velocity ratios gives insights into what is occurring during mixing.

From Figure 4.6, which gives the vertically averaged concentration fields in the channel, it is apparent that beads orbiting in an otherwise stagnant fluid drag fluid across the channel in circular patterns similar to those seen experimentally at low velocity ratios (Figure 4.3a), stretching the fluid-fluid interface and resulting in rapid mixing, which can be seen by the greatly increased concentration uniformity in Figure 4.6b as compared to that in the case of mixing purely due to diffusion shown in Figure 4.6a. As flow down the channel increases in relation to the bead orbit velocity, interfacial stretching decreases and this flattened interface leads to the decline in mixing enhancement with increasing velocity at low velocity ratios, as seen in Figure 4.5a. At $U_x/V_b \approx 0.3$ (Figure 4.6c), the point of minimum mixing enhancement, the interface experiences the lowest deformation due to rotating beads. As the flow velocity ratio is further increased, interface deformation is still minimal, but a distinct mixing mechanism serves to increase mixing, as seen by the increasingly wide mixed regions at the middle of the channel in Figures 4.6c-e.

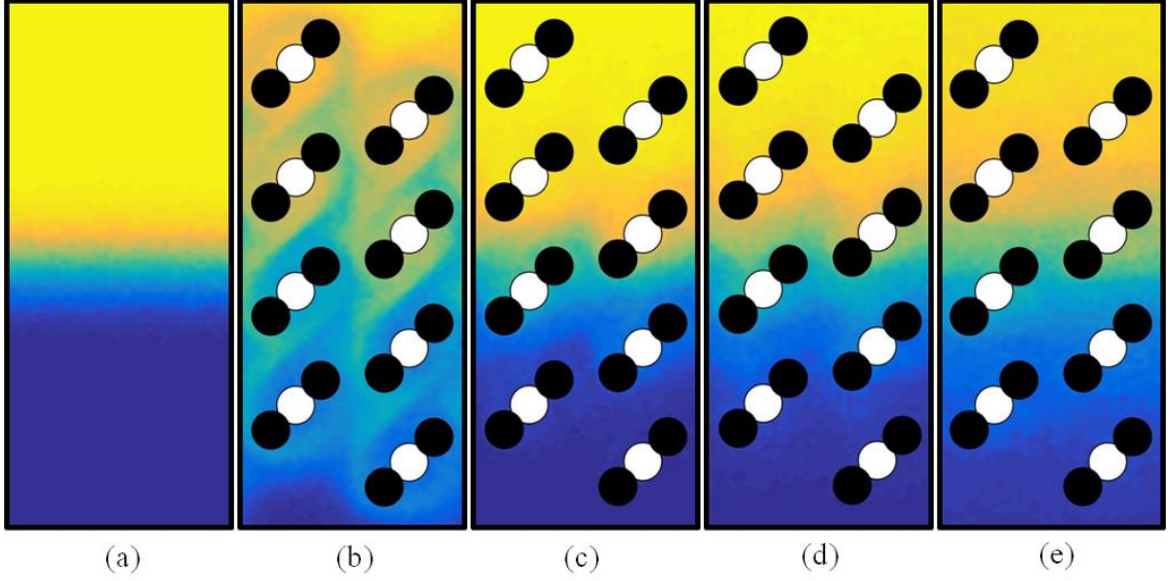


Figure 4.6 Vertically averaged concentration fields in microchannels after mixing a set amount of time $t = 25T$, where T is a fixed bead orbit period. a) Mixing due purely to diffusion (no beads). b – e) Mixing aided by orbiting microbeads at various velocity ratios: b) $U_x/V_b = 0$, c) $U_x/V_b = 0.3$, d) $U_x/V_b = 0.6$, and e) $U_x/V_b = 1.4$

To better understand the physical mixing mechanisms and how they change at different velocity ratios, we performed simulations with non-diffusive tracer particles, thus decoupling particle movement due to advection from movement due to diffusion. Figure 4.7 shows the distribution of tracer particles in a microchannel after 75 orbits of the microbeads at various velocity ratios.

For the case of a microchannel with orbiting microbeads and otherwise stagnant fluid ($U_x/V_b \approx 0$), the beads drag the fluid and accompanying tracer particles in circular streaks that transport the fluid across the channel. Thus, interfacial stretching is caused by advection due to the orbiting beads. This stretched interface then allows diffusion to act over a greatly increased interface length, leading to the high level of mixing enhancement seen at that velocity ratio in Figure 4.5a.

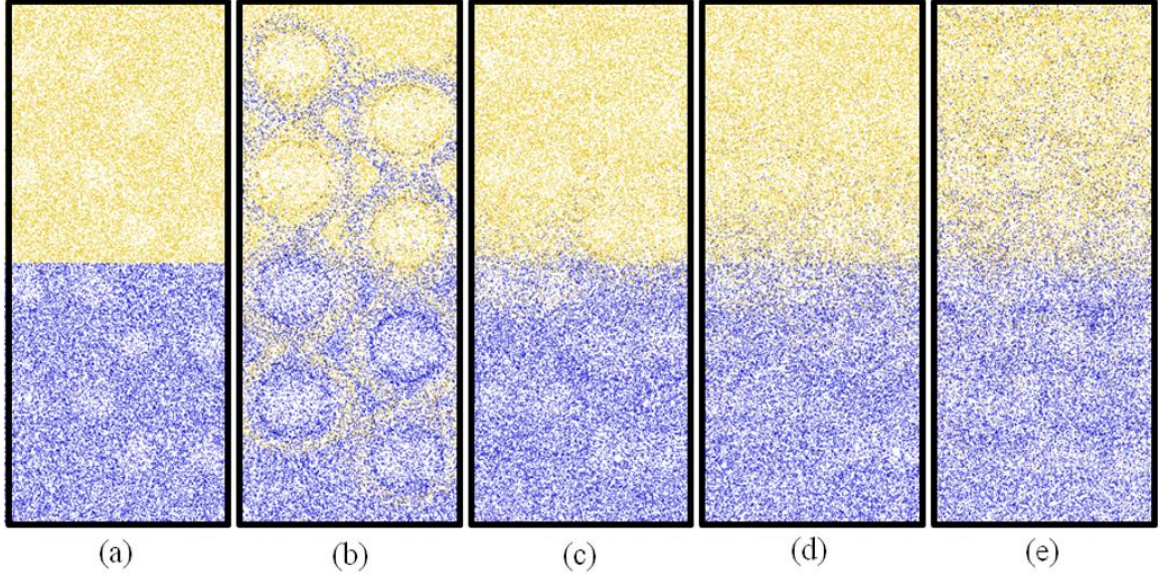


Figure 4.7 Horizontal view of the distribution of non-diffusive tracer particles from the entire height of the microchannel. a) Initial locations of tracer particles. b – e) Locations of tracer particles after 75 orbits of the magnetic microbeads in the channel at the following velocity ratios: b) $U_x/V_b = 0$, c) $U_x/V_b = 0.3$, d) $U_x/V_b = 0.6$, and e) $U_x/V_b = 1.4$

As in the diffusive case, interface stretching with non-diffusive particles declines sharply with increasing velocity ratio. At $U_x/V_b \approx 0.3$, the beads have minimal effect on cross-channel fluid transport and the streams of tracer particles remain essentially separated. However, at an increased velocity ratio, the tracer particles appear to be randomly dispersed across the channel, and this dispersion is increased with increasing velocity ratio. The fact that this dispersion is seen even in the case of non-diffusive particles suggests that this dispersion is a consequence of the flow in the channel with orbiting beads.

Thus, we find that mixing enhancement by orbiting magnetic microbeads occurs due to two different physical mechanisms: interface stretching due to bulk advection of fluid and particles in circular patterns stretching across the channel at relatively low velocity ratio flows, and dispersion of fluid and particles across the channel at higher velocity ratio flows.

The causes of these mixing enhancement mechanisms are investigated below.

The cause of bulk advection of fluid and particles across the channel in circular patterns and its dependence on the velocity ratio are elucidated by examining the streamlines of the period-averaged velocity field generated by orbiting magnetic beads, as shown in Figure 4.2 and discussed in section 4.1. With no net flow down the channel, circulatory flow cells are created, and are connected by streamlines which cross the microchannel. This serves to advect fluid and particles across the channel en masse in circulatory patterns. As a net flow velocity is introduced and the velocity ratio increases, fluid left in the wake of orbiting beads is advected downstream out of the trajectory of the oncoming bead, which leads the circulatory cells to shrink and streamlines linking cells across the channel to disappear (Figures 4.2b-d). Thus, the mechanism of bulk advection across the channel is suppressed for higher velocity ratios.

Dispersion of small amounts of fluid occurs due to interactions between the fluid streams created by adjacent rows of beads. At velocity ratios high enough that fluid is carried downstream quickly enough that it is not advected en masse across the channel in a single row of beads, the timing of fluid reaching adjacent rows of beads becomes important. For dispersion to occur, some of the fluid that is dragged by the orbiting beads should escape the orbit at a point in its trajectory where the fluid is displaced horizontally across the channel. The amount of dispersion depends on the amount of fluid being carried further across the channel. Thus, for optimal dispersion this displaced fluid should travel to the adjacent row of beads at the suitable speed such that it reaches the adjacent bead as it is travelling in that same direction, so that the fluid will be displaced further across the channel.

In the case of the geometry where $S = 2a$ and $D_d = a$, the distance between a bead and the corresponding bead on the adjacent row is $3a$, while the distance a bead must travel to orbit half way around a disc (since there are two beads per disc) is also approximately $3a$, as depicted in Figure 4.8a. Thus, if the fluid flows down the channel at the same speed as the beads orbit ($U_x/V_b = 1$), then the fluid will travel one bead row downstream ($3a$) for each bead half orbit. For some fluid to escape from an orbiting bead and continue downstream to be further displaced across the channel by the adjacent row of beads, rather than being dragged back so as to not travel further across the channel, it must travel fast enough to get past the next orbiting bead ($1.5a$) in the time it takes the beads to travel the distance of a half orbit ($3a$), as depicted in Figure 4.8b. This corresponds to $1.5a/3a \approx U_x/V_b \approx 0.5$, where an increase in mixing enhancement was observed, as seen in Figure 4.5a.

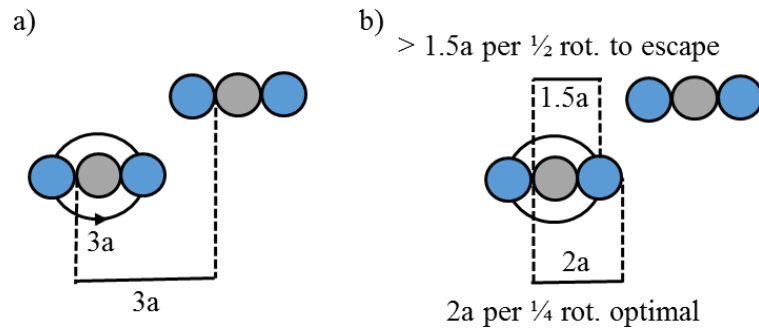


Figure 4.8 Schematic of the effect of geometry and velocities on mixing performance. a) Schematic of the geometry of two NiFe discs (grey circles) with $S = 2a$ and $\theta = 26.6^\circ$, with their associated beads (blue circles). Beads travel approximately a distance of $3a$ during a half orbit around a NiFe disc. Fluid travels a distance of $3a$ to get from one row of beads to the next. b) Schematic showing the critical distances for escape of fluid from a bead orbit (fluid must travel at least $1.5a$ during one half orbit to get past the center of the bead as it returns) and for optimal mixing (fluid travels $2a$ during one quarter orbit so as to be in front of bead on next row)

As depicted in Figure 4.8b, for optimal dispersion in the case of $\theta = 26.6^\circ$ the fluid should travel a distance of about $2a$ in the time it takes the beads to travel the distance of a quarter orbit ($1.5a$), so that the displaced fluid arrives at the adjacent bead as it begins to travel further across the channel, leading to the fluid being dragged further across the channel. This corresponds to $2a/1.5a \approx U_x/V_b \approx 1.33$, close to the local maximum in mixing enhancement at $U_x/V_b \approx 1.4$ for this geometry.

For differently spaced and angled mixing arrays, the optimal speed that the fluid must travel to properly reach the adjacent bead varies, leading to a geometry-dependent optimal velocity ratio as shown in Figure 4.5a-b. Since with increased spacing, beads have to move further to get to the next row of beads in a given orbit time, one would expect the optimal velocity ratio to increase approximately linearly with S . As seen in Figure 4.9a, simulations showed that this is in fact the case. The effect of offset angle on the optimal velocity ratio is less straightforward. As θ is increased, the distance that a bead on a subsequent row should move before sweeping past fluid moving downstream from a previous row of beads is increased. Thus, the fluid will have more time to get from one row of beads to the next, and the optimal velocity ratio will be reduced. As seen in Figure 4.9b, the optimal velocity ratio does indeed decrease with increasing θ .

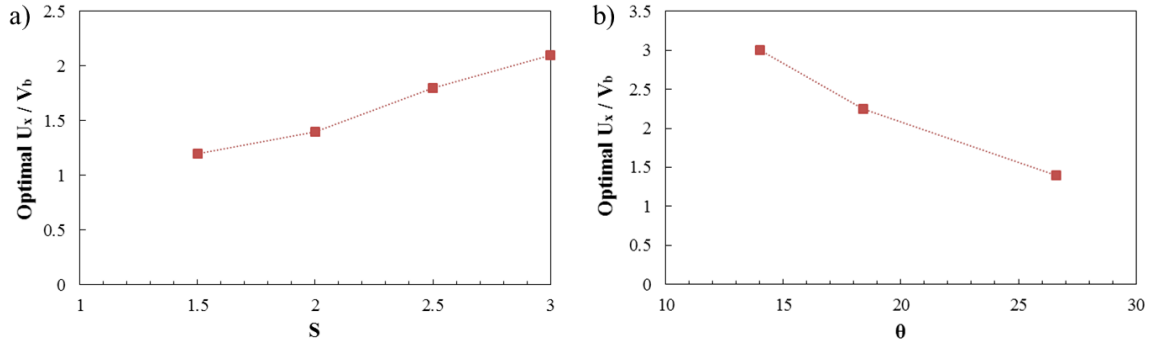


Figure 4.9 a) Effect of S on optimal velocity ratio for mixing enhancement. b) Effect of θ on optimal velocity ratio for mixing enhancement

4.2.3 Mixing Distance

In continuous-flow microfluidic mixing applications, it is important to obtain a high degree of mixing over a short downstream distance. Thus, the mixing performance of a micromixer can be evaluated based on how far the fluid must travel to reach a desired mixing degree. In order to efficiently simulate microfluidic mixing, for simulations in this study a small periodic domain (two rows of NiFe discs) in the flow direction is used, and travel distance downstream is represented by simulated time using the scaling argument $\Delta x = U_x t$, where Δx is the travel distance downstream, U_x is the average axial fluid velocity, and t is the simulation time, or the residence time of the fluid in the mixing region. In order to verify the accuracy of this approximation, mixing data were obtained for mixing in pressure-driven flows through microchannels with orbiting microbeads using this approximation and using a domain consisting of 20 rows of beads in the flow direction with separation of the fluid streams enforced at the inlet, such that the downstream distance could be measured directly. As seen in Figure 4.10a, the downstream evolution of the degree of mixing was almost identical at various velocity ratios using either method. Thus,

the small periodic domain can be safely used to evaluate downstream mixing distance for better computational efficiency.

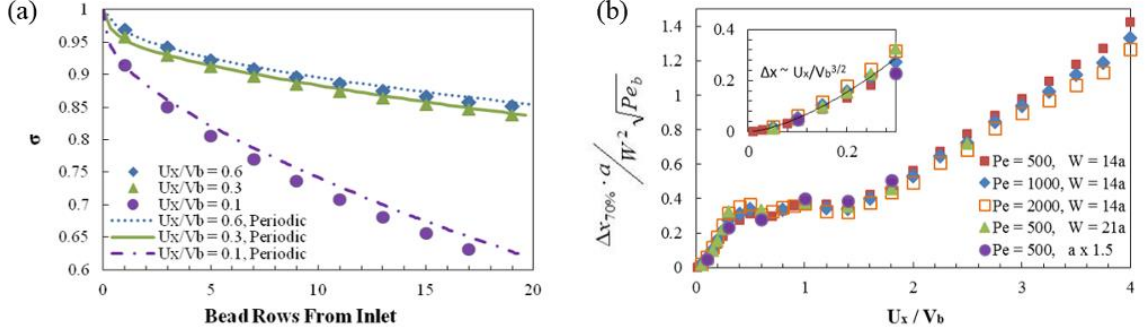


Figure 4.10 a) Mixing degree versus distance downstream from the inlet to the mixing section for various velocity ratios for the case of simulation of 20 rows of discs in the device (markers) and of simulation of a periodic domain that is two disc rows long, using time to estimate distance downstream (lines). b) Normalized distance downstream until the fluid reaches a level of 70% mixing under various conditions plotted against the velocity ratio. Inset shows a power-law increase in mixing distance (trend line in black) for low velocity ratios

One of the aims of this study is to gain an understanding of the expected mixing distances when system parameters are varied. This can be accomplished through non-dimensionalization of the mixing distance by pertinent physical parameters and varying those parameters in simulations. As was established above, $\Delta x = U_x t$ is a good approximation of the downstream travel distance. Additionally, for each velocity ratio U_x/V_b , the relation $U_x \propto V_b$ holds. Using a scaling argument, the residence time that the fluid is in the mixing section can be approximated by $t \propto W^2 / \overline{D}_\perp^*$. Here, $\overline{D}_\perp^* \propto D_0 \sqrt{Pe_b}$ is the transverse Taylor dispersivity (83) for transport in concentrated suspensions of rotating cylinders in which convective mass transport dominates diffusive mass transport ($Pe_b \gg 1$, in our case). Combining these relations, the downstream travel distance can be represented as

$$\Delta x \propto V_b \frac{W^2}{D_0 \sqrt{Pe_b}} \propto \frac{W^2}{a \sqrt{Pe_b}} \frac{V_b a}{D_0} \propto \frac{W^2}{a} \frac{Pe_b}{\sqrt{Pe_b}} \propto \frac{W^2 \sqrt{Pe_b}}{a}. \quad (4.2)$$

Thus W , Pe_b and a are expected to affect the mixing distance and are varied in simulations by varying W , D_0 , V_b and a over a wide range of velocity ratios. Once again, the geometric parameters $H_c = 2a$ and $D_d = a$ are kept constant, and here the configuration with $\theta = 26.6^\circ$ and $S = 2a$ and two beads orbiting each disc is used. The distance $\Delta x_{70\%}$ required to reach 70% mixing, normalized by equation 4.2, is plotted against the velocity ratio in Figure 4.10b. With this normalization, the mixing distance for each of these cases collapsed onto a single curve over a wide range of velocity ratios, supporting our scaling argument and allowing for the prediction of the performance of this device when used in applications requiring various size scales, channel dimensions and working fluid solutions at different flow and rotation rates, provided that there is uniform bead coverage of the entire microfluidic mixing section, as was the case in our simulations.

As can be expected, the shortest mixing distance occurs at low velocity ratios, since in this regime the high bead velocity with respect to the flow velocity allows for the beads to orbit more times for a given downstream travel distance, thus transporting more fluid across the channel. Additionally, as shown earlier, the best mixing enhancement for a given residence time occurs at low velocity ratios, since here secondary flow transports fluid in bulk across the channel. As shown in the inset to Figure 4.10b, the mixing distance increases as $(U_x/V_b)^{3/2}$ within the low velocity ratio range. A linear increase in mixing distance could be attributed to the decreased residence time per channel length, but the

nonlinearly decreasing mixing enhancement with increasing velocity ratio at small velocity ratios, as shown in Figure 4.5a, leads to a power law increase in mixing distance.

The mixing distance curve flattens out such that the mixing distance is relatively constant over the range of approximately $0.5 < U_x/V_b < 1.4$, since as seen in Figure 4.5a the mixing enhancement increases over this range due to fluid dispersion, such that this increase balances the decrease in residence time with increased flow velocity. This result is useful for high throughput applications, where a higher flow velocity is desired, but the rotation velocity can be limited by the increased hydrodynamic forces on the beads at high velocities, which can exceed the magnetic forces and cause magnetic bead detachment from the discs (4). We have experimentally observed that beads are stably controlled by NiFe discs at flow velocities at least up to 12 mm/s. The maximum velocities at which this method can be used will depend on the NiFe disc geometry and on the external magnetic field used in a specific device, since those affect the magnetic forces experienced by the beads.

The independence of the mixing distance from the velocity ratio for $0.5 < U_x/V_b < 1.4$ indicates that the flow velocity can be increased in this velocity ratio range without requiring a higher bead rotation speed or compromising mixing performance. As seen in Figure 4.10b, the mixing distance increases approximately linearly with velocity ratio above about $U_x/V_b \approx 1.4$, since in this range the mixing enhancement decreases only gradually, leaving the linear relationship between velocity ratio and mixing distance for a constant residence time of fluid in the channel.

To compare these non-dimensional mixing distances to relevant physical dimensions, we consider an example of fluid streams with diffusivity $D_0 \approx 10^{-11} \text{ m}^2/\text{s}$ flowed at $50 \text{ } \mu\text{m}/\text{s}$ through a $150 \text{ } \mu\text{m}$ wide channel with $2.8 \text{ } \mu\text{m}$ diameter beads orbiting at 4500 RPM. In this scenario, 70% mixing would be expected at a distance on the order of a millimeter. If the same conditions are used but the flow velocity is increased to the range of approximately $0.5 < U_x < 1.4 \text{ mm}/\text{s}$, then 70% mixing is still expected at a distance on the order of a centimeter. Thus, we conclude that this device provides most rapid mixing at low velocity ratios, but that if it is used at higher velocity ratios, it should be used at $U_x/V_b \approx 1.4$, so as to increase throughput while maintaining good mixing performance. If further increases in throughput are desired, then a , S , and H could all be increased so as to increase the channel cross section and also accelerate mixing for a given channel width. A drawback to increasing these dimensions is that it can be detrimental to micro-particle capture as will be seen in section 4.3.3, in that the particle size is effectively reduced as compared to the system size.

4.3 Micro-Particle Capture

4.3.1 Comparison to Experiments

We now turn to our discussion of the use of orbiting magnetic microbeads to capture micro-particles from a fluid sample. We compare the results using our model to those obtained experimentally by Owen (69) in a $400 \text{ } \mu\text{m}$ -long microfluidic capture region. Here, beads of diameter $a = 2.8 \text{ } \mu\text{m}$ orbit around discs of diameter $D_d = 6 \text{ } \mu\text{m}$ with spacing $s = 10 \text{ } \mu\text{m}$ in a microchannel of width W . In order to determine the ability of the system to capture

spherical particles in microchannels of varying height, capture experiments and simulations were performed in microchannels of height $H_c = 2a$, $3a$, and $4a$.

As seen in Figure 4.11, our simulations predict efficient particle capture. Our model predicts that in the shortest microchannel studied, with height $H = 2a$, almost 100% of the particles will be captured within the capture region for velocity ratios ranging from $0.05 < U_x/V_b < 0.5$. When the channel height is increased, capture drops off with increasing velocity ratio, such that for both $H_c = 3a$ and $H_c = 4a$ capture is reduced to approximately 65% for $U_x/V_b = 0.5$. Interestingly, for a channel of this short length, there was not a significant difference in capture efficiency for channels of height $H_c = 3a$ as compared to those with height $H_c = 4a$. As will be shown below, in longer channels this height difference plays a stronger role in capture efficiency.

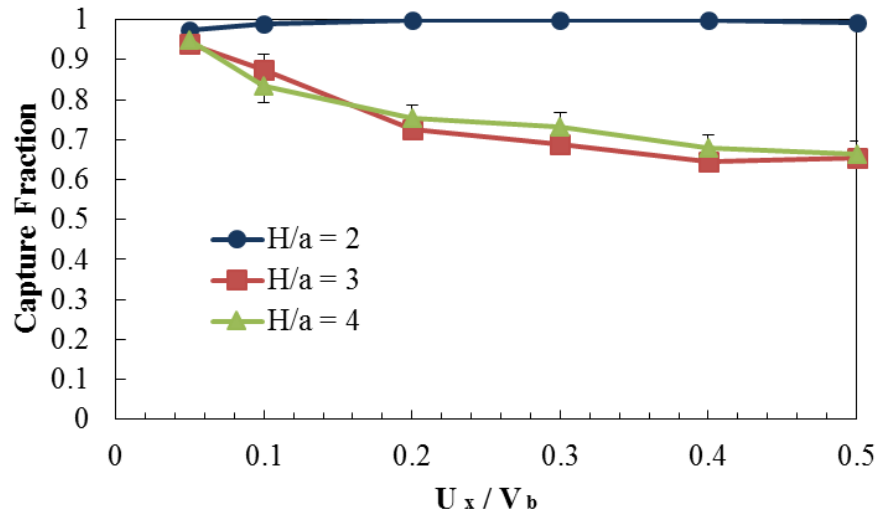


Figure 4.11 Simulation results for the fraction of micro-particles flowed over a range of velocity ratios through a capture section of microchannels of varied height which are captured by orbiting magnetic microbeads. Here, it is assumed that all particles that come into contact with beads are captured

Efficient particle capture occurs due to the fact that fluid at the height of the beads winds between oncoming beads, coming into close contact with magnetic beads as described in section 4.1. Particles are driven by the fluid, and thus particles at the height of the beads also come into close contact with magnetic beads, leading to rapid capture. Further, vertical flow due to the beads, as shown in Figure 4.1c, serves to draw particles down toward the beads for capture. Thus, microchannels with a height close to the diameter of the beads are best suited to efficient particle capture, but orbiting beads are able to draw downward and capture particles from channels even with somewhat increased height.

As described in section 3.1.3, our model operates under the assumption that all particles that come into contact with beads are instantly captured. However, in a physical system the binding kinetics of the specific system of interest depend on factors such as the types of target biological or synthetic particles, the antibodies used for specific binding, and the pH of the system, and can prevent permanent capture of some particles that come into contact with the beads. Indeed, Owen (69) observed that although there was a similar trend in capture with increasing velocity ratio, the actual capture values were significantly reduced from the simulation results shown in Figure 4.11.

As seen in the blue hollow circles in Figure 4.12, particle capture experiments in channels of height $H_c = 2a$ yielded particle capture as high as 90% at a velocity ratio of $U_x/V_b = 0.1$. The capture fraction decreased down to close to 50% at $U_x/V_b = 0.5$, due to the decreased effect of the moving beads on capture. In taller microchannels, the decrease in capture efficiency with increasing velocity ratio was even more dramatic. As seen from the hollow red squares and green triangles in Figure 4.12, experiments showed capture efficiencies as

high as 80% for low velocity ratios in the range of $U_x/V_b = 0.05$, decreasing to approximately 10% at $U_x/V_b = 0.3$. This dramatic decrease in capture efficiency with increasing velocity ratios in taller channels is due to the fact that in addition to changes to the flow due to the decreased effect of magnetic beads, the residence time of the particles in the channel is decreased with increasing flow rate, giving them less time to be drawn down to the beads as they pass through the channel.

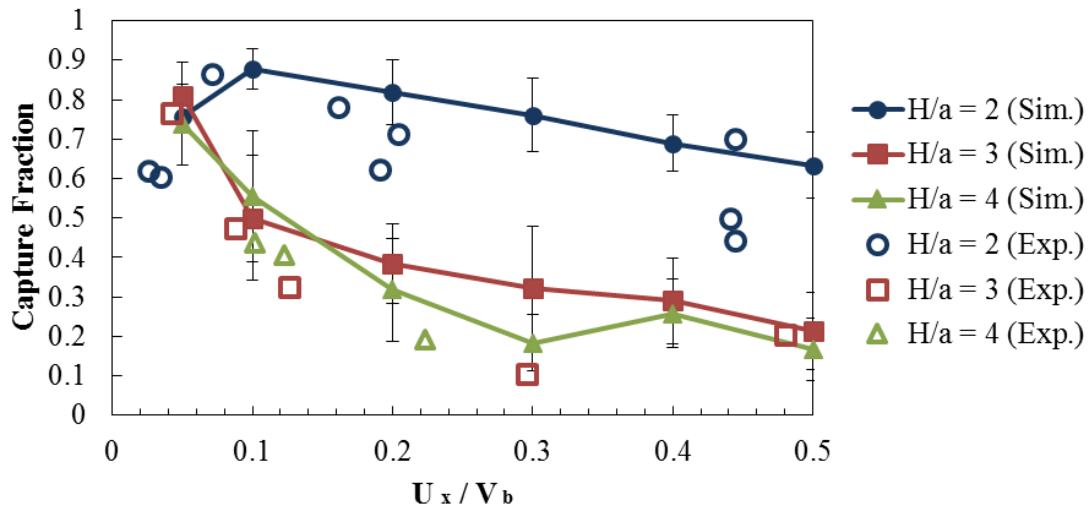


Figure 4.12 Capture fraction of particles in channels of varying height subjected to flows at different velocity ratios. Here, particles are not assumed to be captured irreversibly on contact. Hollow markers denote capture fractions obtained in the experiments of Owen (69). Lines with solid markers represent predicted particle capture under the same conditions, assuming that particles have a 20% probability of irreversible capture on contact with beads

In order to compare results of simulations and experiments, we performed analysis on our simulation results such that only 20% of particles that come into contact with a magnetic bead were determined to be captured. If a particle contacts a bead but is determined by comparison of a random number generated from a uniform distribution to the capture probability of 0.2 to not be captured, then the distance that it traveled

downstream is stored and added to the downstream travel distance of the next contacted particle. This is repeated until a particle is deemed to have been captured. As seen by the lines with solid markers in Figure 4.12, when only 20% of contacted particles are deemed to have been irreversibly captured, the computationally predicted capture fractions are similar to the experimental results described in the preceding paragraph, validating the ability of our model to decipher the experimental trends in capture performance.

In addition to the generally decreasing capture fraction with increasing velocity ratio, it is interesting to note that for capture in channels of height $H_c = 2a$ the capture fraction is decreased at about $U_x/V_b = 0.05$ as compared to that achieved at $U_x/V_b = 0.1$. This was observed in both the experimental and computational capture data. This is related to the fact that as seen in Figure 4.2a, at low velocity ratios fluid in the channel on average moves in circulatory patterns around NiFe discs, enabling particles to follow the beads in their orbits, thus avoiding direct contact. However, for larger velocity ratios (Figure 4.2b-d) these flow cells are reduced, leaving the beads to flow down the channel weaving between oncoming beads as described previously, increasing the probability of contact between particles and beads.

Since the probability of capture is highly dependent on the binding kinetics in the specific capture system, the remainder of our study will focus on capture using the assumption that particles are captured irreversibly on contact. This serves to give an upper limit on capture performance so as to understand how to design efficient capture devices, independent of further improvements that can be made in the binding kinetics of the system.

4.3.2 Distance to Particle Contact

In the remainder of this chapter, we use simulations to determine the length of continuous-flow device required to capture a desired percentage of particles from a fluid sample, and to study the effect of various system parameters on the capture distance. This allows us to guide the design of compact and efficient devices capable of a high probability of particle capture.

In order to understand the effect of NiFe disc spacing on capture of spherical particles, we collected computational capture data using capture regions patterned with varied NiFe edge to edge disc spacing S in channels with height $H_c = 2a$ over a range of velocity ratios. We varied S so as to correspond to a range from 8 μm to 14 μm . As seen in Figure 4.13, devices with all studied values of S followed a general trend of increasing distance required for particle capture with increasing velocity ratio, except in the case of very low velocity ratio, where capture performance is diminished as explained previously. Note that for all of these configurations, capture of 95% of the particles is achieved within a compact capture region of approximately 10-40 rows of beads (based on a spacing of $S = 10\mu\text{m}$), corresponding to a distance of 200-600 μm . Additionally, the increase in capture distance with increased velocity ratio is dependent on S . While all three configurations yielded approximately the same capture performance at low velocity ratios, capture arrays with greater spacing required a significantly greater capture distance at increased velocity ratio. This is due to the fact that this increased spacing gives more space for particles to pass by the beads without contact when they are traveling down the channel in the moderate to high velocity ratio regime described previously. Thus, devices with tight

spacing are recommended for increasing capture performance so as to capture particles over a minimal capture distance. However, one must consider the fact that if a device is designed with extremely tight spacing, the magnetic beads and their captured particles can collide with each other. Owen (69) found experimentally that in arrays with $S = 8\mu m$, beads were prone to collide with particles attached to neighboring orbiting microbeads, resulting in the formation of clumps of beads and particles. In order to maximize capture efficiency while avoiding geometries that would lead to clumping, we perform the rest of our study using $S = 10\mu m$.

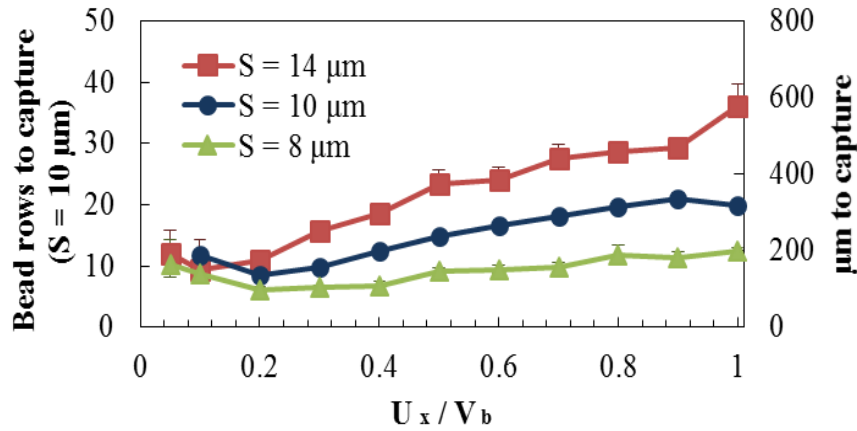


Figure 4.13 Distance required for capture of 95% of spherical particles in a microchannel of height $H_c = 2a$ with NiFe disc spacing $S = 14\mu m$, $10\mu m$, and $8\mu m$ over a range of velocity ratios

In order to study the effect of the microchannel height, H_c , on capture distance, we performed simulations to collect data on the distance required to capture spherical particles in capture arrays with constant $S = 10\mu m$ under flow conditions at $U_x/V_b = 0.5$. As seen in Figure 4.14, we found that the distance to capture increases exponentially with channel height, although capture of 95% of the particles is still possible in channels up to six times

taller than the bead diameter. Above this height, the beads did not sufficiently affect all of the fluid in the channel so as to draw particles from all regions of the channel down to the beads for capture.

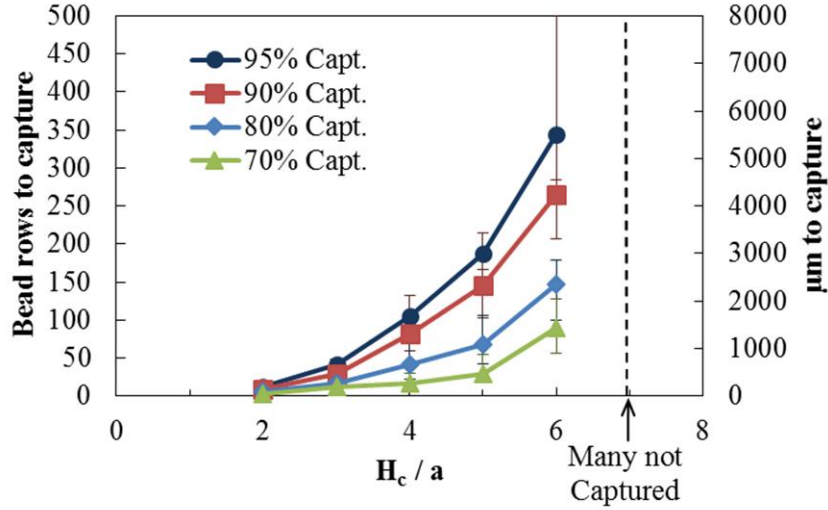


Figure 4.14 Distance to capture of 95%, 90%, 80% and 70% of spherical particles subjected to flow at $U_x/V_b = 0.5$ by beads in a capture region with $S = 10\mu m$. The channel height, H_c , is varied so as to determine the effect of channel height on capture distance

The dependence of capture distance on channel height is linked to the requirement of particles to move downward to the array of beads in order to be captured. As the channel height is increased, an increasing proportion of particles is located at a height away from the beads, and they must be drawn down over greater distances to the beads by fluid flow which weakens with increasing distance from the beads. Thus we confirm the dependence of capture performance on channel height as seen in Figures 4.11 and 4.12, and further find that this has an especially strong effect on capture distance as compared to the capture fraction after a short distance. This is because in the case of determining a capture distance,

a large percentage of the particles must be captured, requiring particles to be captured from the entire height of the channel.

4.3.3 *Capture of Non-Spherical Particles*

Up to this point, our study has focused on capture of spherical particles. While many particles of interest for detection come in nearly spherical shapes, we also desire the capability of capturing particles of other shapes. For example, bacteria often come in the shape of rods, as is the case with salmonella. In order to understand the effect of particle shape on capture performance, we performed simulations on the capture of rod-shaped particles, such as those shown in Figure 3.3 and described in section 3.1.3. We calculated the distance required to capture 80% and 95% of rod-shaped particles in a device with $S = 10\mu m$ and $H_c = 2a$ over a range of velocity ratios, and compared it to capture data on spherical particles under the same conditions. As seen by the green and light blue curves in Figure 4.15, we found no appreciable difference between the distance required to capture 80% of rod-shaped particles and the distance required to capture 80% of spherical particles. By contrast, we observed that changing the diameter of spherical particles has a substantial effect on capture performance, with larger particles being captured more rapidly than smaller ones. We observed that rod-shaped particles do not move in a simple tumbling motion in the flow generated by orbiting beads, which explains why they are not captured as effectively as spheres of diameter equal to the rod length. While we found little effect of particle shape on capture distance for 80% capture, it required a significantly increased distance to capture 95% of rod-shaped particles from the microchannel than it did to capture the same percentage of spherical particles.

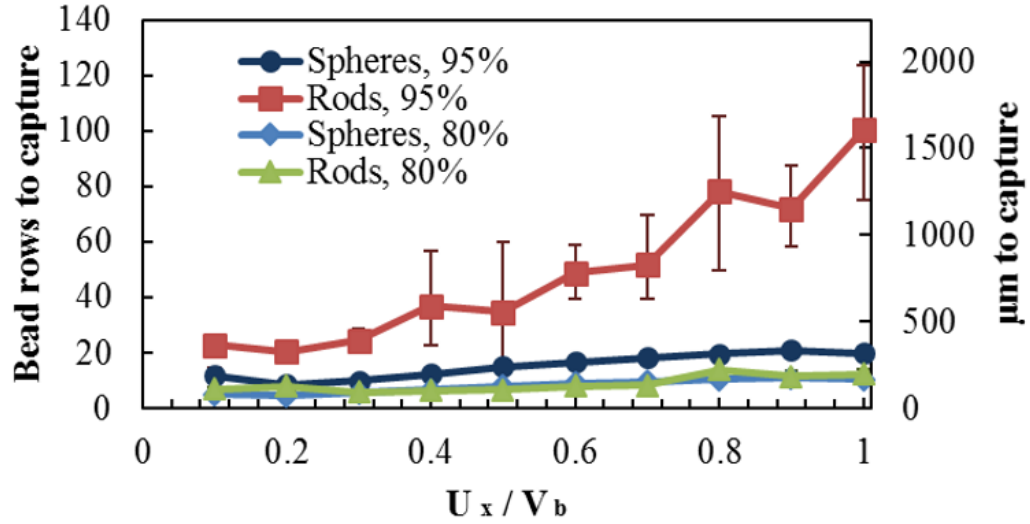


Figure 4.15 Distance required to capture 80% and 95% percent of spherical and rod-shaped particles in a microfluidic channel with $S = 10\mu m$ and $H_c = 2a$ over a range of velocity ratios

Closer examination of particle trajectories revealed that while spherical particles weaved down the channel as they passed rows of microbeads, they did not generally migrate across the channel. However, rod-shaped particles were observed to migrate laterally across the channel as they weaved past rows of microbeads. This resulted in a minority of the rod-shaped particles migrating to the sides of the microchannel, allowing them to flow past small gaps at the edges of the capture array, where magnetic microbeads are unable to orbit without running into the walls. Thus, while the effectiveness of our system at contacting the majority of particles is not strongly dependent on particle shape, lateral migration of rod-shaped particles can affect capture of a minority of the particles. If a high probability of capture of rod-shaped particles is required, then steps should be taken to ensure that particles cannot pass through the microchannel at the channel sides, allowing them to escape undetected. Additionally, particle shape could affect binding of particles to the

magnetic beads, since it can affect the available surface area of the particle for binding, as well as fluid shear forces which can separate particles from the beads.

4.4 Summary

A microfluidic device that utilizes magnetic microbeads orbiting around NiFe discs patterned on a microchannel floor to provide for microfluidic mixing and micro-particle capture was investigated computationally and validated by comparison with experiments. Three-dimensional numerical simulations were developed to model the dynamics of the system, and showed close agreement with the experiments, thereby validating our computational models.

We showed that orbiting microbeads can lead to rapid fluid mixing in low Reynolds number flow, and identified two distinct mixing mechanisms. Bulk advection of fluid across the channel occurs due to the flow pattern that is developed when the ratio of flow velocity to bead velocity is low, and leads to rapid mixing. At higher velocity ratios, dispersion of small amounts of fluid across the channel occurs, and results in increased mixing. We used simulations to investigate the effect of system parameters on mixing performance, so as to guide the effective design of such microfluidic devices for microfluidic mixing applications.

Further, we investigated the ability of orbiting magnetic microbeads to capture particles from fluid samples. We found that orbiting beads are effective at promoting contact between beads and target particles, allowing for efficient particle capture in short distances. Flow patterns created by beads assist them in drawing particles down to the height of the beads, enabling capture from channels up to six times as tall as the beads. We investigated

the effect of system parameters on the distance required for sufficient particle capture, enabling an understanding of how to best use the device for efficient micro-particle capture.

Magnetic beads dissipate little energy through viscous drag (on the order of picowatts to femtowatts), such that their power consumption is low even compared to the power required to drive flow through a microfluidic channel even without the use of a passive mixer (on the order of nanowatts to picowatts). The majority of power dissipation in such a system is expected to be due to inefficiencies in motors driving the rotating magnet and the syringe pump (on the order of one watt).

The major limitation to the use of orbiting magnetic microbeads is that it requires microchannels of limited height, since the beads must be able to affect fluid from the entire height of the channel, yet the beads are constrained to 2-D motion on the microchannel floor. This presents a limitation in the throughput of such a device. In order to overcome this limitation, if high volume throughput is required then either multiple microchannels should be used in parallel or orbiting microbeads should be combined with another method of large-scale circulation generation (such as that presented in chapter 5) to bring more fluid to the beads for processing.

The use of orbiting magnetic microbeads enables mixing of complex fluid samples without blocking particulates such as cells from passing through the microchannel. Additionally, microbeads can be functionalized and used to capture particles such as live cells from fluid samples, and can then be readily extracted from the device using a magnetic field for further analysis. Thus, orbiting magnetic microbeads can provide for multiple functionalities in a single device.

CHAPTER 5. MICROFLUIDIC MIXING AND PARTICLE CAPTURE USING MAGNETICALLY ACTUATED SYNTHETIC CILIA

Cilia are flexible, high aspect ratio structures that are used by a variety of biological organisms for transport of fluid and particles at a low Reynolds number (5, 6). As mentioned in section 3.2.1, the bending patterns of cilia are defined in large part using the non-dimensional sperm number Sp . Cilia are of interest for microfluidic applications, as when used with a moderate value of Sp on the order of one, they bend in patterns that are time-irreversible, thereby enabling transport in the low Reynolds number microfluidic environment. When used at too low or too high Sp , they move either in a nearly time-reversible manner or with minimal deflection, respectively, and are not particularly useful in microfluidic applications. Ghosh et al (70) showed that cilia oscillating at $Sp \approx 3$ and $Sp \approx 5$ exhibit interesting bending patterns, which correspond to the first two oscillatory modes of a beating flagellum (8), with cilia oscillating at $Sp \approx 3$ displacing an order of magnitude further than those at $Sp \approx 5$ for the same driving force. These two bending patterns exhibit travelling waves, which transport fluid along the cilia (8, 82). We use these findings to guide the design of magnetically actuated synthetic cilia, so as to create flow patterns enabling a large-scale flow transport in a microchannel.

We simulate two distinct types of magnetically actuated synthetic cilia to understand their dynamics and their utility in microfluidic applications such as mixing and particle

capture. We first discuss our findings on dynamics of high aspect ratio flexible filaments, and then turn to discussion of ribbon-shaped cilia.

5.1 Filament Cilia

We use computational modeling to probe the utility of actuated synthetic cilia lining walls of a microfluidic channel for enhancing microfluidic mixing and capture of nano-particles dispersed in a viscous fluid filling the channel, as shown in Figure 3.5. We demonstrate that elastic cilia actuated by a sinusoidal force generate circulatory secondary flows facilitating transport. We investigate the effect of operational conditions on cilia transport. Our findings guide the optimal design of ciliated microfluidic systems for uses such as deposition of particulates onto sensory surfaces and microfluidic mixing.

5.1.1 Cilia Dynamics and Flow Generation

We start by examining the dynamics of the flexible filament cilium. In order to understand the effect of Sp and A , as defined in section 3.2.1, on cilia dynamics, we performed numerical simulations of high aspect ratio cilia of square cross-section in a viscous fluid. Here, we applied a sinusoidal oscillating horizontal force to the cilia tips, and varied the frequency and amplitude of this actuation force. While we present results for cilia actuated at the tip, we have found that most of the behavior exhibited by cilia oscillated at their tips is also seen in cilia oscillated by a distributed force applied along the cilium length.

In our simulations, we observed that cilia exhibit bending patterns at $A=1$ similar to those reported by Ghosh et al (70). We focus our study on the effect of Sp on fluid flow. Figure 5.1 shows the period-averaged flow fields for various Sp . The flow fields are

calculated using the period-averaged velocity of non-diffusive tracer particles. Due to symmetry, a slice $x-y$ plane at the center of the cilia in the z - direction is given only for the bottom half of the channel from the middle plane between cilia in the x - direction and the left side of the cilia (Figure 5.1).

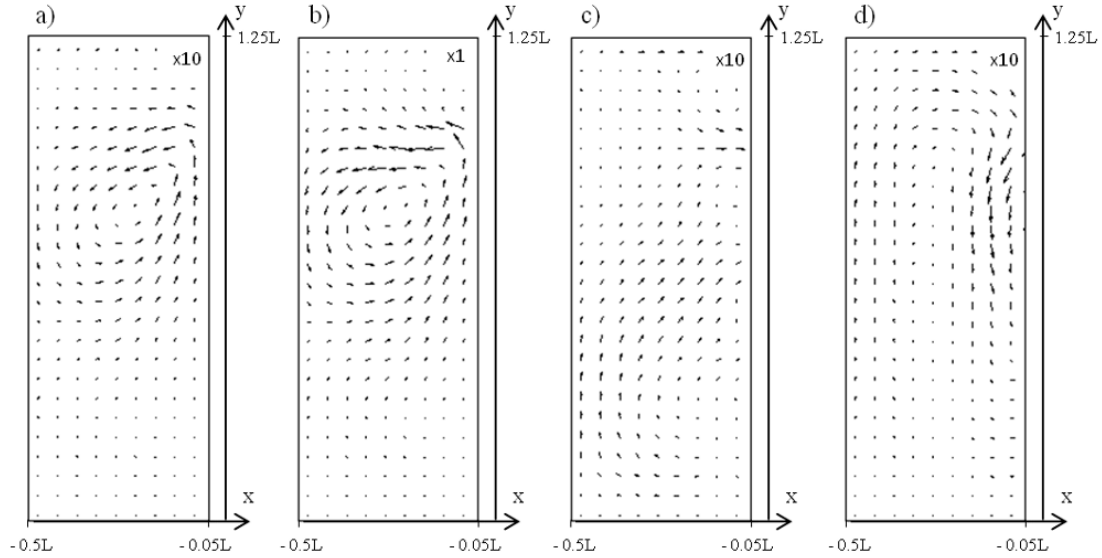


Figure 5.1 Period-averaged velocity in the $x-y$ (cilia motion) plane (see Figure 3.5a) with $A=1$, $\delta x/L=1$, and a) $Sp=2$, b) $Sp=3$, c) $Sp=4$, d) $Sp=5$. For clarity, velocity magnitudes for $Sp=2$, 4, and 5 are scaled up by a factor of ten as compared to those for $Sp=3$. $Sp=3$ results in the most significant circulatory flow patterns

In all cases presented in Figure 5.1, oscillating cilia induce secondary flows in the microchannel. However, among all these cases $Sp=3$ induces the fastest secondary flow with the velocity about an order of magnitude greater than for the other cases. We also find that the structure of flow is different for ciliated channels with $Sp=2$ and $Sp=3$ versus that with $Sp=4$ and $Sp=5$. When oscillated at $Sp=2$ and $Sp=3$, the cilia create a large circulating flow pattern (Figure 5.1a-b) that transports fluid upward near the cilia and downward in the center between neighboring cilia. On the other hand, when cilia

oscillations are characterized by $Sp=4$ and $Sp=5$, the period-averaged flow includes multiple smaller vortices that locally transport fluid, and fluid is generally transported upward in the center between neighboring cilia.

We investigated the effect of the magnitude of the cilia actuation force on cilia and fluid dynamics by setting $Sp=3$ and varying A . Cilia displacement and flow circulation patterns increase with increasing A up to $A=12$, above which cilia displacement is geometrically limited and further increases in A do not lead to significantly greater cilia displacement or flow circulation.

We also find that cilia can exhibit transition from a 2-D to 3-D beating pattern when the oscillating force amplitude exceeds a critical value A_{cr} (Figure 5.2). When driven by relatively small oscillatory forces, cilia beat in a periodic 2-D non-reciprocal pattern, as shown for $A=6$ in Figures 5.2a-b. However, when the driving force is increased to $A=8$, the beating cilia exhibit a periodic 3-D pattern, as shown for $A=8$ in Figures 5.2a-b. The 3-D motion of cilia with $A=8$ is further illustrated in Figures 5.2c-d, showing a sequence of projections of the cilium centerline on the $x-y$ and $x-z$ planes, respectively, during an oscillation period. Our simulations show that the critical amplitude of the oscillatory force causing the transition for $Sp=3$ is $A_{cr} \approx 7$.

The 3-D bending of cilia is caused by a buckling instability (84-86). Buckling occurs when the oscillating force $A > A_{cr}$ bends the cilia to the side, and then drives them in the opposite direction, as shown in Figure 5.2e. Buckling causes cilium bending in the $x-z$ plane, thereby inducing 3-D motion of the oscillating cilia. This behavior resembles Euler's

buckling instability of columns. We can estimate the critical force leading to cilium buckling by considering an axially-loaded long column with unsupported length of $0.75L$, which is approximately equal to the length of the horizontal section of cilia in our simulations at the onset of buckling. Replacing the oscillatory external force with a constant compressive force and using Euler's formula for the critical force for a column with fixed-free end conditions (87), we estimate the magnitude of the dimensionless force required to induce buckling to be approximately 1.5. This value is close to the instantaneous external force experienced by cilia at the onset of buckling, which is found in simulations to be approximately 4, indicating that the 3-D motion is indeed a result of cilium buckling during the beating cycle.

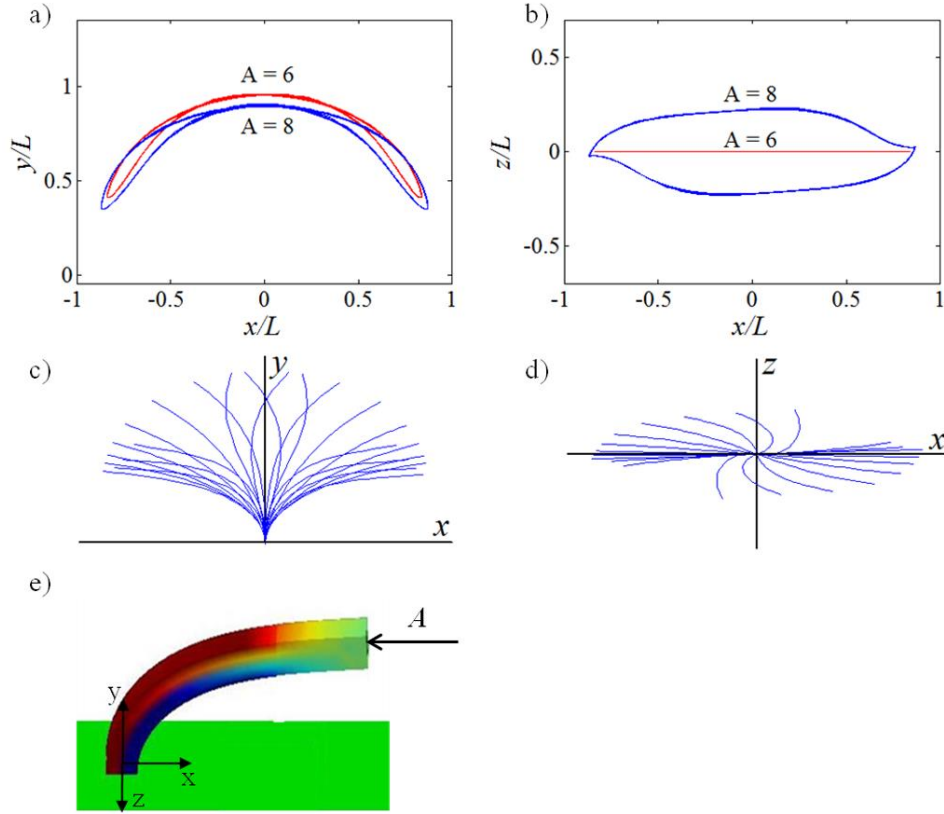


Figure 5.2 Cilium tip trajectory for $Sp = 3$ and $\delta x/L = 1$ a) in the $x - y$ plane, and b) in the $x - z$ plane. Cilium movement is two-dimensional when the driving force amplitude is $A = 6$, but becomes 3-D when the driving force amplitude is increased to $A = 8$. Panels c) and d) show centerlines of cilia with $A = 8$ at different instants of cilium beating in the $x - y$ and $x - z$ plane, respectively. e) 3-D motion is a result of cilia buckling, due to a compressive force applied to the cilium end when it is bent over horizontally

5.1.2 Asymmetric Cilia Actuation

Additional control over net flow at a low Reynolds number can be obtained by using asymmetric forcing applied to cilia. Biological cilia achieve this through the use of complex beating patterns (82, 88) which include an effective stroke and a recovery stroke in their beat cycles. We seek to demonstrate fluid manipulation using a simplified beating pattern with effective and recovery strokes, which pattern is created through magnetic actuation of cilia using a modulated sinusoidal oscillating magnetic force. Such cilia have

application not only in pumping fluid along a microchannel, but also in creating large-scale circulatory patterns across a microchannel, enabling effective and controllable microfluidic mixing and particle capture.

In order to probe the effect of modulating the oscillating magnetic force, we performed simulations in which we modulated the oscillating distributed force applied on an elastic filament cilium such that the amplitude and/or period of the section of the force waveform during the effective stroke was different from that applied during the recovery stroke. We found that both force modulations can cause cilia to beat in asymmetric patterns that cause fluid pumping. A representative example is the case where the forces applied during the effective and recovery strokes were not equal. To characterize the level of asymmetry of these forces, we define the force ratio $R_F = F_R/F_E$, where F_R is the magnitude of the force applied on the recovery stroke, and F_E is the magnitude of the force applied during the effective stroke. As a baseline, we simulated a cilium that is driven at $Sp = 3$ and $A = 45$ with $R_F = 1$, and found that the beating pattern is symmetric, as seen in Figure 5.3a-b. For the case of $R_F = 0.5$, we found that cilia beat in a highly asymmetric pattern similar to the patterns of biological cilia. In this pattern, as shown in Figure 5.3c-d, cilia are erect during their effective stroke, and are bent over during their recovery stroke. This type of stroke allows cilia to produce net pumping along a ciliated surface, as they push more fluid in their erect effective stroke than they pull back as they are bent over during their recovery stroke. To quantify their pumping effect, we define the pumping effectiveness, $\mathcal{E} = V_{pump,stroke}/L^3$, where $V_{pump,stroke}$ is the volume of fluid pumped for each stroke cycle.

We found that for the symmetric case where $R_F = 1$, the pumping effectiveness was $\varepsilon = 0$, while we calculated a high pumping effectiveness of $\varepsilon = 0.74$ for the case of $R_F = 0.5$.

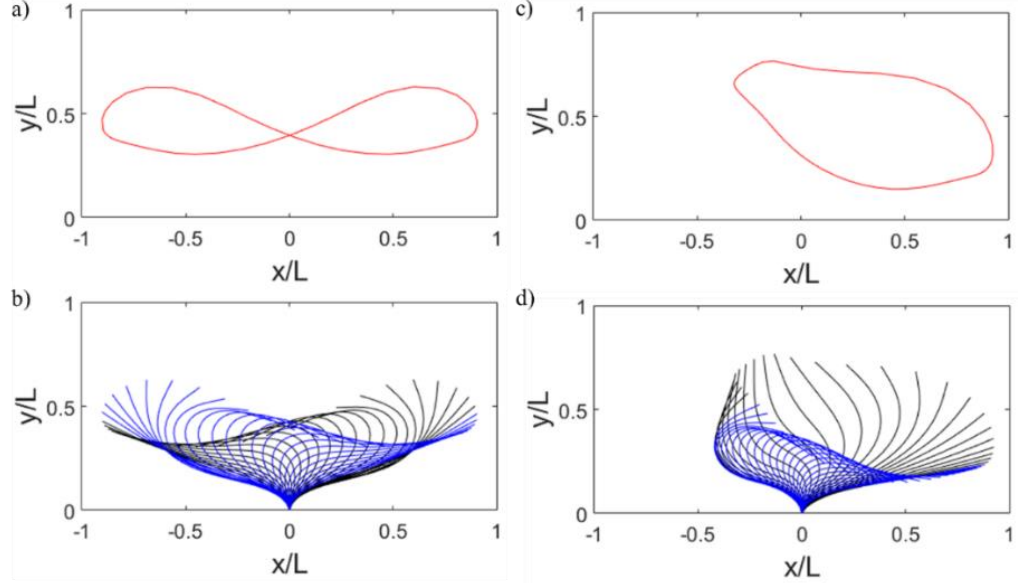


Figure 5.3 Trajectories of cilia modeled as flexible filaments driven by symmetric and asymmetric oscillatory distributed forces at $Sp = 3$ and $A = 45$. Red lines are the tip trajectories, black lines are snapshots of the cilium centerline during the effective stroke, and blue lines are snapshots of the cilium centerline during the recovery stroke. a) Trajectory of the cilium tip for the case of $R_F = 1$, b) Snapshots of the cilium for the case of $R_F = 1$, c) Trajectory of the cilium tip for the case of $R_F = 0.5$, d) Snapshots of the cilium for the case of $R_F = 0.5$

5.1.3 Nano-Particle Capture

Nano-particle capture can be a slow process if left entirely up to diffusion to bring particles to sensory surfaces. In order to evaluate the utility of magnetically actuated synthetic cilia for capture of nanoscale particles onto sensory surfaces, we performed simulations using the model of a channel with ciliated top and bottom walls, as described in section 3.2.1 and shown in Figure 3.5a-b. We characterized deposition enhancement due to oscillating cilia through comparison to deposition due purely to diffusion, as given by the analytical

solution of equation 3.12 and data for the analytical solution and simulations in non-ciliated channels as given in Figure 3.11, which showed that the fraction of nano-particles deposited on channel walls, P , increases steadily with time even without the use of cilia.

When we introduce elastic cilia that are driven by a horizontally oscillating force applied at the cilia tips, the deposition rate increases. Figure 5.4 shows a plot of P over time for both the case of oscillating cilia (solid line) and for the case with no cilia (dashed line). The amount of deposited particles increases more quickly when the fluid is agitated by oscillating cilia, indicating that beating cilia enhance nano-particle deposition by creating convective fluid flows.

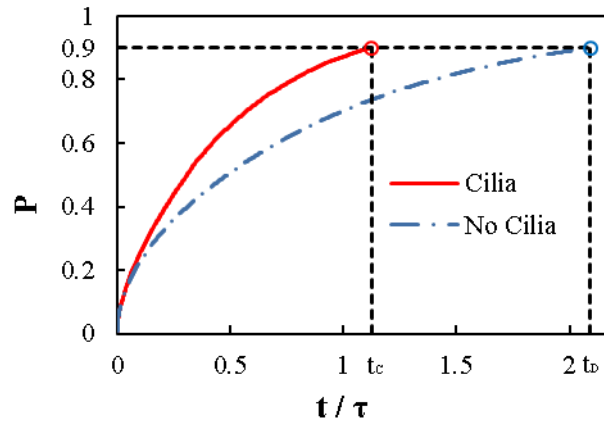


Figure 5.4 Deposition of nano-particles ($Sc = 4000$) on microchannel walls without cilia and with cilia beating at $Sp = 3$, $\delta x/L = 1$, and $A = 1$. The time required to achieve 90% deposition is shown for each case, and is denoted by t_D and t_C , respectively

In order to quantify the enhancement of deposition, we introduce a deposition enhancement factor $E_P = t_D/t_C$, where t_D is the time required to reach the desired deposition P without cilia, and t_C is the time required to reach the same P with oscillating cilia. For the case shown in Figure 5.4b, the deposition enhancement for 90%

deposition, denoted by $E_{0.9}$, was found to be 1.86. This means that 90% of particles will be deposited almost two times faster using oscillating cilia as compared to the deposition in a plain channel.

The value of E depends upon P , as shown in the plots of E versus P for varying Sp and A given in Figures 5.5a and 5.5b, respectively. For relatively short times $t \ll \tau$, deposition is limited to those nano-particles that are near the walls, in which case enhancement due to oscillating cilia is relatively weak. However, as the deposited P increases, E also increases. This can be explained by considering that the initial concentration of particles throughout the channel is uniform and particles located close to the walls can deposit quickly due to molecular diffusion. As more particles deposit on the channel walls, the concentration of particles near the walls is reduced as compared to the center of the channel. This causes the deposition rate to slow as P increases (Figure 5.5). If beating cilia are used to agitate the fluid, then the fluid from the center of the channel, which contains a higher concentration of particles, is brought closer to the walls, increasing the amount of particles that are near the walls, thereby facilitating their deposition. Thus, the influence of beating cilia on deposition increases with time as the concentration of particles in the channel drops.

We find that E increases monotonically for different values of Sp , as shown in Figure 5.5a. Among three values of Sp shown in this figure, $Sp = 3$ yields a consistently larger E than somewhat larger and smaller values of Sp indicating a non-trivial dependence of E on Sp . We also find that an increase in amplitude can enhance the

deposition as indicated by increasing E in Figure 5.5b. Below, we examine the dependence of E on Sp and A in more detail.

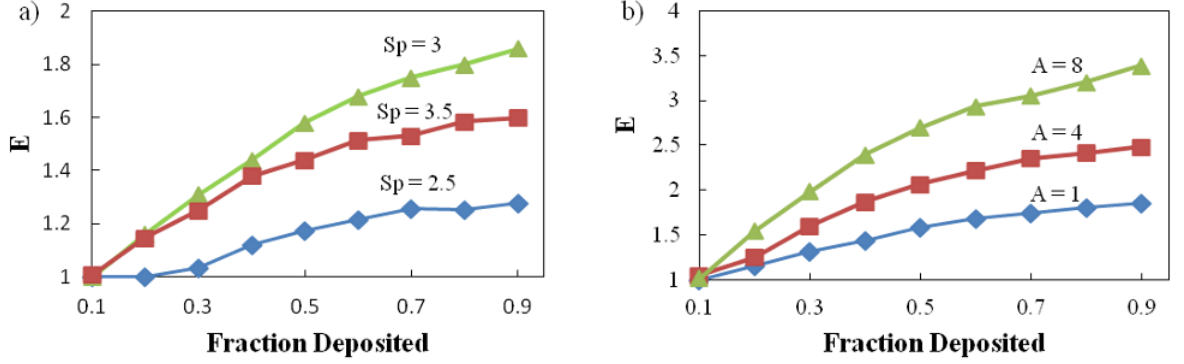


Figure 5.5 Deposition enhancement E in ciliated microchannels with $\delta x/L = 1$ for nanoparticles with $Sc = 4000$. a) Cilia beating with different Sp and $A = 1$. b) Cilia beating with different A and $Sp = 3$

We first investigate the effect of Sp on the deposition of nano-particles in a ciliated microchannel. As seen in Figure 5.6, the dependence of E on Sp is non-monotonic, with two maxima at around $Sp = 3$ and $Sp = 5$, respectively. The maximum at $Sp = 3$ is significantly larger than at $Sp = 5$ and, therefore, characterizes the beating regime that is optimal for enhancing nano-particle deposition. We find a similar dependence of E on Sp for different values of the Schmidt number Sc , as defined in section 3.2.4. Our simulations show that the enhancement is more significant for larger Sc . Because Sc relates the effects of fluid convection on mass transport to that of diffusion, an enhancement for larger Sc means that the effect of cilia on deposition will be more significant for larger, less diffusive particles, as well as for systems at lower temperatures, for which transport by diffusion is relatively slow.

The non-trivial relationship between E and Sp results from the flow patterns generated by cilia oscillating with different Sp , as discussed in section 5.1.1 and shown in Figure 5.1. In all cases presented in Figure 5.1, oscillating cilia induce secondary flows in the microchannel. However, among all these cases $Sp = 3$ induces the fastest secondary flow with the velocity about an order of magnitude greater than for the other cases. Additionally, cilia oscillating at $Sp = 3$ create large circulatory patterns. Thus, we find that cilia with $Sp = 3$ are optimal for enhancing nano-particle deposition.

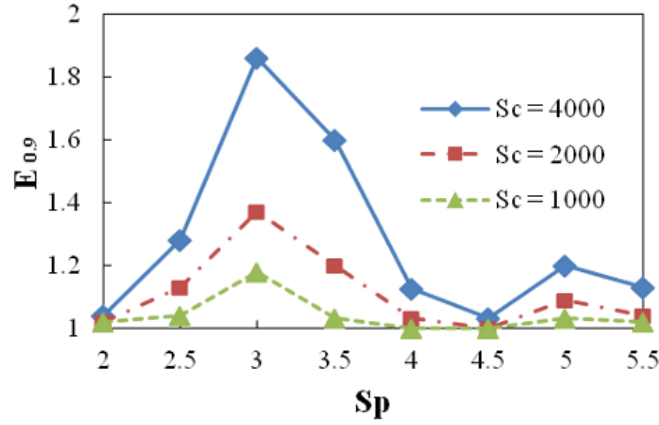


Figure 5.6 Dependence of E at 90% deposition on cilia sperm number Sp . The force amplitude is $A = 1$ and cilia separation is $\delta x / L = 1$

To investigate the effect of cilia coverage density on deposition enhancement, simulations are performed in which we vary spacing between cilia. The results are shown in Figure 5.7. We find that E varies non-monotonically with cilia spacing, showing maximum enhancement at about $\delta x = 1.1L$. This optimal density of cilia coverage is independent of the Schmidt number. A similar optimal spacing has been previously reported for heat transport enhancement by tilted oscillating cilia (76), in which case the

optimal spacing was related to the formation of flow structures in the ciliated layer. Smaller inter-cilial spacing prevents the development of circulatory flow currents, whereas excessive separation between neighboring cilia leaves parts of the fluid un-agitated.

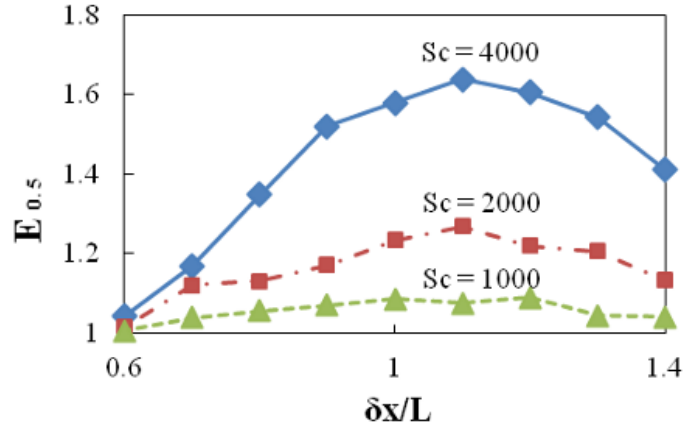


Figure 5.7 Dependence of E at 50% deposition on cilia spacing $\delta x/L$. The simulation parameters are $Sp = 3$, $A = 1$, and $\delta z = \delta x/2$

Finally, we investigate the effect of the magnitude of the cilia actuation force on deposition enhancement. As seen in Figure 5.8, E increases with increasing driving force amplitude for $A < 12$. For larger values of A , E saturates or even slightly decreases. In other words, an additional increase of the oscillating force beyond $A = 12$ is unable to further enhance the deposition of nano-particles. We can explain this by examining the displacement of oscillating cilia. We find that cilia displacement approaches a limiting cycle as the driving force is about $A = 12$. Further increase of the force magnitude essentially does not affect the cilium displacement and, therefore, has a weak effect on nano-particle deposition.

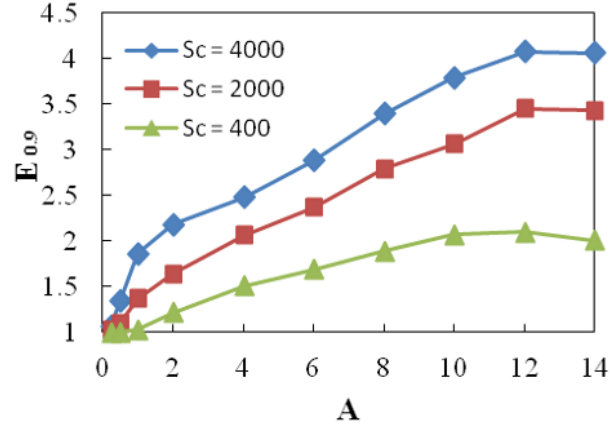


Figure 5.8 Dependence of E at 90% deposition on oscillation amplitude E for various Sc , $Sp = 3$, and $\delta x/L$

5.1.4 Microfluidic Mixing

In order to demonstrate local microfluidic mixing by oscillating flexible filaments, we simulated cilia beating at $Sp = 3$ and $A = 4$ due to an oscillating distributed force in a microchannel filled with a fluid initially containing two stratified concentration layers as described in section 3.2.3 and Figure 3.7. As seen in Figure 5.9a, the circulatory patterns created by these oscillating cilia produce local mixing, as is evident by the large region of light-colored fluid with circular streaks, located between the red and blue layers after several cilia oscillations. Figure 5.9b gives the degree of mixing over time for the case of mixing purely due to diffusion versus mixing enhanced by oscillating cilia, and we find that when cilia are used at $Sp = 3$, $A = 8$, and $Sc = 2000$, 80% mixing is reached 8 times faster than would happen if relying purely on diffusion.

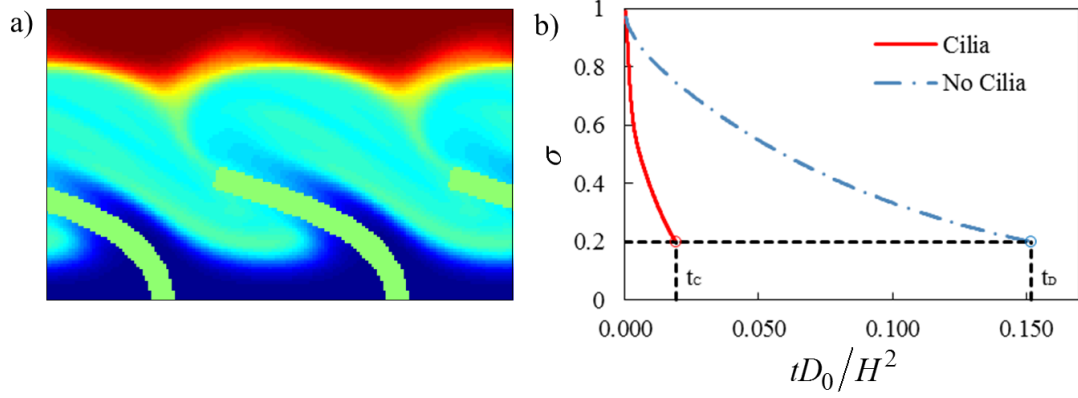


Figure 5.9 a) Concentration field in a microfluidic channel containing an array of flexible filaments driven by an oscillating distributed force at $Sp = 3$, $A = 8$, and $Sc = 2000$. Before mixing, the microchannel contained a layer of fluid with $C = 0$ (blue) and an equally thick layer with $C = 1$ (red). b) Time evolution of the degree of mixing of fluid layers in the case of Figure 5.9a (with cilia) and in a microchannel without cilia

We quantify mixing enhancement using a mixing enhancement parameter, which is once again given by $E_P = t_D/t_C$ giving the acceleration of mixing over mixing due purely to molecular diffusion. We found that as was the case with nano-particle deposition, mixing enhancement increases monotonically with increasing A , as seen in Figure 5.10. It is expected that local mixing enhancement of stratified fluid layers will behave similarly to nano-particle deposition, since the physical mechanism of local circulatory flows transporting fluid and particles vertically across the channel is shared by both processes. Thus, we do not devote further discussion to local microfluidic mixing, and instead focus on the use of asymmetric cilia oscillations for large-scale transport. The ribbon cilia were designed with this goal in mind.

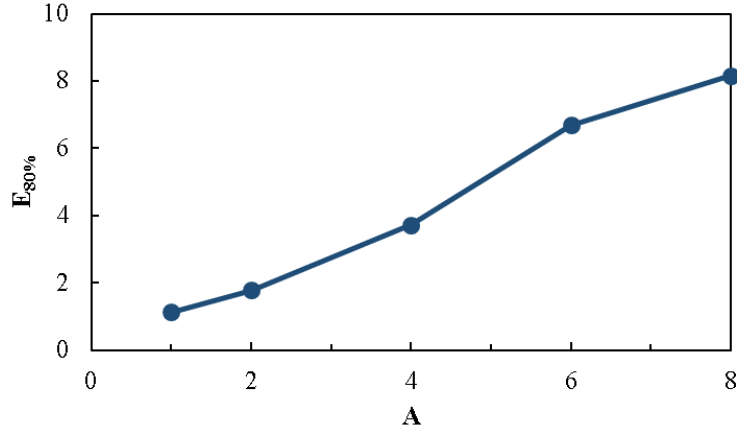


Figure 5.10 Mixing enhancement in a microfluidic channel containing an array of cilia driven by an oscillating distributed force at $Sp = 3$ and $Sc = 2000$ with varied A

5.2 Ribbon Cilia

We now turn our discussion to a numerical study of a second type of ciliated system which uses a simple asymmetric geometry of a flexible thin soft magnetic ribbon and a rotating magnetic B-field (Figure 3.6a) to create large-scale flow for microfluidic applications. We first study the dynamics of such a system to understand how the asymmetry inherent in the system results in a net fluid flow, and to determine how to best use the system to maximize time-irreversibility and asymmetry. We then investigate how the system can be utilized for microfluidic pumping. Finally, we explore the use of such cilia for creating large-scale transverse circulatory flow in a microchannel, so as to facilitate microfluidic mixing and particle capture applications.

5.2.1 Cilia Dynamics

In order to understand the dynamics of magnetically actuated ribbon-shaped cilia and its dependence on the balance between magnetic, elastic and viscous forces, we performed

simulations using the model described in section 3.2.2 and compared our results to recently obtained experimental images of similar cilia. We illustrate cilia dynamics using a series of experimental images that show the position of a cilium at several instances of time (Figure 5.11a), as well as a similar set of cilium positions obtained using our numerical model (Figure 5.11b). These cilia are driven by a uniform magnetic field that is rotating in the x-y plane. When the soft magnetic cilia are in a uniform magnetic field, they feel local magnetic moments acting to align the cilia with \mathbf{B} . As \mathbf{B} rotates counter-clockwise (CCW), the cilia are forced to maintain alignment with \mathbf{B} , and are thus driven from right to left in a power, or forward stroke (black arrows on the trajectory of the cilium tip shown in Figures 5.11a-b) which is dominated by the magnetic moment. When the cilia deflect sufficiently far that their internal elastic forces overcome the magnetic forces, the cilia no longer follow the rotating magnetic field, but instead rapidly snap back to the right in a recovery stroke (white and blue arrows in Figures 5.11a and 5.11b, respectively), due in large part to an elastic restoring force balanced by the viscous drag arising from the surrounding fluid. As seen from the tip trajectory in Figures 5.11a-b, the cilia follow highly asymmetric and time-irreversible stroke patterns in which the tip traces through an air-foil-shaped trajectory, due to the difference in the forces governing the forward and recovery strokes. This asymmetric beating pattern gives these cilia the capability of creating large-scale net flows, as will be shown in sections 5.2.3-4. In this case, the cilia push fluid to the left, and then bend down as they return to the right in their recovery stroke, pulling back less fluid and resulting in net fluid transport to the left.

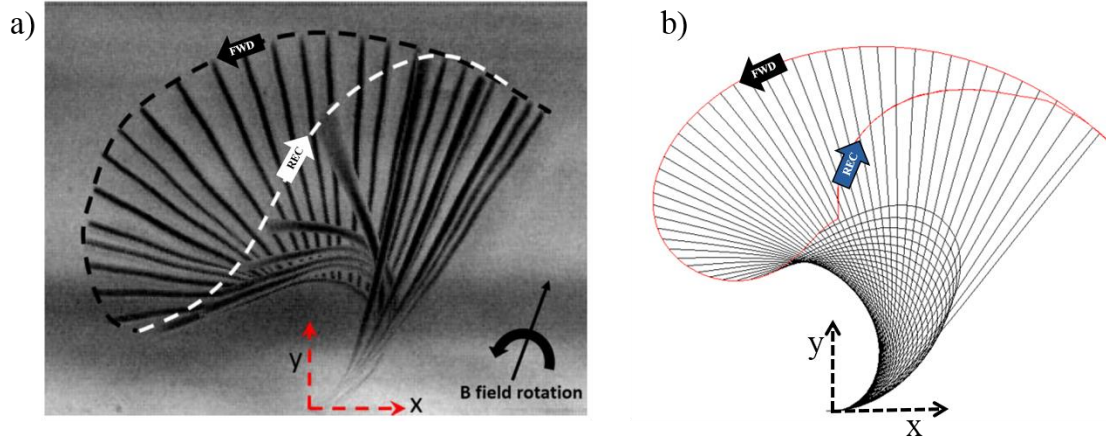


Figure 5.11 a) Series of experimentally-captured images of cilia at various instances of time throughout an oscillation cycle driven by CCW rotation of a magnetic B-field. The trajectory of the tip is denoted by the black and white dashed lines, which indicate the forward and recovery portions of the stroke, respectively. b) Similar images of cilia positions obtained using our numerical model

When the cilia have recovered to the point where they are aligned with the opposite pole of the B-field, they follow $-\mathbf{B}$ to repeat this oscillating cycle. This ability to follow the opposite pole occurs due to the soft magnetic cilia rapidly flipping their magnetization, and results in two oscillations of the cilia for every rotation of the magnetic field. As seen in Figure 5.11, simulation results (Figure 5.11b) capture the basic dynamics seen in images of experimental magnetic cilia (Figure 5.11a).

In order to better understand the complex dynamics of the cilia oscillation cycle, we consider the magnetic forcing experienced by the cilia throughout this cycle in more detail. As described in section 3.2.2, the magnetic moments experienced locally by each part of the cilia can be modelled to be proportional to $\sin(2\theta)$, where θ is the angle between magnetic field \mathbf{B} and the local axis of the cilium, as shown in Figure 3.6a. This captures the fact that cilia experience local moments driving them toward alignment with either the

direction of \mathbf{B} or $-\mathbf{B}$, whichever is closer, which occurs due to the ability of the cilia to change their magnetization such that it aligns with \mathbf{B} . Thus, if the local cilium axis is in alignment with \mathbf{B} or with $-\mathbf{B}$, then it will feel no local magnetic moment and will remain aligned with the field. As θ increases, the magnetic moment increases up to a maximum at 45° , before decreasing until there is no moment at $\theta = 90^\circ$. As θ increases further, the local cilium axis is now closer to $-\mathbf{B}$ and thus feels a moment driving it toward alignment with that direction.

We illustrate this forcing by considering the direction of \mathbf{B} when the cilium is at various positions throughout an oscillation cycle in the case of slow cilium oscillation, such that viscous drag is not sufficiently high to significantly alter cilia dynamics during the forward stroke. When the cilium begins its forward stroke at position a in Figure 5.12, the cilium is close to its equilibrium position (the position which the cilium assumes with no magnetic field) and much of the cilium (that is, all but the cilium base) is held in good alignment with \mathbf{B} by magnetic moments. As the field rotates CCW, the cilium remains mostly aligned with the field and follows it through positions b and c, driven by magnetic moments on the base of the cilium (bottom plots in Figure 5.12), which is primarily oriented less than 90° out from \mathbf{B} . As the cilium continues to follow the field to position d, most of the cilium still remains in alignment with \mathbf{B} , but the base of the cilium now has $\theta > 90^\circ$, resulting in a moment acting to align that part of the cilium with $-\mathbf{B}$. This results in the cilium being pulled by its base back to the right, even though the cilium tip remains aligned with \mathbf{B} . The amount of the cilium that experiences a moment toward $-\mathbf{B}$ increases as the cilium moves to positions e and f, where the cilium tip is now increasingly lagging behind \mathbf{B} .

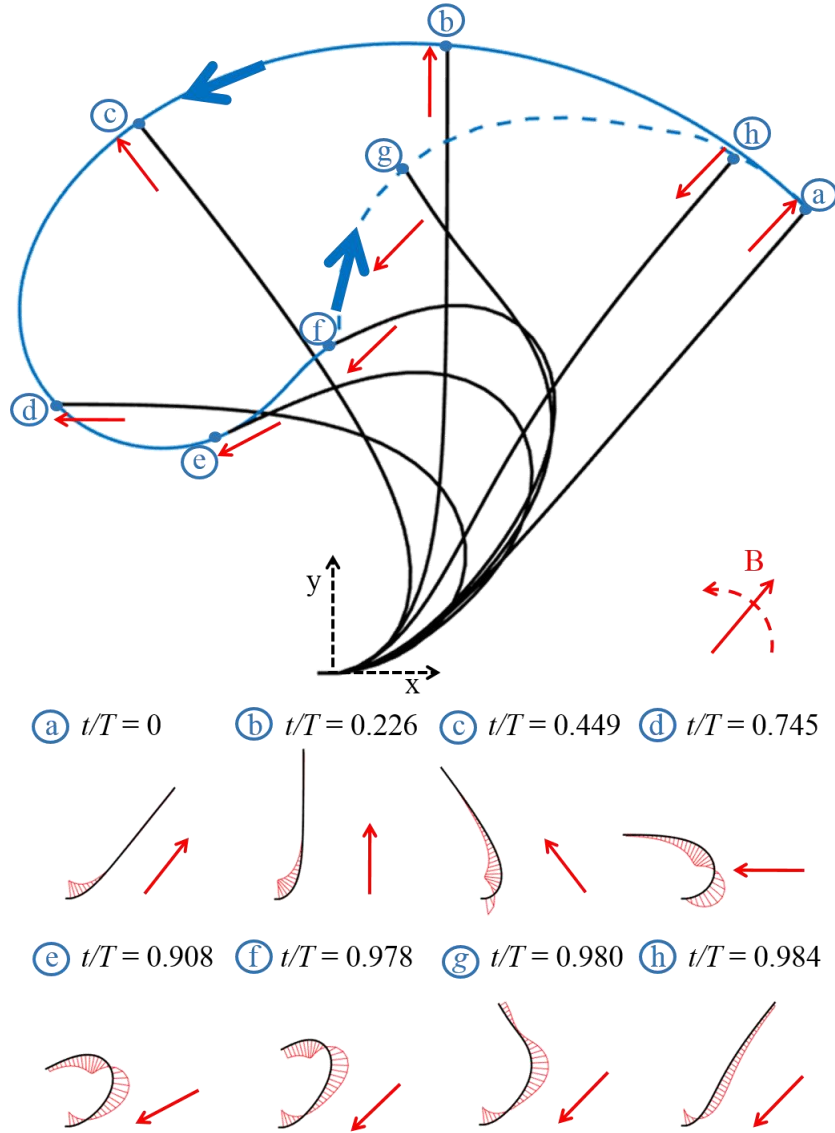


Figure 5.12 Cilium positions a-h at select times throughout the oscillation cycle given by black lines. For each cilium position, the corresponding B-field direction is given by a red arrow. The cilium tip (blue dots) traces out the tip trajectory through the forward and recovery strokes, as given in the top plot by the blue solid and dashed lines, respectively. At bottom, the magnitude and direction of the applied magnetic moment along the cilium length is given in red as a distribution plotted normal to the local cilium axis for the corresponding cilium positions at the given times t/T . While plotting the distribution normal to a curved axis gives the illusion of a sharp changes in the distribution, the magnetic moment and its spatial derivative both vary continuously along the cilium length

Shortly after position f, the cilium reaches a critical threshold where the magnetic moment pulling the cilium tip toward alignment with \mathbf{B} is no longer strong enough to

overcome the increasing elastic force due to bending of the cilium whose base is being pulled by magnetic moments toward $-\mathbf{B}$. At this critical point, the cilium snaps back in its recovery stroke, releasing its accumulated elastic energy as it relaxes through positions g and h. The rate of the recovery stroke is defined by the viscous drag on the cilium from the surrounding fluid. Once the elastic forces have driven the cilium through much of its recovery stroke, the cilium is now mostly aligned with $-\mathbf{B}$, and is driven by magnetic moments toward alignment with the field. The oscillation cycle then repeats.

Note that the recovery stroke is rapid as compared to the forward stroke, as evidenced by the large time difference between cilium positions a-f in Figure 5.12 as compared to those for positions f-h. The time stamps for each cilium position given at the bottom of Figure 5.12 are given as t/T , where t is the time from the beginning of the oscillation cycle until the cilium is at a given position, and T is the cilium oscillation period.

5.2.2 Characterizing Cilia Stroke Patterns

Now that we have a basic understanding of cilia dynamics and its governing forces, we investigate the effect of the balance of these forces using the dimensionless parameters described in section 3.2.2. These parameters are Mn , which gives the balance between magnetic and elastic forces, and Sp , which gives the balance between viscous and elastic forces.

We begin by comparing the trajectories of the tips of cilia driven at different values of Mn by varying the magnitude of \mathbf{B} . The various curves on Figure 5.13a and 5.13b give cilia trajectories for varied values of Mn obtained from experiments and simulations,

respectively. We find that cilia oscillated at high values of Mn move in such a way that they reach large deflections since in this case magnetic forces are strong as compared to elastic forces. As Mn is decreased, the cilia follow a similar trajectory as they did with high Mn , but the deflection of the cilia is decreased due to the reduced magnetic moments with respect to the elasticity of the cilia. As seen in Figure 5.13b, the simulations captured the experimentally-observed changes in cilia trajectories shown in Figure 5.13a.

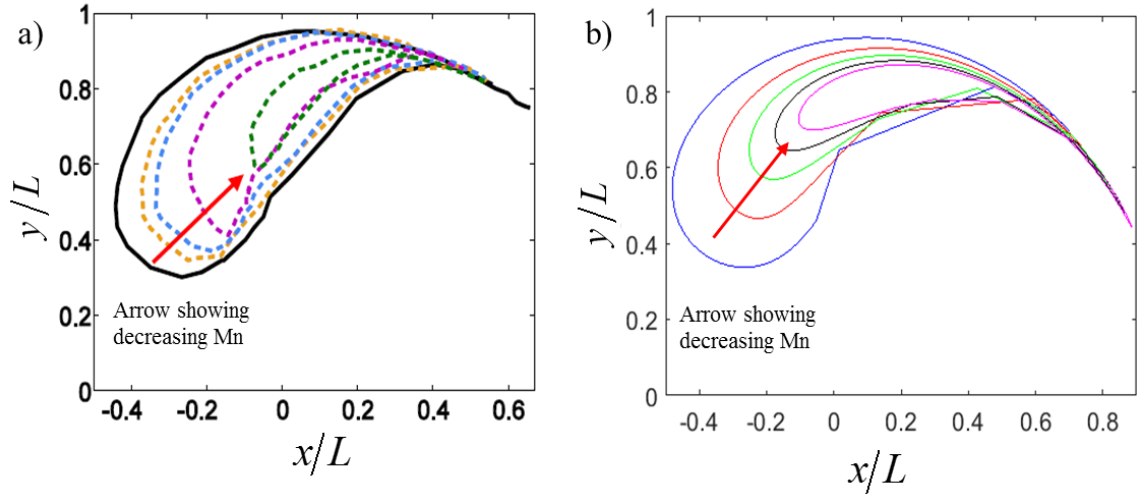


Figure 5.13 Cilia tip trajectories for varied values of Mn obtained by varying the magnitude of \mathbf{B} in a) experiments, and b) numerical simulations. Each colored curve represents a tip trajectory for a given value of Mn

We study the effect of the balance between viscous forces and magnetic and elastic forces by investigating the effect of Sp on cilia behavior. In order to do so, we first characterize cilia dynamic behavior through consideration of the time scales of the forward and recovery strokes. Specifically, we consider a dimensionless stroke irreversibility time,

$$T_s = \frac{t_{power} - t_{recovery}}{t_{power} + t_{recovery}} \quad (1)$$

where t_{power} is the time it takes a cilium to complete the power stroke portion of the oscillation cycle, and $t_{recovery}$ is the time in which the cilium completes its recovery stroke. This gives a simple way of characterizing the stroke irreversibility, as a large difference in the time taken to do the power stroke as compared to the recovery stroke indicates that the strokes are very different, due to a significant difference in the forcing for the respective parts of the oscillation cycle. Thus, a value of this dimensionless time approaching $T_s = 1$ denotes a highly-irreversible stroke, while a low value approaching $T_s = 0$ corresponds to a stroke in which the power and recovery strokes are similar to each other.

We now consider the effect of Sp on cilia dynamics by examining how T_s changes with changing Sp . As seen in in Figure 5.14a, simulations using varied ω , EI and ν showed that T_s decreases with increasing Sp for each given Mn . This is due to the increase in viscous forces with respect to elastic and magnetic forces, serving to dampen the velocity of the cilium and smooth out its stroke, reducing the ability of the cilium to closely follow **B** during the power stroke and providing resistance to the elasticity-driven recovery stroke. In the limit of low values of Sp , viscous forces are low enough that they do not hamper the ability of the cilium to follow **B**, allowing for an extended power stroke. In this case, low viscous forces allow for a rapid recovery stroke. This results in a dimensionless stroke time approaching $T_s = 1$. At high values of Sp , viscous forces provide for significant damping

in both strokes. Viscous drag causes the cilium to lag behind \mathbf{B} during the power stroke, decreasing the angle at which the cilium can no longer follow \mathbf{B} and shortening the power stroke. Viscous forces also act to dampen cilium motion during the recovery stroke, leading to an increased recovery stroke time. This combined effect leads to a low value of T_s at low Sp . In fact, in the limit of high Sp , high viscous drag results in cilia oscillating with very low deflection with little difference between the motion in forward and recovery strokes.

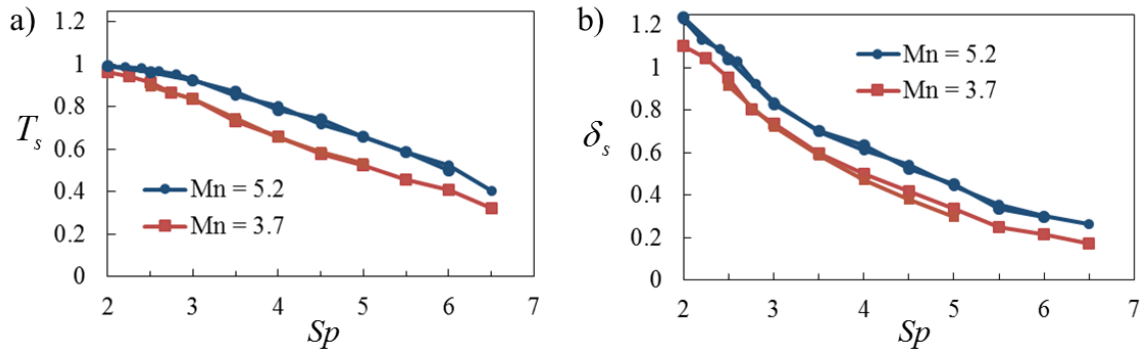


Figure 5.14 Characterization of the effect of Sp and Mn on cilia behavior. Blue and red curves represent characteristic non-dimensional values obtained from simulations with varied ω , EI and ν at two values of Mn over a wide range of Sp . a) Effect on the non-dimensional stroke irreversibility time, T_s . b) Effect on the normalized cilium displacement, δ_s

As seen in Figure 5.14a, T_s is also dependent on Mn . This is due to the fact that increasing Mn results in an increased ability of the cilium to follow \mathbf{B} , resulting in a longer power stroke to a larger deflection, which gives a larger elastic force to drive the recovery stroke.

In addition to T_s , the extent of the deflection of cilia is important to their dynamics. We characterize this deflection using a normalized deflection, $\delta_s = \delta_{\max} / L$, where δ_{\max} is the maximum distance between cilium tip points on the tip trajectory, such as points a and d on Figure 5.12 and L is the cilium length. As shown in Figure 5.14b, simulations showed that increasing Sp acted to decrease the deflection of cilia, due to increased fluid resistance to cilia movement.

5.2.3 *Microfluidic Pumping*

With an understanding of how ribbon-shaped cilia can be actuated to create high-amplitude highly irreversible and asymmetric strokes, we turn to the study of how this affects large-scale fluid transport. We begin by studying the creation of a net pumping flow down a microchannel. We do this using a simulation domain consisting of a single cilium, with periodic boundary conditions in the horizontal (x - and z -) directions, and solid walls on the top and bottom of the domain, as seen in Figure 3.6b. This simulates an infinitely wide and long microchannel, and gives us a simple and efficient way of investigating the use of cilia for microfluidic pumping.

5.2.3.1 Effect of Cilia Stroke Pattern

It has been shown that the amount of fluid propelled by a cilium is proportional to the area swept by the cilium in its oscillation cycle (89, 90). This is physically intuitive, since this area multiplied by a width represents the difference in the volume of fluid pushed forward (in the negative x -direction) in the power stroke as compared to the amount pulled backward (in the positive x -direction) in the recovery stroke. This allows us to

approximate the ability of the cilia to perform microfluidic pumping by measuring the area swept by its tip throughout its trajectory, as seen by the cilium tip trajectory curves in Figures 5.11-13.

In order to demonstrate that the swept area is in fact proportional to the volume of fluid pumped by an oscillating cilium, we performed simulations with cilia oscillating at varied Mn in a periodic array with x - and z - direction spacing of $\delta x = 1.2L$ and $\delta z = 0.2L$, respectively, in a channel of height $H/L = 1.1$. We tracked the tip trajectory so as to calculate a swept area, and also calculated the amount of fluid pumped in the negative x -direction by each cilium during each oscillation. As seen in the red curve in Figure 5.15, the area enclosed by the cilium tip trajectory, which we normalize by L^2 and denote as $A_{enclosed}$, increases linearly with increasing Mn . This is also evidenced by the increasingly small tip trajectories shown in Figure 5.13b, and is in line with the fact that increasing Mn increases both stroke irreversibility and deflection, as seen in the difference between the blue and red curves in Figures 5.14a-b. The volume of fluid pumped by a cilium in each oscillation was also linear, as evidenced by the pumping effectiveness shown in the blue curve in Figure 5.15. Indeed, when $A_{enclosed}$ is scaled by a factor of 1/4, it shows close correlation to the pumping effectiveness, as defined in section 5.1.2 and shown by the green curve in Figure 5.15. Thus, $A_{enclosed}$ is indeed proportional to pumping in our system, and can be used to investigate the effect of Sp on microfluidic pumping.

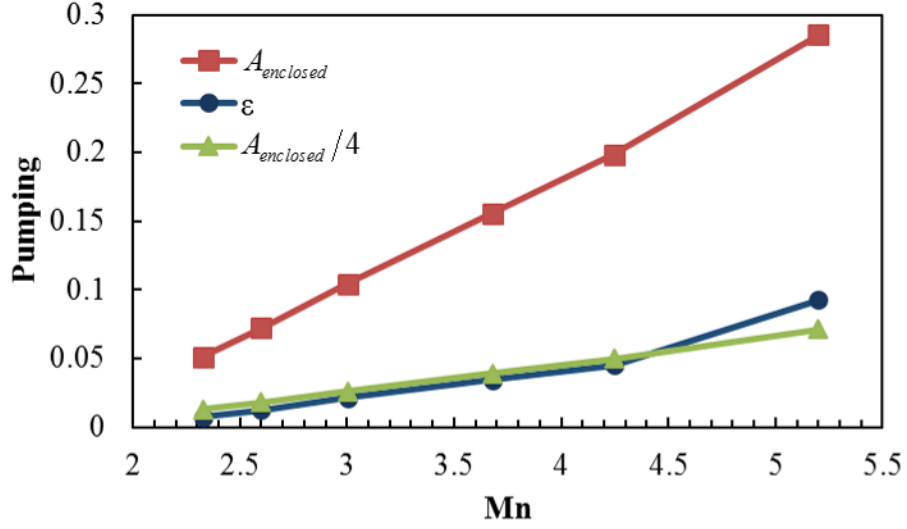


Figure 5.15 Measures of pumping per cycle by each cilium a periodic array of cilia oscillating at $Sp = 2$ for varied Mn in a channel with $H/L = 1.1$. The red and green curves give $A_{enclosed}$ and $A_{enclosed}/4$, respectively. The blue curve is the pumping effectiveness, ϵ

In order to understand the effect of Sp on cilia pumping, we performed simulations with cilia oscillating at varied frequencies in a periodic array with x – and z – direction spacing of $\delta x = 1.2L$ and $\delta z = 0.2L$, respectively, in a channel of height $H/L = 1.1$. We calculated $A_{enclosed}$ and found that it generally decreases with increasing Sp , as shown in Figure 5.16a. This is due to the decrease in stroke irreversibility and deflection as shown in Figure 5.14a-b, respectively. Thus, we expect that the amount of fluid pumped by a cilium in one oscillation cycle will generally decrease with increasing Sp .

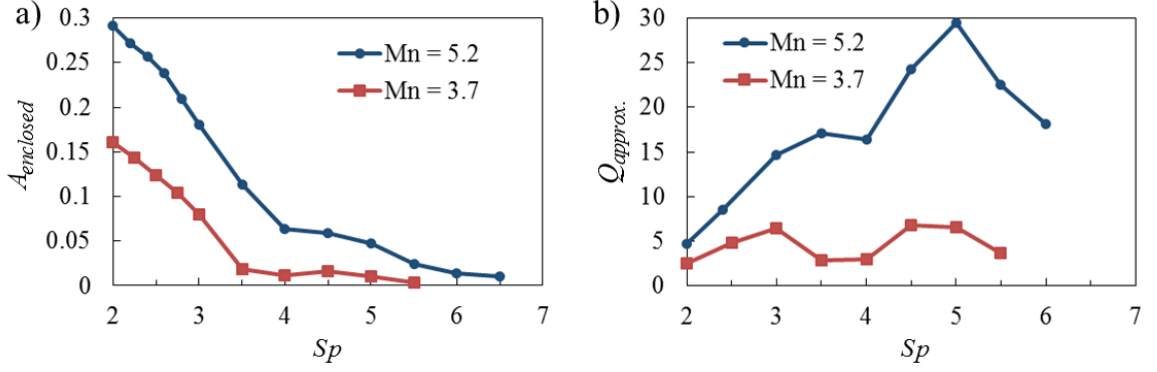


Figure 5.16 Approximation of pumping in a microchannel with cilia oscillating at varied Sp for two values of Mn . a) $A_{enclosed}$ as a function of Sp , giving an approximation of the amount of fluid pumped by each cilium oscillation. b) $Q_{approx.}$, which approximates the volumetric flow rate of fluid pumped by cilia

In order to approximate the volumetric flow rate achieved by oscillating cilia, one must also take into account the oscillation rate of the cilia, so as to arrive at a volume pumped per unit time. Thus, we approximate the volumetric flow rate as $Q_{approx.} = A_{enclosed} \omega / \omega_1$, where ω_1 is the oscillation frequency at $Sp = 1$ for a given parameter set. This serves to keep the resulting parameters dimensionless and to make the result dependent on Sp but not on specific system parameters that go into Sp . Since ω increases as Sp to the fourth power, it is to be expected that at least some of the decrease in pumping for a single oscillation will be offset by the increased stroke frequency. As seen in Figure 5.16b, there is indeed a non-monotonic relationship between $Q_{approx.}$ and Sp , with peaks near $Sp = 3$ and $Sp = 5$. This understanding helps us to know how microfluidic pumping can be controlled directly through control of the oscillation frequency.

5.2.3.2 Effect of Channel Geometry

In order to understand the effect of the height of a microchannel on the ability of oscillating cilia to induce pumping therein, we performed simulations with cilia oscillating at $Sp = 2$ in a periodic array with x - and z - direction spacing of $\delta x = 1.2L$ and $\delta z = 0.1L$, respectively, in channels of varied height, and calculated the volume of fluid pumped per cycle so as to determine the pumping effectiveness. As seen in Figure 5.17a, the pumping effectiveness increases almost linearly with increasing channel height. This suggests that the average velocity of fluid pumped through the channel is fairly constant with changes in H/L . In order to study the effect of H/L on the average pumping velocity, we introduce a channel-area normalized pumping effectiveness, $\varepsilon_{ch} = V_{pump,stroke} / \delta z HL$, which gives the volume of fluid pumped per cycle normalized by the cilium length and the channel cross-sectional area. The parameter ε_{ch} represents the normalized average displacement of fluid in the pumping direction during an oscillation cycle, and can be used to find the average fluid velocity for a given oscillation frequency and cilium length. For example, a cilium of length $L = 480 \mu m$ oscillating at 100 Hz would be expected to generate flow at around 2 cm/s. As seen in Figure 5.17b, we found that for cilia oscillating at two different values of Mn , ε_{ch} is relatively constant with varied H/L . There are variations in ε_{ch} with changing H/L especially in short channels in which the channel height is close to the cilium length, but in the limit of high H/L there is not much dependence of ε_{ch} on H/L .

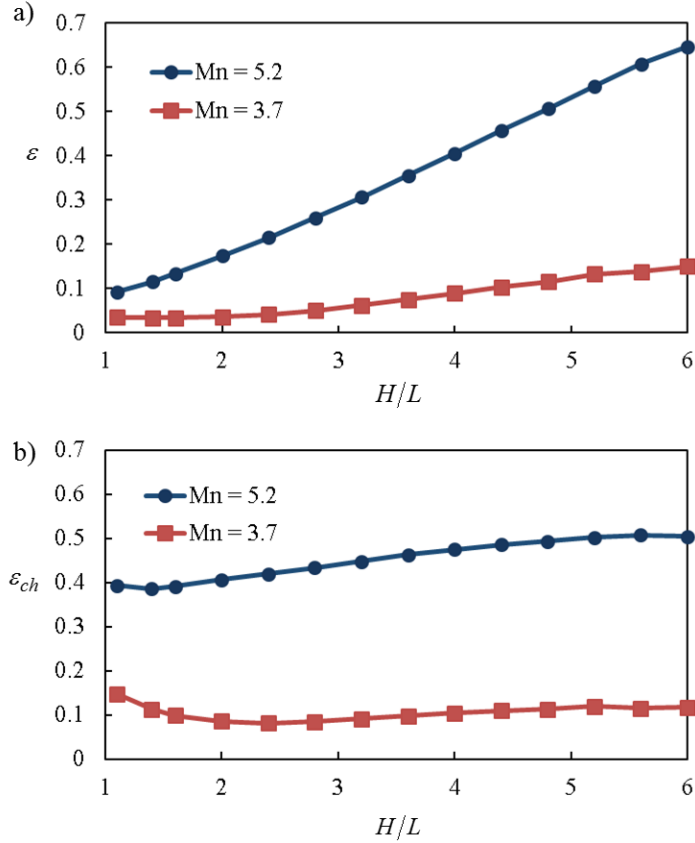


Figure 5.17 Calculated pumping effect of oscillating cilia. a) Effect of H/L on pumping effectiveness ε . b) Effect of H/L on channel-area normalized pumping effectiveness ε_{ch}

In order to understand why there is not much change in ε_{ch} with varied channel height, we consider the variation in period-averaged fluid velocity along the channel height, as shown in Figure 5.18a-b. Figure 5.18a gives the profile of the period-averaged velocity in the pumping (negative x -) direction, U_x , normalized by a reference velocity, U_{ref} , chosen to be the maximum velocity at this cross-section of a channel with $H/L = 6$. Here, the velocity profile is highly nonlinear in the section of the channel approximately up to the height of the cilia, which is denoted by the horizontal line at $H/L = 1$, but becomes linear above that. The negative pumping velocity transitioning to a peak positive velocity

profile at the bottom of the channel is due to the fact that the oscillating cilia create local CCW circulatory flow patterns in their vicinity. Above the local circulatory flow patterns, the velocity profile is linear. This is because fluid must meet no-slip conditions causing it to have the circulatory flow velocity at the top of the circulatory flow pattern, while having zero velocity at the stationary wall at the top of the channel. The velocity boundary conditions at the bottom and top of this section of fluid, similar to the classical Couette flow, results in the linear velocity profile present in shear flows. This linear velocity profile in the fluid above ciliated surfaces has been observed in experimental and physiological ciliated flows (91, 92).

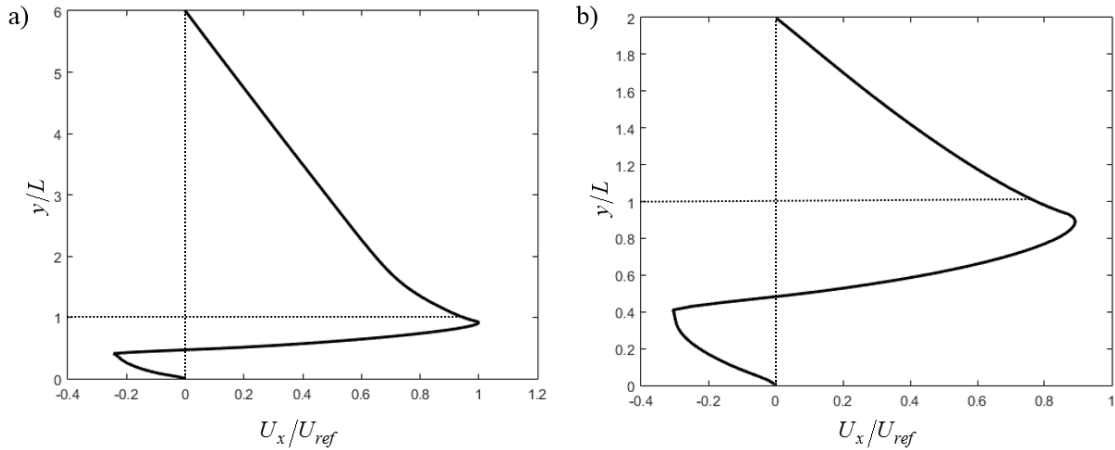


Figure 5.18 Profiles of the normalized velocity in the pumping (negative x –) direction for a) $H/L = 6$ and b) $H/L = 2$

As seen in Figure 5.18b, channels with $H/L = 2$ have a similar velocity profile, except that the maximum velocity (and thus the velocity at the top of the circulation pattern) is decreased slightly due to the proximity of the top wall. The decreased distance to the top wall gives an increased fluid shear stress to resist circulatory flow, since the flow velocity decreases over a much shorter distance than in the case of $H/L = 6$. Since the velocity

profile is nearly linear in a significant portion of the channel, the average velocity can be estimated as half of the velocity at the edge of the circulation pattern. This explains why the fluid velocity does not change much with increasing H/L , especially in the limit of large H/L . This nearly-constant average fluid velocity leads to the volumetric flow rate scaling linearly with the channel cross-sectional area and thus with the channel height. It is important to note that the dependence of pumping effectiveness on channel height as studied here applies specifically to a large array of cilia covering the microchannel floor of the entire channel in which fluid is to be pumped, and does not necessarily reflect behavior in different configurations. For example, less pumping would be expected in a channel in which a small region of cilia drives fluid through a longer section of channel, due to the increased fluid resistance in the extended channel length.

In addition to microfluidic applications, these findings are important to understanding the effect of cilia on transport in biological applications. The transport of a layer of fluid on top of circulatory flow regions in the vicinity of oscillating cilia has implications in a variety of biological and physiological applications, including mucociliary clearance.

5.2.4 Generating Large-Scale Circulatory Flow

In order to use oscillating cilia for microfluidic mixing and particle capture in continuous-flow devices, it can be desirable to controllably generate large-scale transverse circulatory flows. This helps to stretch fluid interfaces for mixing and to move fluid and particles past capture surfaces in applications such as bio-detection. Thus, we investigate the effect of channel geometry and cilia placement on generation of transverse flow by simulating cilia stretching across a microchannel of finite width $5.6L$, as depicted in Figure 3.6c. Cilia

oscillate at $Sp = 2$ and $Mn = 5.2$, and we vary the channel height and number of equally-spaced cilia across the channel. We use periodic boundary conditions in the axial (z -) direction, simulating a long microchannel with finite height and width.

We quantify generation of transverse flow across the channel as a normalized mean transverse velocity, $\bar{U}_x^* = \bar{U}_x / Lf$, where \bar{U}_x is the mean period-averaged velocity in the x -direction of fluid that is located above the height of the cilia and f is the frequency of cilia oscillation. We consider only the fluid above the height of the cilia since if we considered the entire channel height, then the average velocity would be zero due to conservation of mass.

As seen from comparison of the curves for one, two, three and four cilia across a microchannel in Figure 5.19, the transverse flow generation increases with increasing the number of cilia. This is in large part due to the fact that an increased number of cilia increases the ability to push fluid against resistance such as the viscous friction at the channel walls.

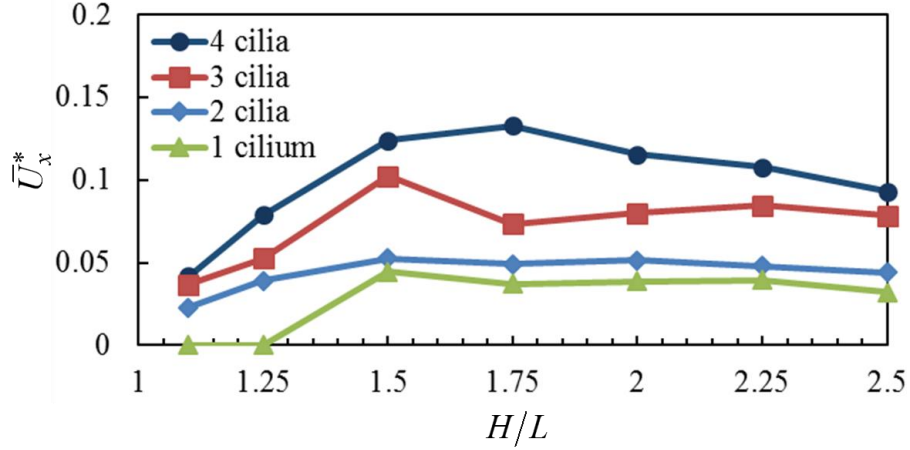


Figure 5.19 Normalized mean transverse velocity of flow generated by oscillating cilia oriented so as to push fluid across a microchannel. The four curves represent velocities for configurations using one, two, three or four cilia stretching across the channel with varied H/L

The lack of \bar{U}_x^* when using a single cilium across the width of the channel in geometries with $H/L=1.1$ and $H/L=1.25$, as seen in the green curve in Figure 5.19, results from the generation of a single pair of counter-rotating vortices each filling the entire height of the channel. When this happens, fluid is not able to travel across the entire height of the channel. Instead, fluid resides in either the vortex created by the oscillating cilium, or in its counter-rotating partner vortex. If more cilia are used in the channel, the size of vortices is reduced such that they do not occlude the entire height of the channel, and thus allow a net transverse flow at the top of the channel. Alternatively, if the channel height is increased to at least $H/L=1.5$, then the vortex created by the oscillating cilium does not reach the top of the channel, and it drives a large-scale circulation of fluid stretching across the entire width of the channel.

As seen in Figure 5.19, for all configurations \bar{U}_x^* is relatively low when the channel height is close to the cilium length, increases to a maximum value at around $1.5 < H/L < 1.75$, and then decreases as the channel height is further increased. The inability of cilia to provide for much transverse flow in the case of low H/L can be explained by the law of conservation of mass. Although the cilium stroke serves to push fluid, the fluid must have somewhere to go in order to be pumped, and if it does not then the cilium will not be able to displace it. In the case of pumping fluid in the transverse direction toward a solid wall, the problem is different than it was for axial pumping down a microchannel, since in the case of the solid wall the fluid needs to have space to return in the opposite direction.

One option for an avenue of returning fluid is to have enough space at the top of the channel in which fluid can return. Figure 5.20a gives the streamlines of a slice of the period-averaged velocity field at the centerline of cilia for the case of 4 cilia across a channel with $H/L = 1.1$. The cilia drive fluid in circulatory patterns, apparent here as the four large vortices. However, since the cilia are driving the fluid toward the left wall and the fluid does not have space to flow above the vortices, there is little large-scale circulation.

However, if the channel height is increased to $H/L = 1.5$, there is significant transverse flow, as seen in Figure 5.20b. Once again, the cilia create local circulatory patterns as seen by the four circular vortices located in the bottom half of the channel. There is also a significant amount of transverse flow weaving up and down between vortices and across the channel from right to left. This transverse flow is made possible by the flow of fluid

returning from left to right in the top portion of the channel, completing a large-scale transverse circulatory pattern of fluid stretching across the entire width of the channel. This allows for generation of transverse flow at significant and controllable velocities. For example, if this microchannel was used with four rows of cilia of length $L = 480\mu\text{m}$ stretching across a channel with $H/L = 1.5$, and were oscillated at 100 Hz, then transverse flow with an average velocity of over 7 mm/s would be expected. One could further optimize the use of a specific device for generation of transverse flows using the findings of section 5.2.3.1.

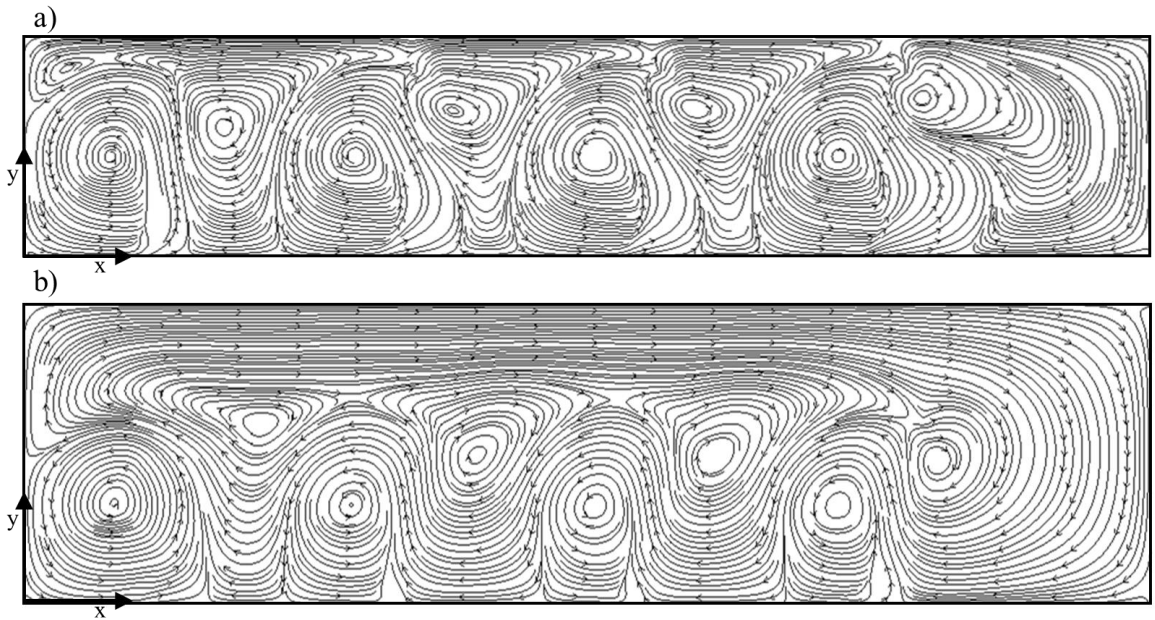


Figure 5.20 Plot of streamlines of a slice of the period-averaged velocity field at the centerline of cilia for the case of 4 cilia across a channel with a) $H/L = 1.1$, and b) $H/L = 1.5$. Cilia oscillate at the locations of the circulatory flow cells at the bottom of the channels, and arrows indicate the direction of flow

5.3 Summary

We used computational simulations to study the dynamics of two distinct types of magnetically actuated synthetic cilia, and investigated how to best use them for microfluidic transport applications.

We showed using a model of high-aspect-ratio cilia that cilia behavior is dependent on two dimensionless numbers: the sperm number Sp and force number A . Oscillating cilia create circulation patterns that are largest and strongest at $Sp = 3$. These cilia can be caused to create a net pumping effect if driven in asymmetric strokes using a modulated asymmetric forcing. We demonstrated that the flow circulation patterns generated by these cilia can be used for microfluidic mixing, and showed how to best use such cilia for capture of nanoscale particles on sensory surfaces.

We developed a model of high-aspect-ratio ribbon-shaped cilia, and explored the time-irreversible asymmetric cilium dynamics that these cilia exhibit when exposed to a rotating uniform magnetic field. Our model captures cilia behavior seen experimentally, and is used to understand the physics of the cilia-fluid interactions. We show that the behavior of these cilia is dependent on two dimensionless numbers: the sperm number Sp and the magneto-elastic number Mn . We characterize the time-irreversibility and deflection of cilia oscillations at various values of these dimensionless numbers, and show that fluid pumping can be approximated using the area swept by the cilia. Further, we investigate the effect of channel configuration on the generation of axial microfluidic pumping and transverse circulatory flow using oscillating cilia, and show that significant fluid transport can be created by use of these cilia. These cilia require power input on the order of a microwatt,

which is approximately greater than the power required to drive flow through a microchannel, but still much lower than the power lost to heat in a typical motor as would be used to rotate the magnet used for the magnetic field.

Our findings not only guide the efficient design of microfluidic devices utilizing oscillating synthetic cilia, but can be applicable in understanding the behavior of biological cilia and their effect on fluid transport.

CHAPTER 6. CONCLUDING REMARKS AND OUTLOOK

In this dissertation, we have studied the fluid and solid dynamics of two different types of magnetically actuated structures for use in microfluidic devices with mixing and particle capture applications. Specifically, we studied the behavior and application of a system that uses superparamagnetic microbeads moving in controlled orbits through a fluid sample, so as to mix the fluid and capture particles therefrom. We also studied the dynamics of actuated synthetic cilia, and investigated their use in microfluidic applications. We studied these systems using fully coupled 3-D computer simulations which modeled fluid and solid dynamics as well as mass transport phenomena, allowing for an in-depth investigation of system behavior and for the study of these systems in a wide variety of geometries and conditions.

A microfluidic device that utilizes magnetic microbeads orbiting around NiFe discs patterned on a microchannel floor to provide for microfluidic mixing and micro-particle capture was investigated computationally and validated by comparison with experiments. We showed that orbiting microbeads can lead to rapid fluid mixing in low Reynolds number flow, and identified two distinct mixing mechanisms. Bulk advection of fluid across the channel occurs due to the flow pattern that is developed when the ratio of flow velocity to bead velocity is low, and leads to rapid mixing. At higher velocity ratios, dispersion of small amounts of fluid across the channel occurs, and results in increased mixing. We used simulations to investigate the effect of system parameters on mixing performance, so as to guide the effective design of such microfluidic devices for microfluidic mixing applications.

Further, we investigated the ability of orbiting magnetic microbeads to capture particles from fluid samples. We found that orbiting beads are effective at promoting contact between beads and target particles, allowing for efficient particle capture in short distances. Flow patterns created by beads assist them in drawing particles down to the height of the beads, enabling capture from channels up to six times as tall as the beads. We investigated the effect of system parameters on the distance required for sufficient particle capture, enabling an understanding of how to best use the device for efficient micro-particle capture.

Additionally, we used computational simulations to study the dynamics of two distinct types of magnetically actuated synthetic cilia, and investigated how to best use them for microfluidic transport applications.

We showed using a model of high-aspect-ratio filament cilia that cilia behavior is dependent on two dimensionless numbers: the sperm number Sp and force number A . Oscillating cilia create circulation patterns that are the largest and strongest at $Sp = 3$. These cilia can be caused to create a net pumping effect if driven in asymmetric strokes using a modulated asymmetric forcing. We demonstrated that the flow circulation patterns generated by these cilia can be used for microfluidic mixing, and showed how to best use such cilia for capture of nanoscale particles on sensory surfaces.

We developed a model of high-aspect-ratio ribbon-shaped cilia, and explored the time-irreversible asymmetric dynamics that these cilia exhibit when exposed to a rotating uniform magnetic field. Our model captures cilia behavior seen experimentally, and is used to understand the physics governing cilia kinematics. We show that the behavior of these cilia depends on two dimensionless numbers: the sperm number Sp and the magneto-

elastic number, Mn . We characterize the time-irreversibility and deflection of cilia oscillations at various values of these dimensionless numbers, and show that fluid pumping can be approximated using the area swept by the cilia. Further, we investigate the effect of channel configuration on the generation of axial microfluidic pumping and transverse circulatory flow using oscillating cilia, and show that significant fluid transport can be created by use of these cilia.

Our findings on the use of orbiting microbeads demonstrate that they can effectively be used for both microfluidic mixing and micro-particle capture, and provide important understanding of the system and how to best use it in microfluidic applications. Orbiting magnetic microbeads, when functionalized, can be used in multi-functional devices for both microfluidic mixing and for specific detection of even small concentrations of microscale particles that can be readily extracted for further analysis, with important implications in bio-detection. Further efforts on study of such a device would be well served to focus on capture of live cells, so as to understand how the binding kinetics of specific target cells in sample fluids will affect capture, and to put this device to use in its intended function. Further, work should be done to scale up the throughput of this device by using multiple micro-channels in parallel on a device such as a lab-on-a-disc. Finally, this device should be incorporated into an overall device design so as to include the entire process from sample preparation and possible filtering, through capture, and finally to detection and quantification of captured cells.

Our findings on magnetically actuated cilia not only guide the efficient design of microfluidic devices utilizing oscillating synthetic cilia, but can be applicable in understanding the behavior of biological cilia and their effect on fluid transport. A valuable

extension of this work could be done to improve our understanding of how cilia can pump non-Newtonian fluids and stratified layers of fluids, with applications in areas such as muco-ciliary clearance. The ribbon-shaped cilia should further be investigated for use in capture of small concentrations of microscale particles, since they allow for the use of channel of large cross-section for significant sample throughput. Finally, ribbon-shaped cilia should be studied in continuous-flow applications to quantify their ability to use generated transverse flow for microfluidic mixing applications, and to determine how well a small array of cilia can pump fluid through channels of extended length.

REFERENCES

1. Daw R, Finkelstein J. Lab on a chip. *Nature*. 2006;442(7101):367-.
2. Figeys D, Pinto D. Lab-on-a-chip: a revolution in biological and medical sciences. *Anal Chem*. 2000;72(9):330 A-5 A.
3. Purcell EM. Life at Low Reynolds-Number. *Am J Phys*. 1977;45(1):3-11. PubMed PMID: ISI:A1977CS64300001.
4. Owen D, Mao W, Alexeev A, Cannon J, Hesketh P. Microbeads for sampling and mixing in a complex sample. *Micromachines*. 2013;4:103–15.
5. Riisgard HU, Larsen PS. Minireview: Ciliary filter feeding and bio-fluid mechanics - present understanding and unsolved problems. *Limnology and Oceanography*. 2001;46(4):882-91. PubMed PMID: ISI:000169214600013.
6. Sleigh MA. Adaptations of ciliary systems for the propulsion of water and mucus. *Comparative Biochemistry and Physiology a-Physiology*. 1989;94(2):359-64. PubMed PMID: ISI:A1989AZ56500028.
7. Satir P, Christensen ST. Overview of structure and function of mammalian cilia. *Ann Rev Physiology*. 2007;69:377-400. doi: DOI 10.1146/annurev.physiol.69.040705.141236. PubMed PMID: ISI:000245334100020.
8. Wiggins CH, Riveline D, Ott A, Goldstein RE. Trapping and wiggling: Elastohydrodynamics of driven microfilaments. *Biophys J*. 1998;74(2):1043-60. doi: 10.1016/S0006-3495(98)74029-9. PubMed PMID: ISI:000073393500037.
9. Brennen C, Winet H. Fluid-Mechanics of Propulsion by Cilia and Flagella. *Annu Rev Fluid Mech*. 1977;9:339-98. PubMed PMID: ISI:A1977CS66100014.
10. Oh K, Chung JH, Devasia S, Riley JJ. Bio-mimetic silicone cilia for microfluidic manipulation. *Lab Chip*. 2009;9(11):1561-6. doi: Doi 10.1039/B817409a. PubMed PMID: ISI:000266269400012.
11. Evans BA, Shields AR, Carroll RL, Washburn S, Falvo MR, Superfine R. Magnetically actuated nanorod arrays as biomimetic cilia. *Nano Lett*. 2007;7(5):1428-34. doi: Doi 10.1021/NI070190c. PubMed PMID: ISI:000246313000056.
12. Oh K, Smith B, Devasia S, Riley JJ, Chung JH. Characterization of mixing performance for bio-mimetic silicone cilia. *Microfluid Nanofluid*. 2010;9(4-5):645-55. doi: DOI 10.1007/s10404-010-0578-3. PubMed PMID: ISI:000281483400005.
13. Babataheri A, Roper M, Fermigier M, Du Roure O. Tethered fleximags as artificial cilia. *J Fluid Mech*. 2011;678:5-13.

14. Khaderi SN, Craus CB, Hussong J, Schorr N, Belardi J, Westerweel J, Prucker O, Ruhe J, den Toonder MJM, Onck PR. Magnetically-actuated artificial cilia for microfluidic propulsion. *Lab Chip*. 2011;11(12):2002-10.
15. Keißner A, Brücker C. Directional fluid transport along artificial ciliary surfaces with base-layer actuation of counter-rotating orbital beating patterns. *Soft Matter*. 2012;8(19):5342-9.
16. Whitesides GM. The origins and the future of microfluidics. *Nature*. 2006;442(7101):368-73.
17. Stroock AD, Dertinger SKW, Ajdari A, Mezic I, Stone HA, Whitesides GM. Chaotic mixer for microchannels. *Science*. 2002;295(5555):647-51. PubMed PMID: ISI:000173560900035.
18. Lee C-Y, Chang C-L, Wang Y-N, Fu L-M. Microfluidic mixing: a review. *International journal of molecular sciences*. 2011;12(5):3263-87.
19. Liu RH, Stremler MA, Sharp KV, Olsen MG, Santiago JG, Adrian RJ, Aref H, Beebe DJ. Passive mixing in a three-dimensional serpentine microchannel. *J Microelectromech S*. 2000;9(2):190-7.
20. Ménégaud V, Josserand J, Girault HH. Mixing processes in a zigzag microchannel: finite element simulations and optical study. *Anal Chem*. 2002;74(16):4279-86.
21. Schönfeld F, Hessel V, Hofmann C. An optimised split-and-recombine micro-mixer with uniform 'chaotic' mixing. *Lab Chip*. 2004;4(1):65-9.
22. Liu RH, Lenigk R, Druyor-Sanchez RL, Yang J, Grodzinski P. Hybridization enhancement using cavitation microstreaming. *Anal Chem*. 2003;75(8):1911-7.
23. Ahmed D, Mao X, Juluri BK, Huang TJ. A fast microfluidic mixer based on acoustically driven sidewall-trapped microbubbles. *Microfluid Nanofluid*. 2009;7(5):727-31.
24. Harnett CK, Templeton J, Dunphy-Guzman KA, Senousy YM, Kanouff MP. Model based design of a microfluidic mixer driven by induced charge electroosmosis. *Lab Chip*. 2008;8(4):565-72.
25. Lu L-H, Ryu KS, Liu C. A magnetic microstirrer and array for microfluidic mixing. *J Microelectromech S*. 2002;11(5):462-9.
26. Rida A, Gijs M. Manipulation of self-assembled structures of magnetic beads for microfluidic mixing and assaying. *Anal Chem*. 2004;76(21):6239-46.
27. Gijs MA, Lacharme F, Lehmann U. Microfluidic applications of magnetic particles for biological analysis and catalysis. *Chemical reviews*. 2009;110(3):1518-63.

28. Mao W, Peng Z, Hesketh PJ, Alexeev A. Microfluidic mixing using an array of superparamagnetic beads. *Bulletin of the American Physical Society*. 2011;56.
29. Ivnitski D, Abdel-Hamid I, Atanasov P, Wilkins E. Biosensors for detection of pathogenic bacteria. *Biosensors and Bioelectronics*. 1999;14(7):599-624.
30. Bouguelia S, Roupioz Y, Slimani S, Mondani L, Casabona MG, Durmort C, Vernet T, Calemczuk R, Livache T. On-chip microbial culture for the specific detection of very low levels of bacteria. *Lab Chip*. 2013;13(20):4024-32.
31. Tekin HC, Gijs MA. Ultrasensitive protein detection: a case for microfluidic magnetic bead-based assays. *Lab Chip*. 2013;13(24):4711-39.
32. Adams JD, Kim U, Soh HT. Multitarget magnetic activated cell sorter. *Proceedings of the National Academy of Sciences*. 2008;105(47):18165-70.
33. Xia N, Hunt TP, Mayers BT, Alsberg E, Whitesides GM, Westervelt RM, Ingber DE. Combined microfluidic-micromagnetic separation of living cells in continuous flow. *Biomedical Microdevices*. 2006;8(4):299-308.
34. Liu RH, Yang J, Lenigk R, Bonanno J, Grodzinski P. Self-contained, fully integrated biochip for sample preparation, polymerase chain reaction amplification, and DNA microarray detection. *Anal Chem*. 2004;76(7):1824-31.
35. Proczek G, Gassner A-L, Busnel J-M, Girault HH. Total serum IgE quantification by microfluidic ELISA using magnetic beads. *Anal Bioanal Chem*. 2012;402(8):2645-53.
36. Beyor N, Seo TS, Liu P, Mathies RA. Immunomagnetic bead-based cell concentration microdevice for dilute pathogen detection. *Biomedical microdevices*. 2008;10(6):909-17.
37. Tennico YH, Hutanu D, Koesdjojo MT, Bartel CM, Remcho VT. On-chip aptamer-based sandwich assay for thrombin detection employing magnetic beads and quantum dots. *Anal Chem*. 2010;82(13):5591-7.
38. Ambrosi A, Guix M, Merkoçi A. Magnetic and electrokinetic manipulations on a microchip device for bead-based immunosensing applications. *Electrophoresis*. 2011;32(8):861-9.
39. Sivagnanam V, Song B, Vandevyver C, Bünzli J-CG, Gijs MA. Selective breast cancer cell capture, culture, and immunocytochemical analysis using self-assembled magnetic bead patterns in a microfluidic chip. *Langmuir*. 2010;26(9):6091-6.
40. Furdyi VI, Harrison DJ. Immunomagnetic T cell capture from blood for PCR analysis using microfluidic systems. *Lab Chip*. 2004;4(6):614-8.
41. Boehm DA, Gottlieb PA, Hua SZ. On-chip microfluidic biosensor for bacterial detection and identification. *Sensors and Actuators B: Chemical*. 2007;126(2):508-14.

42. Alexeev A, Verberg R, Balazs AC. Modeling the motion of microcapsules on compliant polymeric surfaces. *Macromolecules*. 2005;38(24):10244-60. PubMed PMID: ISI:000233524900047.
43. Alexeev A, Verberg R, Balazs AC. Designing compliant substrates to regulate the motion of vesicles. *Phys Rev Lett*. 2006;96(14):148103. PubMed PMID: ISI:000236797200075.
44. Bouzidi M, Firdaouss M, Lallemand P. Momentum transfer of a Boltzmann-lattice fluid with boundaries. *Phys Fluids*. 2001;13(11):3452-9. PubMed PMID: ISI:000171569600030.
45. Succi S. The lattice Boltzmann equation for fluid dynamics and beyond. Oxford: Oxford University Press; 2001. xvi, 288 p. p.
46. Ladd AJC, Verberg R. Lattice-Boltzmann simulations of particle-fluid suspensions. *J Stat Phys*. 2001;104(5-6):1191-251. PubMed PMID: ISI:000171472100012.
47. Dawson SP, Chen S, Doolen GD. Lattice Boltzmann computations for reaction-diffusion equations. *The Journal of chemical physics*. 1993;98(2):1514-23.
48. Zhang T, Shi B, Guo Z, Chai Z, Lu J. General bounce-back scheme for concentration boundary condition in the lattice-Boltzmann method. *Phys Rev E*. 2012;85(1):016701.
49. Buxton GA, Care CM, Cleaver DJ. A lattice spring model of heterogeneous materials with plasticity. *Model Simul Mater Sc*. 2001;9(6):485-97. PubMed PMID: ISI:000172464400002.
50. Ostoja-Starzewski M. Lattice models in micromechanics. *Applied Mechanics Reviews*. 2002;55(1):35-60.
51. Gusev AA. Finite element mapping for spring network representations of the mechanics of solids. *Phys Rev Lett*. 2004;93(3):034302. PubMed PMID: ISI:000222691900019.
52. Monette L, Anderson M. Elastic and fracture properties of the two-dimensional triangular and square lattices. *Model Simul Mater Sc*. 1994;2(1):53.
53. Mao W. Modeling particle suspensions using lattice Boltzmann method [PhD thesis]; Georgia Institute of Technology; 2013.
54. Verlet L. Computer Experiments on Classical Fluids. Part I. Thermodynamical Properties of Lennard-Jones Molecules. *Physical Review*. 1967;159(1):98-103. PubMed PMID: ISI:A19679693500017.

55. Verlet L. Computer Experiments on Classical Fluids. Part 2. Equilibrium Correlation Functions. *Physical Review*. 1968;165(1):201-14. PubMed PMID: ISI:A1968A471500028.
56. Verberg R, Alexeev A, Balazs AC. Modeling the release of nanoparticles from mobile microcapsules. *J Chem Phys*. 2006;125(22):224712. PubMed PMID: ISI:000242855800034.
57. Ballard M, Mills Z, Beckworth S, Alexeev A. Enhancing nanoparticle deposition using actuated synthetic cilia. *Microfluid Nanofluid*. 2014;17(2):317-24. doi: 10.1007/s10404-013-1308-4.
58. Marsaglia G, Tsang WW. The ziggurat method for generating random variables. *Journal of statistical software*. 2000;5(8):1-7.
59. Walsh S, Saar M. Interpolated lattice Boltzmann boundary conditions for surface reaction kinetics. *Phys Rev E*. 2010;82(6):066703.
60. Ballard M, Owen D, Mills ZG, Hesketh PJ, Alexeev A. Orbiting magnetic microbeads enable rapid microfluidic mixing. *Microfluid Nanofluid*. 2016;20(6):1-13.
61. Owen D, Ballard M, Alexeev A, Hesketh PJ. Rapid Microfluidic Mixing via Rotating Magnetic Microbeads. *Sensors and Actuators A: Physical*. 2016;251:84-91.
62. Dasgupta PK, Liu S. Electroosmosis: a reliable fluid propulsion system for flow injection analysis. *Anal Chem*. 1994;66(11):1792-8.
63. Weigl BH, Bardell RL, Cabrera CR. Lab-on-a-chip for drug development. *Adv Drug Deliver Rev*. 2003;55(3):349-77.
64. Dittrich PS, Schuille P. An integrated microfluidic system for reaction, high-sensitivity detection, and sorting of fluorescent cells and particles. *Anal Chem*. 2003;75(21):5767-74.
65. Fu AY, Chou H-P, Spence C, Arnold FH, Quake SR. An integrated microfabricated cell sorter. *Anal Chem*. 2002;74(11):2451-7.
66. Furlani EP. Permanent magnet and electromechanical devices: materials, analysis, and applications: Academic press; 2001.
67. Furlani E. Analysis of particle transport in a magnetophoretic microsystem. *Journal of Applied Physics*. 2006;99(2):024912.
68. Rosensweig RE. *Ferrohydrodynamics*. Mineola, NY: Dover Publications; 1997. xv, 344 p. p.
69. Owen D. Mixing and sampling in a microfluidic channel using rotating magnetic microbeads [Ph.D. Dissertation]: Georgia Institute of Technology; 2016.

70. Ghosh R, Buxton GA, Usta OB, Balazs AC, Alexeev A. Designing Oscillating Cilia That Capture or Release Microscopic Particles. *Langmuir*. 2010;26(4):2963-8. doi: Doi 10.1021/La902926w. PubMed PMID: ISI:000274342200113.
71. Alexeev A, Yeomans JM, Balazs AC. Designing synthetic, pumping cilia that switch the flow direction in microchannels. *Langmuir*. 2008;24(21):12102-6. doi: Doi 10.1021/La801907x. PubMed PMID: ISI:000260508800003.
72. Yeh PD, Alexeev A. Biomimetic flexible plate actuators are faster and more efficient with a passive attachment. *Acta Mechanica Sinica*. 2016;32(6):1001-11.
73. Masoud H, Alexeev A. Resonance of flexible flapping wings at low Reynolds number. *Phys Rev E*. 2010;81(5):056304. doi: Artn 056304 Doi 10.1103/Physreve.81.056304. PubMed PMID: ISI:000278148500035.
74. Alexeev A, Verberg R, Balazs AC. Modeling the interactions between deformable capsules rolling on a compliant surface. *Soft Matter*. 2006;2(6):499-509. PubMed PMID: ISI:000238912500006.
75. Kilimnik A, Mao W, Alexeev A. Inertial migration of deformable capsules in channel flow. *Phys Fluids*. 2011;23(12):123302.
76. Mills ZG, Aziz B, Alexeev A. Beating synthetic cilia enhance heat transport in microfluidic channels. *Soft Matter*. 2012;8(45):11508-13. doi: Doi 10.1039/C2sm26919h. PubMed PMID: ISI:000310829800013.
77. Mao W, Alexeev A. Hydrodynamic sorting of microparticles by size in ridged microchannels. *Phys Fluids*. 2011;23(5):051704.
78. Mao WB, Alexeev A. Motion of spheriod particles in shear flow with inertia. *J Fluid Mech*. 2014;749:145-66. doi: Doi 10.1017/Jfm.2014.224. PubMed PMID: WOS:000337922700006.
79. Yeh PD, Alexeev A. Free swimming of an elastic plate plunging at low Reynolds number. *Phys Fluids*. 2014;26(5):053604. doi: Artn 053604 Doi 10.1063/1.4876231. PubMed PMID: WOS:000337103900026.
80. Yeh PD, Alexeev A. Effect of aspect ratio in free-swimming plunging flexible plates. *Comput Fluids*. 2016;124:220-5.
81. Chen L. An integral approach for large deflection cantilever beams. *Int J Nonlin Mech*. 2010;45(3):301-5.
82. Lauga E, Powers TR. The hydrodynamics of swimming microorganisms. *Rep Prog Phys*. 2009;72(9):096601.
83. Nadim A, Cox R, Brenner H. Taylor dispersion in concentrated suspensions of rotating cylinders. *J Fluid Mech*. 1986;164:185-215.

84. Guglielmini L, Kushwaha A, Shaqfeh ESG, Stone HA. Buckling transitions of an elastic filament in a viscous stagnation point flow. *Phys Fluids*. 2012;24(12). doi: Artn 123601 Doi 10.1063/1.4771606. PubMed PMID: WOS:000312833500022.
85. Vogel R, Stark H. Motor-driven bacterial flagella and buckling instabilities. *Eur Phys J E*. 2012;35(2). doi: Artn 15 Doi 10.1140/Epje/I2012-12015-0. PubMed PMID: WOS:000301433500006.
86. Son K, Guasto JS, Stocker R. Bacteria can exploit a flagellar buckling instability to change direction. *Nat Phys*. 2013;9(8):494-8. doi: 10.1038/nphys2676 <http://www.nature.com/nphys/journal/v9/n8/abs/nphys2676.html#supplementary-information>.
87. Landau LD, Lifshitz EM. *Theory of elasticity*. 2d English ed. Oxford, New York: Pergamon Press; 1970. viii, 165 p. p.
88. Witman GB. *Introduction to cilia and flagella. Ciliary and flagellar membranes*: Springer; 1990. p. 1-30.
89. Golestanian R, Ajdari A. Analytic results for the three-sphere swimmer at low Reynolds number. *Phys Rev E*. 2008;77(3):036308.
90. Khaderi SN, Baltussen MGHM, Anderson PD, Ioan D, den Toonder MJM, Onck PR. Nature-inspired microfluidic propulsion using magnetic actuation. *Phys Rev E*. 2009;79(4):- . doi: Artn 046304 Doi 10.1103/Physreve.79.046304. PubMed PMID: ISI:000265941400046.
91. Shields AR, Fiser BL, Evans BA, Falvo MR, Washburn S, Superfine R. Biomimetic cilia arrays generate simultaneous pumping and mixing regimes. *P Natl Acad Sci USA*. 2010;107(36):15670-5. doi: DOI 10.1073/pnas.1005127107. PubMed PMID: ISI:000281637800010.
92. Okada Y, Takeda S, Tanaka Y, Belmonte J-CI, Hirokawa N. Mechanism of nodal flow: a conserved symmetry breaking event in left-right axis determination. *Cell*. 2005;121(4):633-44.

VITA

Matthew Ballard was raised in North Salt Lake, Utah. After serving as a missionary in Russia for two years, he attended Brigham Young University, where he received his B.S. in Mechanical Engineering in 2009. He worked as a flight test engineer until 2012, when he began his graduate studies at Georgia Tech as a member of the Complex Fluids Modeling and Simulation Group under the direction of Dr. Alexander Alexeev. Matt received his M.S. in Mechanical Engineering from Georgia Tech in 2014, and continued there with his Ph.D. studies. During his graduate studies, he has worked as an instructor of Mechanical Engineering at Georgia Tech Lorraine in Metz, France, and also worked as a student intern with Sandia National Laboratories in Livermore, California. His research interests are in computational modeling and simulation, with an emphasis on fluid mechanics and fluid-solid interactions in applications including biological systems and the design of microfluidic devices.